DELFT UNIVERSITY OF TECHNOLOGY
Delft, April 7, 2023

Faculty of Applied Sciences and Aerospace Engineering

Master of Applied Physics and Master of Aerospace Engineering
Double Degree

Using ASPIRE and OpenFAST to simulate platform motions of a semi-submersible floating offshore wind turbine under uniform and sinusoidal inflow velocity and under different atmospheric stability

by

Violinde den Breeijen

Candidate
Violinde den Breeijen
ID 4698665

Supervisors
Prof. dr. H.J.J. Jonker (AP)
Dr. ir. A.C. Viré (AE)

External Supervisor
Prof. dr. ing. S. Kenjeres

Abstract

The energy consumption is growing and growing over the past few years and in the meanwhile, all nations are united by the Paris Agreement to undertake ambitious efforts to limit global warming. Therefore, there is a strong need for more renewable energy sources such as wind energy. To reduce the costs of adapting wind energy inputs to the power grid, it is necessary to make an accurate power forecast for wind farms. In this research the Umaine VolturnUS S semi-submersible floating platform designed for the IEA 15 MW reference turbine is studied to better understand the behavior of this floating construction. This is established by using a coupling between ASPIRE (turbulence resolving numerical weather model) and OpenFAST (wind turbine model).

After a convergence study, a uniform velocity profile was used as input showing the increased translations and rotations as wind speed increases. The natural frequency in each degree of freedom is determined from the oscillatory platform motions, greatly corresponding to the values from literature [1]. Adding a sinusoidal fluctuation to the velocity input profile in u or v (respectively surge or sway direction) clearly shows a coupling between the different degrees of freedom: increased responses at certain natural frequencies reveals an interaction between surge, pitch and heave (higher responses for fluctuations in u) and between roll, sway and yaw (higher responses for fluctuations in v), corresponding to the two sets of coupled equations in the equations of motion. The response function behaves as a low pass filter in all degrees of freedom: high response and zero phase difference for small frequencies and the opposite for large frequencies. In heave the phase difference behaves opposite because of its downwards direction.

To study the influence of atmospheric stability on the turbine's behavior, the surface heat flux was changed to create different atmospheric stability conditions. The wake recovery is fastest in the unstable regime (a wake length of $7D$) and slowest under stable conditions (a wake length of $23D$). This is due to the increase of turbulence intensity as stability decreases, which also explains why the temporal power fluctuations are largest under unstable conditions. The atmospheric stability does not influence the platform motions significantly.

When comparing a bottom-fixed wind turbine and a floating wind turbine, one obtains a similar velocity profile. The turbulent kinetic energy is slightly higher for the floating turbine: at $10D$ behind the rotor the maximum value was 1.2 times larger. The time-averaged power output was lower, but the temporal fluctuations were higher for the floating turbine compared to the fixed turbine, due to the increased turbulence intensity.

Because wind farms meet the expected supply threshold, the costs for energy producers can be reduced by using the coupling of ASPIRE and OpenFAST to create more accurate power forecasts for wind farms. It is recommended to validate the model by simulating a wind farm with real weather data and comparing the simulated with the real power output. Besides, one could find a method to describe the floating turbine using a moving actuator disk model. This would allow Whiffle to do very fast and very precise forecasting for semi-submersible offshore wind turbines.

Acknowledgement

I want to thank Whiffle for the graduation position they have offered me. Being a part of the team for the past nine months has been a pleasure, and you have made me feel very welcome. Even though it was sometimes challenging to combine the thesis with my cycling ambitions, the freedom within Whiffle really encouraged me to make a suitable planning. I want to express my gratitude to my supervisors, Axelle and Harm, for their enthusiasm and fast communication. I was greatly inspired by the scientific knowledge of Axelle and I admire Harm's pragmatic approach. Harm has taught me to trust my own results and my own approach, to discover new things rather than simply repeating what others have investigated.

In addition, Mikko deserves a heartfelt thank you. His patience and his thorough responses were a huge help to me during this project. And he was always available to fix technical problems, which was definitely necessary, particularly in the first few weeks. I always went to Pim with questions about wind turbines and atmospheric stability. I really appreciate his prompt and elaborate help when I unexpectedly dropped by his office.

During the final month of my project, Evert made the announcement that he would start a PhD using the coupling between ASPIRE and OpenFAST. I enjoyed our quick conversation about my own and about your research and I'm really looking forward to your project. In addition, I want to express my gratitude for your elaborate, time-consuming and detailed comments on my thesis, which significantly improved my report. Many thanks and best of success on your PhD!

Furthermore, I want to thank my parents for giving me the freedom to follow my own path during my time in Delft. They were always there for me and I loved working from their beautiful home in Holten, with the cat sitting behind me in the same chair, the dog lying on the ground and my parents working on the same table. I'm so appreciative of being welcomed. A special gratitude also goes out to Sija and Rob for our lovely cooking nights with delicious recipes and good chats. And a big thanks to Wander, for his mental support over the past few months. The scheduling of starting the race season, moving to Nijmegen and finishing my thesis all in one month was less than ideal. Many thanks for your great support!

I feel more than prepared to broaden my horizons and relocate to Nijmegen for an internship at TenneT after my time in Delft. I hope you will enjoy reading this thesis.

Violinde den Breeijen
Holten, April 2023

This thesis is a result of the research performed for the double degree master in Applied Physics and in Aerospace Engineering. In the table below, one can find the different parts of my research with the corresponding amount of ECTs. Besides, one can see which parts belong to which studies. In total, the thesis will add up to 52 ECTs, with an overlap of 32 ECTs and 10 ECTs for each study separately.

Topic	**Study**	**ECTs**
Coupling ASPIRE and OpenFAST for floaters	AE + AP	28
Convergence Study ASPIRE and OpenFAST	AE + AP	4
Linearize the Equations of Motion for a floater	AE	2
Platform Motions under Uniform Velocity Profiles	AE	4
Platform Motions under Different Atmospheric Conditions	AE	4
Bottom-Fixed and Floating Turbines under a uniform Velocity Profile	AP	3
Platform Motions under Different Gusts (Response Graph)	AP	7

Contents

Nomenclature

α	wind angle
$\delta(\Delta\phi)$	uncertainty in phase difference
$\delta(H)$	uncertainty in response function
$\Delta\phi$	phase difference
Δt	time step
Δt_{max}	maximum time step
$\Delta u/u_\infty$	velocity deficit
Δx	grid size in x-direction
Δy	grid size in y-direction
Δz	grid size in z-direction
ϵ	absolute percentage error
η	vector containing platform motions in all directions
η	viscosity
Γd	dry adiabatic lapse rate
Γenv	environmental lapse rate
Γm	moist adiabatic lapse rate
κ	von Kármán constant
ω	rotor speed
$\overline{w'\theta'_v}$	surface heat flux
ϕ	phase
ρ	density
σ	standard deviation
σ^2	variance
σ_i	normal force in i-direction
τ	total momentum flux
τ_{ij}	shear force if $i \neq j$ and normal force if $i = j$
θ'_v	perturbation in the potential temperature
θ_v	potential temperature
$\vec{v}$	velocity vector containing u, v and w

A	amplitude of the fitted sine
A	area
A_u	amplitude of the sinusoidal wind fluctuation in streamwise direction
A_v	amplitude of the sinusoidal wind fluctuation in spanwise direction
A_{ij}	added mass matrix
B_{ij}	damping matrix
C	Courant number
C	vertical offset of the fitted sine
c_P	power coefficient
C_{ij}	hydrostatic restoring coefficients
f	frequency
F_j	external forces
f_{max}	maximum turbine natural frequency
g	gravitational constant
H	response function
h	hub-height
k	turbulent kinetic energy
k_i	volume force in i-direction
L	Obukhoh length
M_{ij}	generalized mass matrix
n	number of moles
P	rotor power
p	pressure
R	ideal gas constant
T	temperature
t	time
t_0	horizontal offset of the fitted sine
T_u	amplitude of the sinusoidal wind fluctuation in streamwise direction
T_v	period of the sinusoidal wind fluctuation in spanwise direction
U	total internal energy

u	wind velocity in streamwise direction
u_*	friction velocity
u_i	input velocity in streamwise direction
u_∞	freestream velocity
u_{hub}	wind velocity in streamwise direction at hub height
U_{mag}	averaged velocity magnitude
V	volume
v	wind velocity in spanwise direction
v_i	input velocity in spanwise direction
w	wind velocity in vertical direction
w'	perturbation in the vertical velocity
x	streamwise direction
y	spanwise direction
z	height
z_0	surface roughness
Re	Reynolds number
RMSE	root mean square error

List of Figures

List of Tables

1. Introduction

The last few years, energy consumption has been significantly increasing, as shown in Figure 1 [2]. In the meantime, countries aim to limit global warming. All nations are united by the Paris Agreement to undertake ambitious efforts to combat climate change [13]. In comparison to 1990, Europe wants to lower its greenhouse gas emissions by 80% to 95% in 2050 [14]. This is only possible with a power generation focused on renewable energy. Therefore, there is a need for green energy sources to meet the rising demand.

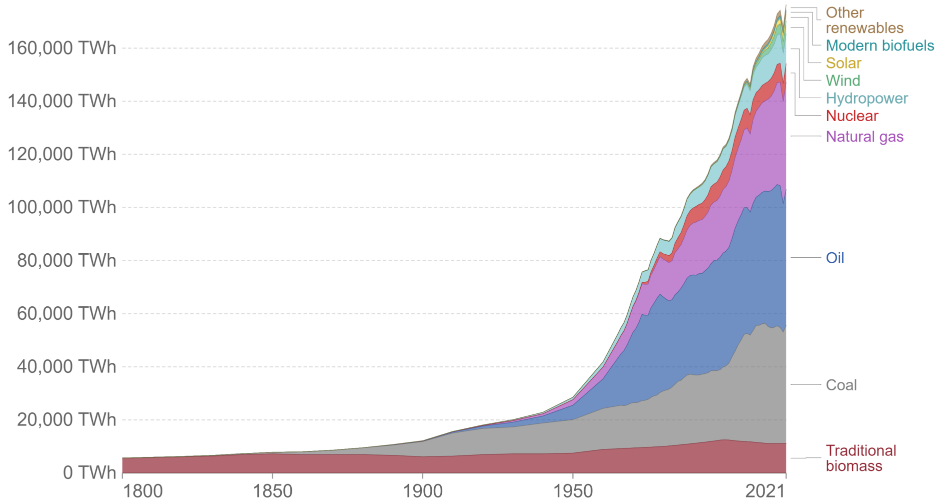

Figure 1: Global energy consumption by source from 1800 to 2021 [2].

In addition to solar power, wind energy will be one of the key sources of additional renewable energy. Wind energy can be generated both onshore and offshore. Compared to onshore turbines, offshore wind farms have higher costs, due to more complex electrical networks and foundations. In addition, the construction and operation are more challenging compared to onshore situations [15]. However, due to the fact that offshore winds often flow faster than onshore winds, the power generation can be higher [16]. Additionally, offshore wind speeds are more consistent than onshore ones, resulting in more reliable power generation [17]. Besides, a larger area is available offshore, and the turbulence levels are lower compared to onshore situations. In 2018, only a tiny fraction of global energy supply was provided by offshore wind [18]. Because turbines are growing in size and in power capacity, offshore wind energy is expected to expand impressively over the next two decades [18].

There exist different types of offshore wind turbines, for instance floating wind turbines and bottom-fixed wind turbines. When water depth increases above 50 m, floating wind turbines seem to be the most effective due to financial and technical constraints [19, 3].

In the current energy market, energy produces can be penalized with fines from governments for power outages. Besides, producers are not compensated for extra energy in case of exceeding the expected supply thresholds. In Germany, the annual costs of adapting wind energy inputs to the power grid are approximately 500 million euros [20]. Therefore, it is important to predict the power generation of a wind farm with high accuracy. Because this generation highly depends on the weather conditions, it is necessary to make a coupling between a weather forecasting model and a wind turbine simulation tool. In this research, such a coupling is established and the behavior of a floating wind turbine under different inflow conditions is evaluated. The remainder of this section provides some background information about these floating turbines, as well as a clear problem formulation and the structure of this report.

1.1. Floating Offshore Wind Turbines

A floating wind turbine is based on floating foundations, consisting of a floater, a turbine and a mooring system.

1.1.1. Floater

The floater is used as the TLP (Tension Leg Platform). This TLP is a floating foundation which is kept at rest using heavy steel rods, via suction anchors anchored on the seabed [21]. In general, there are three different types of floaters, as visualised in Figure 2 [22].

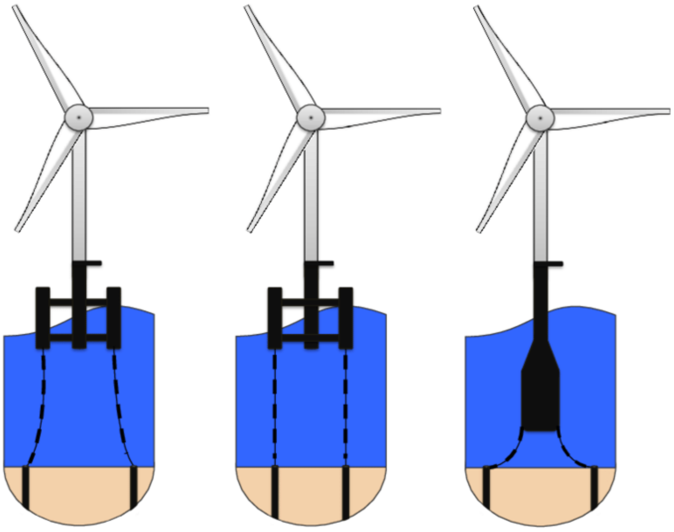

Figure 2: Three different types of floating foundations for offshore wind turbines: the semi-submersible system (left), the tension-leg floater (middle) and the floating spar buoy (right) [3].

- **Semi-Submersible Floaters** (left turbine): several cylinders form a base structure, providing stability due to its buoyancy. These floaters mainly experience large wave-induced motions, which cause the tower top to move significantly [22]. After assembly on a dry dock, the turbine is towed to its location. The floaters are independent of water depth. However, the costs of the mooring lines (attached to drag embedded anchors) significantly increases for higher water depths. The floater tries to minimize the surface area exposed to water, while maximizing the buoyancy by increasing the water mass displacement.
- **Tension-Leg Floaters** (centered turbine): the turbine stays at its position using a semi-submersible shallow structure, which is vertically tethered to the seabed using tensioned mooring lines. The structure is very stiff for rotational motions, and the turbine only experiences small wave-induced motions. Installation is a complex process, since the floater in itself is unstable. A special floatation is designed to stabilize the turbine during installation, after which the mooring lines are connected to maintain

stability. The tension-leg floaters work best for intermediate water depths (50 to 150 m). The mooring lines of such a system are short and therefore cheap (they extend vertically). However, one has to deal with high loads to provide constant tension between the anchors and the buoyancy tank.

- **Spar Buoy Floaters** (right turbine): by shifting the system's center below the buoyancy center, stability is achieved. A water depth of more than 100 m is required, with long mooring lines connected to drag embedded anchors. Although this system is stiff in translational motions, it is sensitive to rotational motions. The assembly can be performed both onshore and offshore.

1.1.2. Turbine

Also for the turbine there are several options: one can for example use airborne wind energy, in which greater altitudes (and correspondingly higher wind speeds) can be achieved with less materials. However, there are still challenges considering the system's design and control, and it is impossible to obtain constant power production. Another option is to use vertical-axis wind turbines, which are omnidirectional and have a lower center of gravity compared to regular wind turbines. However, they produce less power because of their unsteady loading and slower rotational speed. A last option considered here is a downwind 2-bladed turbine, which has a fairly simple design, a high rotational speed and low costs. However, this system is less effective than the other options considered here. [22]. There are many more options, and there is still a lot of research going on to optimize the offshore energy production using wind turbines. The most prevailing and best-known wind turbine (both onshore and offshore) is the three-bladed horizontal wind turbine, as shown in Figure 2.

1.1.3. Mooring System

The mooring system is used to maintain the wind turbine at the intended location in all water depths and to ensure stability. A mooring line is used to connect the anchor on the seabed to the floating structure. Several options are shown in Figure 2. A first option is to use catenary mooring (visualized in the most left turbine in Figure 2), in which a restoring force is presented because of the weight of the mooring lines. Although this system requires more material, one can use inexpensive anchors because the loads they encounter are only horizontal. Another option is to use taut mooring, as shown in the middle turbine in Figure 2, in which a restoring force exists due to line stiffness. Because the lines are straight, less material is needed. However, the loads on the anchors are now both in horizontal and in vertical direction, which requires costly anchors. A last option considered here (in the most right turbine in Figure 2) is to use tension legs, which derive their restoring forces from line stiffness. Once more, straight lines reduce the amount of material required. Although the loads on the anchor are only in vertical direction, expensive anchors are needed. [22]

1.2. Problem Formulation

In this research, the behavior of the UMaine VolturnUS S Reference Platform ([1]) is studied. This floating platform is developed for the IEA Wind 15-Megawatt Offshore Reference Wind Turbine ([4]) and belongs to the Semi-Submersible Floaters. The specified wind turbine is a three-bladed horizontal wind turbine and the floating platform has a catenary mooring system [1]. A visualisation of this combination is shown in Figure 3. A summary of the parameters for the wind turbine and floater are given in Table 1.

parameter	**specification**
rotor diameter	240 m
hub height	150 m
rated power	15 MW
number of blades	3
cut-in wind speed	3 m/s
rated wind speed	10.59 m/s
cut-out wind speed	25 m/s
design tip speed ratio	9.0
maximum rotor speed	7.56 rpm
platform type	floating
total mass	20,093 t
platform mass	17,839 t
tower mass	1,263 t
designed water depth	200 m
mooring system	three-line chain catenary

Table 1: Some general parameters for the IEA 15MW reference turbine ([4]) and the UMaine VolturnUS-S semi-submersible platform ([1]).

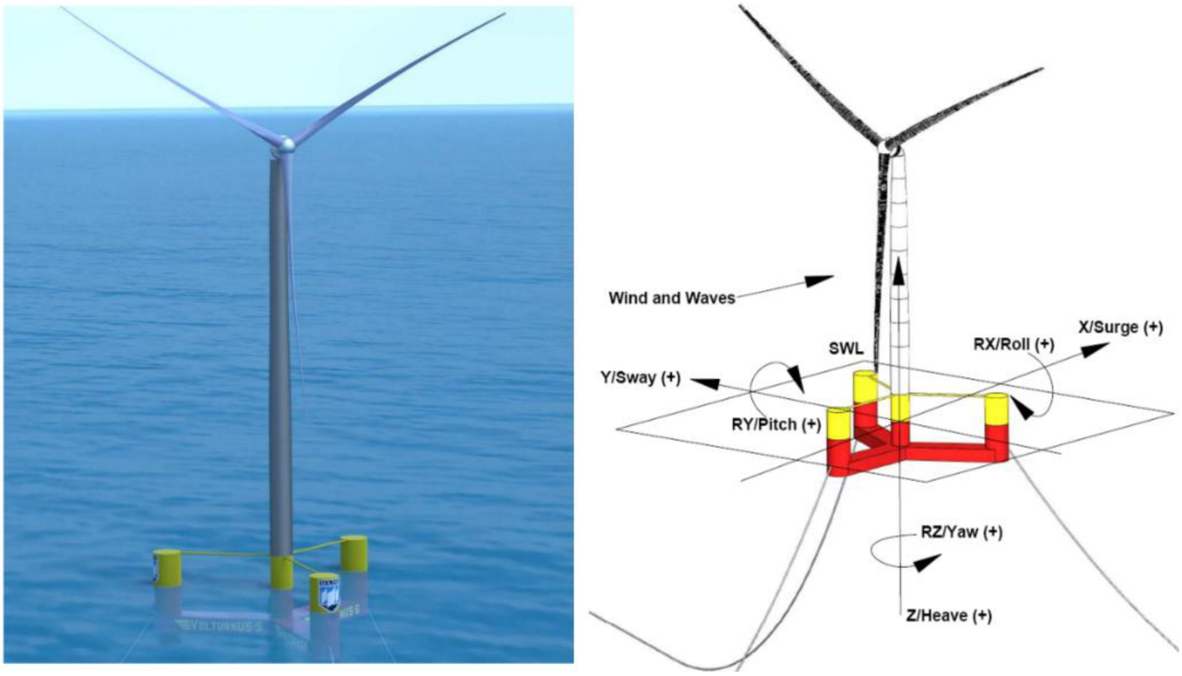

Figure 3: Visualisation of the UMaine VolturnUS S Reference Platform ([1]) with the IEA Wind 15-Megawatt Offshore Reference Wind Turbine ([4]) and a catenary mooring system [5].

This research consists of different research questions, all treated in separate chapters. To answer these questions, first some background information is needed and a coupling between the software ASPIRE and OpenFAST has to be established. Besides, a proper simulation set-up has to be found to simulate platform motions and flow fields under different conditions. In the research questions below, platform motions, power production and flow field are combined in the word *behavior*.

- What are proper settings to simulate the behavior of a semi-submersible floating wind turbine using a coupling between ASPIRE and OpenFAST? (Section 6)
- What are the influences of waves from the Pierson-Moskowitz spectrum on the behavior of the semi-submersible floating wind turbine compared to a still water situation? (Section 7)
- What are the influences of the magnitude of the uniform inflow wind velocity on platform motions and natural frequencies of the semi-submersible floater? (Section 8)
- How do different frequencies in a sinusoidal velocity input profile influence the platform motions for a semi-submersible floating turbine? (Section 9)
- What is the influence of atmospheric stability on the behavior of the semi-submersible floating wind turbine in terms of flow field, power production and platform motions? (Section 10)
- How does the behavior of a semi-submersible floating wind turbine differ from a bottom-fixed wind turbine in terms of velocity profile, power generation and turbulence intensity? (Section 11)

After this introduction, the report will continue with some background information about atmospheric stability. Then, a derivation of the equations of motion for floaters is presented in Section 3. Using computational fluid dynamics, with the help of the simulation tools ASPIRE and OpenFAST, the behavior of the platform and its motions can be simulated. Some background information about computational fluid dynamics and the used software programs are presented in Section 4 and Section 5 respectively. First, a coupling between the two software programs has to be established, after which different simulations can be performed. For these simulations, one has to choose a proper time step and grid size, which are obtained in a convergence study presented in Section 6. The influence of waves on the floaters behavior is then examined in Section 7. Using the obtained settings, one can study the platform motions under different conditions. First, a comparison is made between a uniform velocity inflow profile of 8 m/s and 15 m/s in Section 8. The obtained platform motions and velocity profiles are evaluated and the differences between the two cases are discussed in detail. After this, a sinusoidal wind fluctuation is added to the inflow profile of 8 m/s in either u- and in v-direction and the response in platform motions is studied for different gust-periods. A response graph is presented in Section 9 with an in-depth discussion about the obtained results. A study to the influence of atmospheric stability is elaborated upon in Section 10. Section 11 describes the difference in behavior between a semi-submersible floating wind turbine and a bottom-fixed one (a Monopile). This report will end with a conclusion and a discussion in respectively Section 12 and Section 13.

2. Atmospheric Stability

The formation of clouds, winds or thunderstorms are all results from certain atmospheric conditions. For example, the atmospheric stability has a great influence on the turbulence intensity and the wind speed. This stability can roughly be divided into 3 categories: stable, neutral and unstable. There is no analytical technique for calculating wind speeds at specific heights that can be applied for all stability situations according to Gualtieri et al. [23]. However, it is important to take this stability into account: for example, the power production of the NREL 5 MW wind turbine is up to 24% higher during the day (unstable conditions) than it is during the night (stable conditions) [24]. This section discusses how atmospheric stability affects the efficiency of wind power plants, starting with some background information about atmospheric stability, followed by some information about determining atmospheric stability. After this, the coupling between atmospheric stability and power plant efficiency for both onshore and offshore wind turbines will be discussed.

2.1. Atmospheric Stability

To determine the stability of a certain air parcel, one needs to know the temperature of the environment at different heights and the temperature of rising air. One way to find the temperature of a rising air parcel is by using a weather balloon [6]. This temperature depends on the height: it is known that pressure decreases with height, such that structures expend adiabatically with increasing height. This process takes energy and thus the temperature of the structure will decrease. Note that the structures temperature changes without exchanging heat with the environment: the change is only due to expanding or compressing of air. This decreasing temperature for increasing height is called the dry adiabatic lapse rate: $\Gamma_d = -9.8$ K/km. Under the assumption that air parcels move adiabatically in the atmosphere and that pressure decreases with height, the following definitions for stability in the atmosphere are formulated: [25]

- **Stable Atmosphere**: the temperature of the air parcel is cooler than the surrounding temperature, and thus the air parcel sinks and compresses. The parcel returns back to its original position after movement because buoyancy forces suppress disturbances in the flow, reducing turbulence.
- **Neutral Atmosphere**: the temperature of the air parcel is equal to the surrounding temperature, and thus the air parcel stays at the obtained position after movement, without any additional motions.
- **Unstable Atmosphere**: the temperature of the air parcel is warmer than the surrounding temperature, and thus the air parcel rises and expands. The parcel accelerates away from its original position after movement because buoyancy forces increase the disturbances in the flow.

2.1.1. Environmental Lapse Rate

For dry stability, one can easily check the stability of the atmosphere using the environmental lapse rate Γ_{env} compared with the dry adiabatic lapse rate Γ_d:

$$\begin{aligned} \Gamma_d &< \Gamma_{env} && \text{stable} \\ \Gamma_d &= \Gamma_{env} && \text{neutral} \\ \Gamma_d &> \Gamma_{env} && \text{unstable} \end{aligned} \tag{1}$$

However, when adding moisture, above guidelines are not valid anymore. According to the Clausius-Clapeyron relation, lower temperatures imply more saturation. If water starts to condensate, energy is released as latent heat ($2.5 \cdot 10^6$ J/kg for condensation [26]), significantly changing the lapse rate because the air parcel will cool at a smaller rate. The moist adiabatic lapse rate is given by $\Gamma_m = 4.5$ K/km. Using the moist stability, one defines additional regions:

$$\begin{aligned} \Gamma_m > \Gamma_{env} \qquad & \text{absolutely stable} \\ \Gamma_m < \Gamma_{env} < \Gamma_d \qquad & \text{conditionally unstable} \\ \Gamma_d < \Gamma_{env} \qquad & \text{absolutely unstable} \end{aligned} \tag{2}$$

Conditionally unstable implies that the buoyancy depends on the saturation of air [6]. A schematic overview of the atmospheric stability is shown in Figure 4.

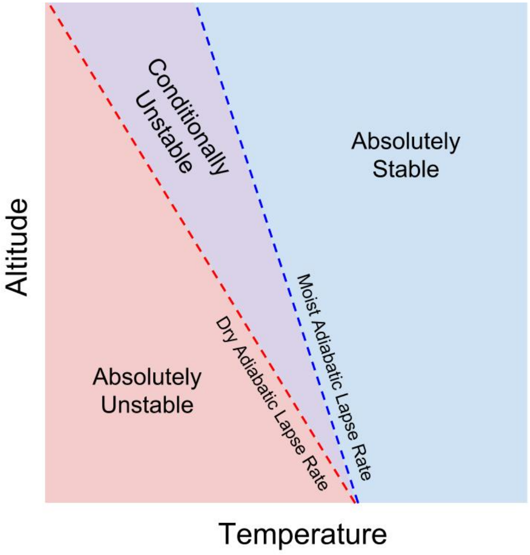

Figure 4: Stability of the atmosphere using the dry and moist adiabatic lapse rates ($\Gamma_d = 9.8$ *K/km and* $\Gamma_m = 4.5$ *K/km) [6].*

2.1.2. Monin-Obukhov Similarity Theory

Another way to define the atmospheric stability is by using the potential temperature θ_v, which represents the temperature the air parcel would have when moved to the ground (and thus excluding the temperature change caused by expansion due to pressure differences with height). The gradient of this potential temperature to the height ($\partial\theta_v/\partial z$) represents the stability: $\partial\theta_v/\partial z < 0$ corresponds to unstable conditions, $\partial\theta_v/\partial z = 0$ to neutral and $\partial\theta_v/\partial z > 0$ to stable conditions [25].

To describe the mean temperature and mean flow in the surface layer, one can use the Monin-Obukhov similarity theory, depending on the atmospheric stability. The obtained vertical distributions can then be used to generalize the logarithmic wind profile for non-neutral situations. In the Monin-Obukhov similarity theory, the dimensionless Obukhov length L is introduced, which characterizes the length scale of the turbulence in the surface layer. This length is determined by the following equation [27]:

$$L = -\frac{u_*^3}{\kappa \frac{g}{\theta_v} \overline{w'\theta_v'}} \tag{3}$$

in which u_* denotes the friction velocity (shear stresses written in units of velocity), κ the von Kármán constant ($\kappa = 0.40$), g the gravitational constant, θ_v the potential temperature, θ_v' the perturbation in this potential temperature and ω' the perturbation in the vertical velocity. This length scale can now be used as a criterion for atmospheric stability: if $L > 0$ the atmosphere is stable, if $L \to \infty$ it is neutral and if $L < 0$ it is unstable.

2.1.3. Characteristics

In general, during the day, unstable conditions occur onshore because the sun warms up the surface, which transfers its heat to the adjacent layer of air. During the night, the surface cools the air above it, leading to stable conditions. A similar but opposite reasoning can be used offshore, when warm air passes cooler ocean water [25]. When wind is coming from the sea, unstable and neutral conditions dominate in the North Sea [28].

Various characteristics for stable, neutral and unstable (convective) conditions are illustrated in Figure 5 ([7]), with h denoting the hub height for the IEA 5 MW Reference Turbine and z the height of measurement. As one can see, there is a low-level jet at $z/h \approx 1.8$ ($z = 162$ m) when the environment is stable and at $z/h \approx 2.6$ ($z = 234$ m) when the environment is neutral. There is no low-level jet in an unstable environment. From Figure 5b) and Figure 5c) it becomes clear that both the wind veer and the potential temperature are largest in the stable case and weakest in the convective case. Combining above observations shows that the stable boundary layer has the smallest momentum flux and the convective boundary layer the largest. Looking at Figure 5a) one can see that the mean velocity at hub height ($z/h = 1$) is strongest under stable and weakest under neutral conditions. Therefore, one would expect the highest power generation under stable conditions, middle power generation under unstable condition and lowest generation under neutral conditions for the IEA 5 MW Reference Turbine. Besides, because the turbulence intensity at hub height is smallest for the stable case and highest for the unstable case, the power fluctuation in unstable situations is expected to be more pronounced compared to stable situations. The NREL 5 MW reference turbine has a radius of 63 m and a hub height of 90 m, resulting in a maximum height for the blade tip of $z/h = 1.7$ [29]. At this point, there are significant differences in the characteristics shown in Figure 5 and therefore it is important to keep the atmospheric stability into account during power predictions or load calculations.

2.2. Determining Atmospheric Stability

There are various methods to determine the atmospheric stability. The bulk Richardson method was suggested as the most robust approach by Rodrigo et al. to assess atmospheric stability offshore [30]. The method is based on differential temperature measurements to determine potential temperature gradients. It is based on an empirical function formulated by Grachev and Fairall ([31]) and it seems to be a useful strategy for wind farm designers. Another choice for determining stability is to use the Obukhov length method. This method is based on sonic anemometer measurements and provides a local value of stability without any theoretical assumptions or empirical formulations. Therefore, the resulting information can be used to verify other methods, such as the bulk Richardson method [30].

Bardal et al. looked into various methods for determining atmospheric stability. They discovered that the measurement height can have a considerable impact on both accuracy and applicability when using the Richardson method. As a result, enough vertical spacing between measurements is required. According their research, the surface-layer Richardson formulation

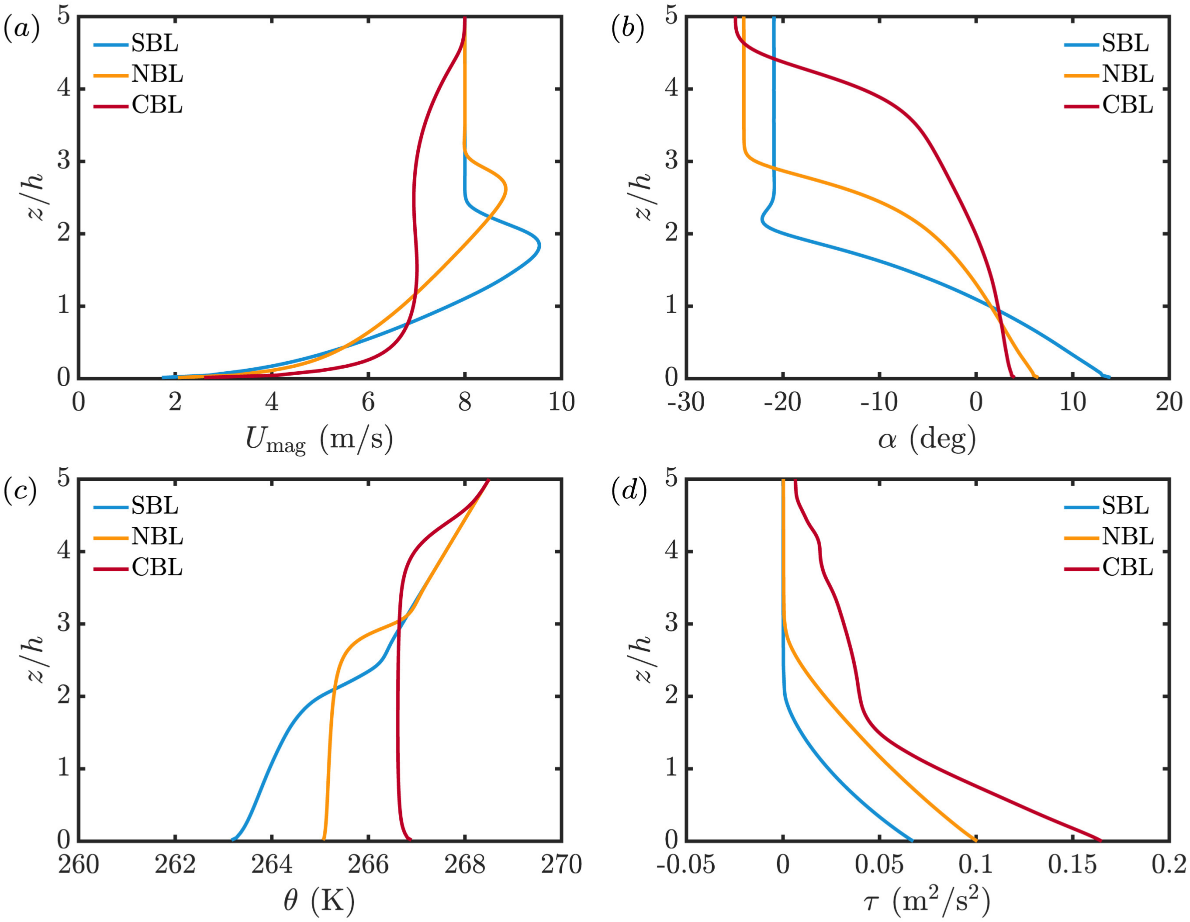

Figure 5: Vertical profiles for the stable (SBL), neutral (NBL) and convective (CBL) boundary layer of a) the averaged velocity magnitude $u_{mag} = \sqrt{u^2+v^2+w^2}$ *with* u*,* v *and* w *being the mean velocities in respectively streamwise, spanwise and vertical direction, b) the wind angle* $\alpha = \tan^{-1}(w/u)$*, c) the potential temperature* θ_v*, and d) the total momentum flux* τ *[7].*

is more robust compared to the bulk Richardson formulation, because it shows less variation with measurement height. Empirical relations can be used to relate the Richardson number to atmospheric stability. Although the obtained results do not perfectly overlap with measurements from sonic anemometers, the distributions are qualitatively similar. Therefore, it is advantageous to employ the surface-layer Richardson approach for long-term measurements, rather than the more complex sonic method with high-accuracy equipment [32].

This influence of measurement height on the expected atmospheric stability is also found by other research [32, 33]: the measurements indicate less neutral circumstances nearer to the surface than at high altitudes. Therefore, sonic fluxes measured at 50 m are not representative for the surface layer. Near coasts, more stable correction is needed compared to locations in the middle of the sea [33].

According to measurements made by offshore masts in the German Bight, the atmospheric stability varies with wind direction: stable conditions were anticipated for southerly winds arriving from the land, whereas unstable conditions predominate for winds coming from the north (the open sea) [34]. In general, warm winds imply stable conditions and cold winds bring unstable conditions.

2.3. Atmospheric Stability and Power Plant Efficiency

The atmospheric stability can significantly impact the power production, the fatigue and the control of wind turbines. For instance, Churchfield et al. used numerical experiments to study the impact of atmospheric stability and surface roughness on wind turbine dynamics. Atmospheric winds and wind turbine flows were obtained using large-eddy simulations (LES). Several quantities around different locations of a 5 MW wind turbine were evaluated using both a low and a high surface roughness (representing respectively offshore and onshore settings), for neutral and unstable conditions. By locating a second turbine 7 rotor diameters downwind, wake effects were investigated for all scenarios.

Churchfield et al. claim that as surface roughness increases from $z_0 = 0.0001$ m (offshore conditions) to $z_0 = 0.2$ m (onshore conditions) there is a corresponding increase in turbulence intensity, resulting in enhanced mixing and faster wake recovery. This permits the downwind turbine to produce 10% more power [8]. As a result of the weather, the surface roughness offshore can change: calm sea for instance in itself already changes between $z_0 = 1 \cdot 10^{-4}$ m and $z_0 = 3 \cdot 10^{-4}$ m [35]. However, compared to the values of $z_0 = 0.001$ m (offshore) and $z_0 = 0.2$ m (onshore) as utilized in Churchfield's research, this discrepancy is significantly smaller. Therefore, further research is required to determine how the dynamics of turbines are affected by shifting surface roughness offshore as a result of varying weather conditions.

According to the research of Churchfield et al., a downwind turbine's power output increases by 15% when the atmospheric stability is reduced from neutral to unstable, using an identical surface roughness [8]. It should be noted that just 2 wind turbines were used for this study. It would be interesting to observe what happens in a larger power plant when the atmospheric stability changes.

Churchfield et al. also studied wake deficits. The obtained results are shown in Figure 6, in which ΔU is defined as $\Delta U = \left(\overline{U} - \langle U \rangle_{hub}\right) / \langle U \rangle_{hub}$, with $\overline{U}$ being the time-averaged magnitude of the flow (in streamwise direction) and $\langle U \rangle_{hub}$ the horizontally averaged wind speed at hub height (being 8 m/s). As a result, $\Delta U = 0$ denotes complete recovery to $\langle U \rangle_{hub}$ and $\Delta U = 1$ implies no flow speed. The upper graphs show horizontal profiles at hub height and the bottom graphs show the vertical profiles at hub height, with the plotted profiles 1 rotor diameter apart from each other. The two wind turbines are shown as thick black lines. In this figure, one can see four different scenarios, using high (H) and low (L) surface roughnesses, as well as neutral (N) and unstable (U) atmospheric conditions. Once more it is demonstrated that the greater mixing causes the wake to recover more quickly for high surface roughness. Additionally, increased stability leads to slower wake recovery. The asymmetry in the vertical wake profiles is mainly due to wind shear and the fact that the wake rotates in opposite direction compared to the blade rotation. As a result, the low speed flow beneath the turbine is rotated to the left, while the high speed flow above the turbine is slightly rotated to the right. Because there is very little wind shear in vertical direction in this study, the Coriolis force's impact on asymmetry is assumed to be insignificant [8].

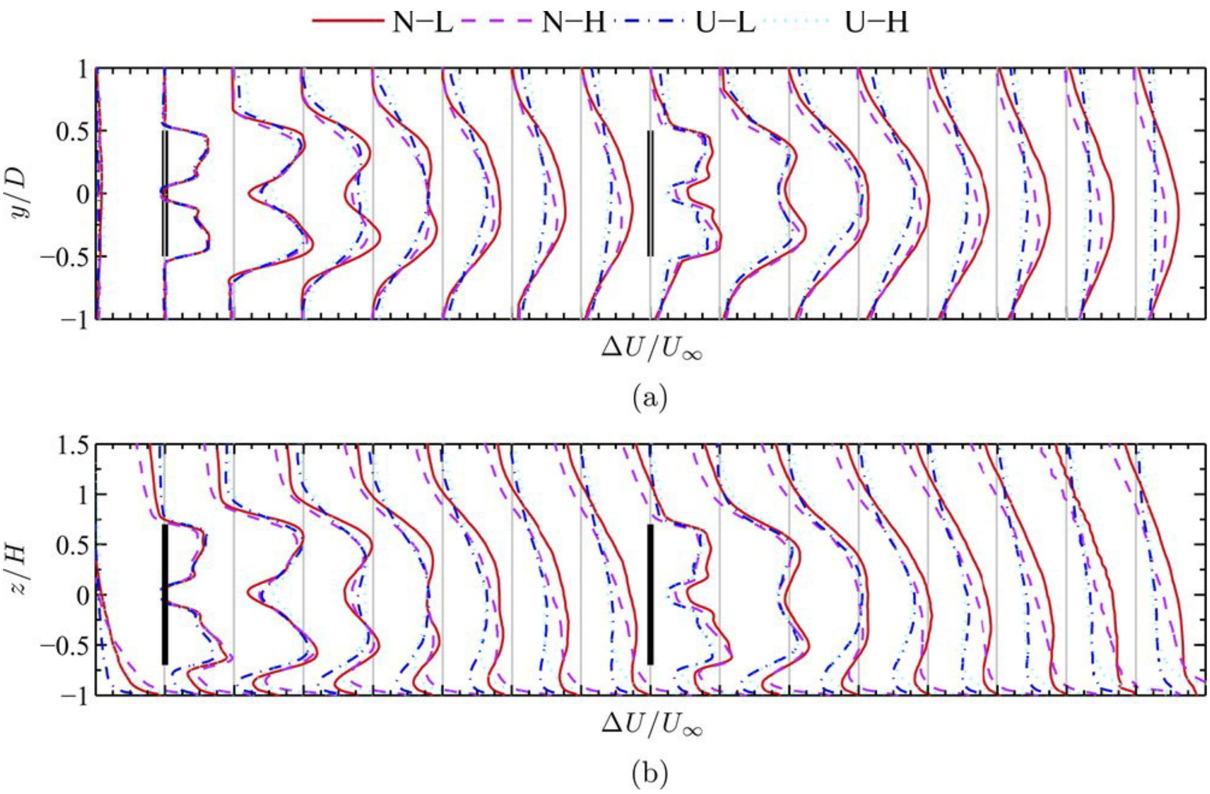

(a)

(b)

Figure 6: The a) horizontal and b) vertical wind profiles normalized by the horizontally averaged wind speed at hub height (being 8 m/s) plotted 1 rotor diameter apart for different atmospheric conditions: neutral (N) or unstable (U) atmosphere, combined with low (L) and high (H) surface roughness. The horizontal axis varies from 0 to 0.5 for each profile [8].

Also Subramanian et al. showed the importance of taking into account the atmospheric stability during simulations of a wind turbine: in unstable conditions, the wake evolution was inclined with 9° angle rather than following the main wind direction [36]. Under stable conditions, there is a larger mean power deficit compared to neutral or unstable conditions [37, 38]. The wind speed reduction at hub height rises as stability increases [39].

Emeis discovered that the wind speed reduction at hub height is larger over smooth surfaces offshore than over rough surfaces onshore. To prevent shadowing effects of the upstream farm, a greater distance between the wind turbines is needed in offshore scenarios compared to onshore situations: under neutral conditions, the offshore wind parks' wake is approximately three times longer compared their onshore counterparts [39].

Abkar et al. investigated the influence of atmospheric stability on the wakes of a wind turbine. Using an LES-model with an actuator-disk model including rotation ([40]), their obtained growth rate under unstable conditions was 2.4 times larger than under stable conditions. Besides, it was found that the maximum turbulent kinetic energy production is further downwind under stable conditions compared to unstable or neutral conditions [41].

More research on the influence of atmospheric stability on the performance of a wind turbine is performed for both onshore and offshore wind turbines.

2.3.1. Onshore Wind Turbines

The impact of atmospheric stability on onshore wind turbines is studied quite elaborate. Already in 1981, Hiester and Pennell showed that unstable situations are best in regard of power generation in wind farms due to their faster wake recovery and thus higher wind speeds at the downwind rotor. However, because it has the least wind shear, the neutral atmosphere performs best in terms of the rotor's fatigue life. Stable conditions combine the decreased wind speed with the increased wind shear, and therefore is unfavorable for a wind turbine in a wind farm [42].

Above statement was supported by Kim et al., who investigated how the South-Korean wind farm Dongbok-Bukchon was affected by air stability [43]. They discovered that for the wind farm the largest annual energy production and the lowest power deviation were obtained in unstable conditions: the unstable production was 5-7% higher than under neutral conditions. The opposite was true for stable conditions, where the lowest power generation and the biggest power deviation were recorded.

Later, Liu et al. investigated the effects of atmospheric stability on the performance of a wind turbine located behind a hill [7]. They discovered that in unstable situations, a hill wake reduces power production by 34.8%, because the wind veer is insufficient to deflect the hill wake. However, there is a 70% increase in power production oscillations. Under neutral conditions, the wind veer is sufficient to deflect the hill wake and therefore the power production is not affected, although there is an increase of 60% in power fluctuations compared to the no-hill case. It is remarkable that the hill, under stable conditions with growing power fluctuations, can boost the downstream turbine's power output by up to 24%. This increase is due to the low-level jet as shown in Figure 5a).

2.3.2. Offshore Wind Turbines

Although offshore wind farms mostly suffer unstable conditions, the majority of research is conducted under the assumption of neutral stability conditions. Therefore there is not much known about the influence of atmospheric stability on the performance of an offshore wind turbine. In the analysis, it is important to distinguish between bottom-fixed wind turbines and floating ones due to their difference in dynamics.

Bottom-Fixed Wind Turbines According to Wharton and Lundquist, unstable conditions can reduce the power output from an unwaked (isolated) turbine by 20% in comparison to stable conditions for the same hub-height wind speed [44]. However, when considering a wind farm instead of an isolated turbine, it was discovered that under stable conditions (40% of the time, with its lower ambient turbulence intensity), there was a slower mixing of low momentum wakes with the surrounding compared to neutral conditions (20% of the time) or unstable conditions (40% of the time). Therefore, the Nysted offshore wind plant performs most inefficiently in stable conditions [45]. According to Jensen, the Horns Rev offshore wind plant operates most effectively when atmospheric stability is reduced [46]. In conclusion, wind farms perform less in stable conditions compared to unstable conditions, whereas it is the other way around for isolated wind turbines. According to wind tunnel experiments, under stable conditions, the frequency of wake meandering was up to 18% lower than under neutral or unstable conditions. However, under neutral conditions wakes decay most quickly [47]. This wake meandering effect was also investigated by Abkar et al.: they discovered that wake meandering is stronger under unstable situations compared to neutral and stable conditions (which is due to the fact that the wake's growth rate was roughly 2.4 times greater for the unstable situation compared to neutral and stable conditions) [41].

Research performed on the German offshore wind farm Alpha Ventus showed a pronounced difference between stable and unstable conditions in terms of power output: up to 15% increase in a non-wake situation and even up to 20% increase for turbines in the wake of other turbines in the unstable situation compared to the stable conditions [48] .

Floating Wind Turbines It was found by Rivera-Arreba et al. that both the atmospheric stability and the turbulence model significantly influence the response of a floating wind turbine in the low-frequency range, with the largest structural response under unstable conditions [49]. By fitting the input parameters of the Kaimal model and the Mann model to LES data and to point observations, the effect of atmospheric stability was taken into account in the simulations.

Wise et al. examined the impacts of floating wind turbines' wake meandering [50]. According to their research, a uniform wake deficit (with negligible meandering) was obtained when using the Kaimal model as described in the IEC 61400-1 standard (spatial coherence captured in longitudinal velocity component only). However, when utilizing the Mann model or the extended Kaimal model (spatial coherence captured in both longitudinal, lateral and vertical velocity components) increasing wind speed led to a decrease in wake meandering at higher frequencies. Besides, the more turbulence, the more meandering. For wind speeds below rated, this lateral meandering increased yaw motions up to 40% for the semi-submersible floater and up to 20% for the spar buoy floaters and the tension-leg floaters. The lower the turbulence intensity, the bigger the standard deviations in yaw motions for a downstream turbine. For all floating concepts, fatigue was increased for both above-rated wind speeds due to the velocity deficit and below rated wind speeds due to wake meandering. This effect however is significantly more pronounced when using the Kaimal model compared to the Mann-model.

3. Equations of Motion

As explained in the introduction, an offshore floating wind turbine exists of a floater, a turbine and a mooring system. The floaters experience different types of motions. In Figure 7 one can find the definitions of the six degrees of freedom: 3 rotational ones (roll, pitch and yaw) and 3 translational ones (surge, sway and heave) [51].

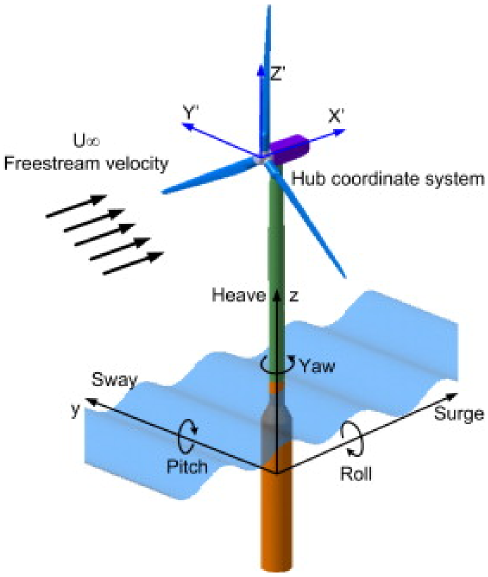

Figure 7: The six degrees of freedom for a floating wind turbine with respect to the main wind direction, being three translations (surge, sway and heave) and three rotations (roll, pitch and yaw) [9].

In this section, the motions in all degrees of freedom, their influences on the turbines performance and the mathematical expressions are discussed in detail, starting with the equations of motion.

3.1. General Expression for the Equations of Motion

The governing equation for all these motions is given by the following matrix equation:

$$\sum_{k=1}^{6} \left[\left(M_{jk} + A_{jk} \right) \ddot{\eta}_k + B_{jk} \dot{\eta}_k + C_{jk} \eta_k \right] = F_j, \qquad j = 1, 2, ..., 6 \tag{4}$$

in which M_{jk} represent the components of the generalized mass matrix, A_{jk} the added mass coefficients, B_{jk} the damping coefficients, C_{jk} the hydrostatic restoring coefficients and F_j the external forces. Above summation contains all six degrees of freedom for both the symmetric (translational degrees of freedom) and anti-symmetric motions (rotational degrees of freedom): the subscript i denotes the direction in surge, sway, heave, roll, pitch and yaw from $i = 1$ to $i = 6$ respectively. The expressions for η, $\dot{\eta}$ and $\ddot{\eta}$ are given by respectively the position, the velocity and the acceleration in the i-th degree of freedom. Note that the matrices depend on the system characteristics such as the structure geometry, the wave frequency, the wave amplitude, the water depth, etc. [52]

In Equation 4 of motion it is assumed that the floating body is slender and rigid with symmetric mass distribution, that the amplitude of motion is small such that the equations can be linearized, that the effect of viscosity can be neglected except in roll motion, that the incident waves are of single periodicity and unidirectional and that longitudinal and transverse motions are decoupled due to lateral symmetry [52].

The generalized mass matrix is given by the following:

$$M_{jk} = \begin{bmatrix} M & 0 & 0 & 0 & Mz_c & 0 \\ 0 & M & 0 & -Mz_c & 0 & 0 \\ 0 & 0 & M & 0 & 0 & 0 \\ 0 & -Mz_c & 0 & I_4 & 0 & -I_{46} \\ Mz_c & 0 & 0 & 0 & I_5 & 0 \\ 0 & 0 & 0 & -I_{46} & 0 & I_6 \end{bmatrix} \tag{5}$$

in which M represents the mass of the floating body, I_j the moment of inertia in the jth mode of motion and I_{jk} the product of inertia for the kth mode of motion coupled with the jth mode. Because the floater has a fore-aft symmetry, I_{46} (the coupling between roll and yaw) vanishes [53]. The center of gravity G is given at $(O', 0, z_c)$. The matrices for the UMaine VolturnUS S semi-submersible platform are given by the following [1]:

$$\begin{aligned}
M &= \begin{bmatrix} 2.0093 \cdot 10^{7} & 0 & 0 & 0 & -3.002 \cdot 10^{8} & 0 \\ 0 & 2.0093 \cdot 10^{7} & 0 & 3.002 \cdot 10^{8} & 0 & 0 \\ 0 & 0 & 2.0093 \cdot 10^{7} & 0 & 0 & 0 \\ 0 & 3.002 \cdot 10^{8} & 0 & 1.251 \cdot 10^{10} & 0 & 0 \\ -3.002 \cdot 10^{8} & 0 & 0 & 0 & 1.251 \cdot 10^{10} & 0 \\ 0 & 0 & 0 & 0 & 0 & 2.367 \cdot 10^{10} \end{bmatrix} \\
A &= \begin{bmatrix} 9.640 \cdot 10^{6} & 0 & 0 & 0 & -1.010 \cdot 10^{8} & 0 \\ 0 & 9.640 \cdot 10^{6} & 0 & 1.010 \cdot 10^{8} & 0 & 0 \\ 0 & 0 & 2.480 \cdot 10^{7} & 0 & 0 & 0 \\ 0 & 0 & 0 & 1.160 \cdot 10^{10} & 0 & 0 \\ -1.010 \cdot 10^{8} & 0 & 0 & 0 & 1.160 \cdot 10^{10} & 0 \\ 0 & 0 & 0 & 0 & 0 & 2.010 \cdot 10^{10} \end{bmatrix} \\
B &= \begin{bmatrix} 9.225 \cdot 10^{5} & 0 & 0 & 0 & -8.918 \cdot 10^{6} & 0 \\ 0 & 9.225 \cdot 10^{5} & 0 & 8.918 \cdot 10^{6} & 0 & 0 \\ 0 & 0 & 2.296 \cdot 10^{6} & 0 & 0 & 0 \\ 0 & 8.918 \cdot 10^{6} & 0 & 1.676 \cdot 10^{10} & 0 & 0 \\ -8.918 \cdot 10^{6} & 0 & 0 & 0 & 1.676 \cdot 10^{10} & 0 \\ 0 & 0 & 0 & 0 & 0 & 4.798 \cdot 10^{10} \end{bmatrix} \\
C &= \begin{bmatrix} 0 & 0 & 0 & 0 & 0 & 0 \\ 0 & 0 & 0 & 0 & 0 & 0 \\ 0 & 0 & 4.470 \cdot 10^{6} & 0 & 0 & 0 \\ 0 & 0 & 0 & 2.190 \cdot 10^{6} & 0 & 0 \\ 0 & 0 & 0 & 0 & 2.190 \cdot 10^{6} & 0 \\ 0 & 0 & 0 & 0 & 0 & 0 \end{bmatrix}
\end{aligned} \tag{6}$$

For low frequencies, motions of offshore wind turbines are dominated by spring terms. For high frequencies, motions are mainly determined by mass terms. In between these frequencies, motions are dominated by damping terms and the heave amplitude is largest. [22]

3.2. The Coupled Equations of Motion

Substitution of the matrices in Equation 6 into Equation 4, yields the following equations:

$$\begin{aligned}
(M_{11}+A_{11})\ddot{\eta}_1+(M_{15}+A_{15})\ddot{\eta}_5+B_{11}\dot{\eta}_1+B_{15}\dot{\eta}_5&=F_1\\
(M_{22}+A_{22})\ddot{\eta}_2+(M_{24}+A_{24})\ddot{\eta}_4+B_{22}\dot{\eta}_2+B_{24}\dot{\eta}_4&=F_2\\
(M_{33}+A_{33})\ddot{\eta}_3+B_{33}\dot{\eta}_3+C_{33}\eta_3&=F_3\\
M_{42}\ddot{\eta}_2+(M_{44}+A_{44})\ddot{\eta}_4+B_{42}\dot{\eta}_4+B_{44}\dot{\eta}_4+C_{44}\eta_4&=F_4\\
(M_{51}+A_{51})\ddot{\eta}_1+(M_{55}+A_{55})\ddot{\eta}_5+B_{51}\dot{\eta}_1+B_{55}\dot{\eta}_5+C_{55}\eta_5&=F_5\\
(M_{66}+A_{66})\ddot{\eta}_6+B_{66}\dot{\eta}_6&=F_6
\end{aligned} \tag{7}$$

The value for A_{ij} is given at matrix position $A[i,j]$, and similarly for B_{ij}, C_{ij} and M_{ij}. The values for the wave exciting forces and moments F_i can be determined using the following equation:

$$F_i=\bar{F}_i\sin(\bar{\omega}t+\epsilon),\ \ i=1,2,3,4,5,6 \tag{8}$$

in which ϵ represents the phase angle and $\bar{\omega}$ the encountering frequency [52]. The values for $\bar{F}_i$ can be found using the following expressions [53]:

$$\begin{aligned}
\bar{F}_1&=\alpha\rho\int(f_1+h_1)d\xi\\
\bar{F}_2&=\alpha\rho\int(f_2+h_2)d\xi\\
\bar{F}_3&=\alpha\rho\int(f_3+h_3)d\xi\\
\bar{F}_4&=\alpha\rho\int(f_4+h_4)d\xi\\
\bar{F}_5&=-\alpha\rho\int\xi(f_3+h_3)d\xi\\
\bar{F}_6&=\alpha\rho\int\xi(f_2+h_2)d\xi
\end{aligned} \tag{9}$$

in which α represents the amplitude of the incident wave, h_i the sectional diffraction force, f_i the sectional Froude-Kriloff force and ξ the variable of integration, which is taken over the whole length of the floater. An in-depth derivation of the expressions for h_i and f_i is out of scope of this research and can be found in [53]. Most important for this research is that for still water the amplitude of the incident wave α equals zero (there are no waves). Therefore $\bar{F}_i=0$ and thus $F_i=0$ (see Equation 8), meaning that the right hand sides in Equation 7 vanish.

For a body with lateral symmetry in both weight and shape, it appears that the equations of motion can be decoupled into two systems of equations: one set describing the motions in sway, roll and yaw and one set describing the motions in surge, heave and pitch. In other words, for a body with lateral symmetry placed in the water, motions in surge, heave and pitch direction are not coupled with motions in sway, roll and yaw [53].

3.2.1. Sway, Roll and Yaw Motions

The equations to describe the motions in sway, roll and yaw direction are given by the following:

$$\begin{aligned}
(A_{22}+M_{22})\ddot{\eta}_2 + B_{22}\dot{\eta}_2 + (A_{24}+M_{24})\ddot{\eta}_4 + B_{24}\dot{\eta}_4 &= 0 \\
M_{42}\ddot{\eta}_2 + B_{42}\dot{\eta}_2 + (A_{44}+M_{44})\ddot{\eta}_4 + B_{44}\dot{\eta}_4 + C_{44}\eta_4 &= 0 \\
(A_{66}+M_{66})\ddot{\eta}_6 + B_{66}\dot{\eta}_6 &= 0
\end{aligned} \tag{10}$$

Note that the motions in sway and roll are coupled, while the motions in yaw direction are not directly related to the motions in the other directions.

3.2.2. Surge, Heave and Pitch Motions

The equations to describe the motions in surge, heave and pitch direction are given by the following:

$$\begin{aligned}
&(A_{11}+M_{11})\ddot{\eta}_1 + B_{11}\dot{\eta}_1 + (A_{15}+M_{15})\ddot{\eta}_5 + B_{15}\dot{\eta}_5 = 0 \\
&(M_{33}+A_{33})\ddot{\eta}_3 + B_{33}\dot{\eta}_3 + C_{33}\eta_3 = 0 \\
&(A_{51}+M_{51})\ddot{\eta}_1 + B_{51}\dot{\eta}_1 + (A_{55}+M_{55})\ddot{\eta}_5 + B_{55}\dot{\eta}_5 + C_{55}\eta_5 = 0
\end{aligned} \tag{11}$$

Again note the coupling between motions in surge and heave, while the motions in pitch are not directly coupled to the motions in the other directions.

For most offshore platforms, the largest amplitude in motions are in surge and pitch direction. Research shows that the average power production increases slightly for increasing motion frequency or motion amplitude. The influence of pitch motion on the performance of the wind turbine is larger than the influence of surge motion. [22, 10]

3.3. Static Instability

In Figure 8 one can see the effect of motions on the flow field passing the wind turbine [10]. This also visualises one of the main challenges for floating offshore wind turbines, being the static instability. When for example the wind speed increases, the turbine moves backwards (the most right turbine in Figure 8). To optimize the power output, the controller increases the pitch to reduce the power coefficient. However, this leads to a reduced thrust, and thus the turbine moves forward (such as the second turbine from the left in Figure 8) and the turbine experiences again an increase in induced wind speed. Now the whole loop starts over again, called the static instability. This instability can be solved by for example reducing the controller bandwidth.

3.4. Natural Frequencies

To see which components are related to damping and which are related to added mass, one can perform a free-decay test [22]. In this test, the linear and quadratic damping, as well as the natural frequency in each degree of freedom are determined by releasing the structure after a certain offset. The added mass is related to the force in phase with the motion. The damping is related to the force out-of-phase with the motion.

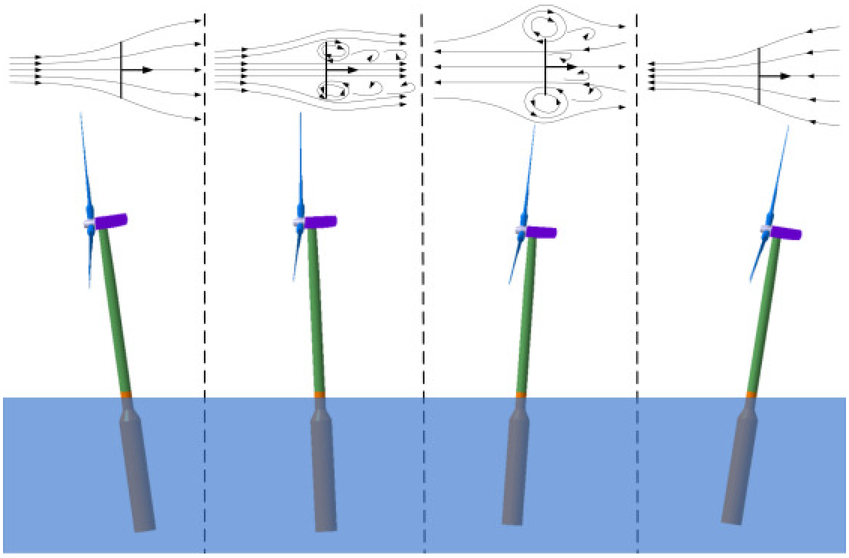

Figure 8: The effect of the platform pitching motion on the surrounding flow field [10].

For the chosen UMaine VolturnUS S Reference Platform, Allen et al. performed free-decay simulations for each of the platform degree of freedom to find the natural frequencies. In these tests, a still wind environment was assumed. The blades were oriented such that minimal drag was produced, to minimize aerodynamic drag influences. The obtained results are presented in Table 2. [1]

Degree of Freedom	**Natural Frequency**
Surge	0.007
Sway	0.007
Heave	0.049
Roll	0.036
Pitch	0.036
Yaw	0.011

Table 2: The natural frequencies in Hz for movements in the six degrees of freedom for the floating platform, obtained with free-decay simulations. [1]

Linear-excited motions occur in the wave-frequency range, and high-frequency motions occur due to resonance oscillations in roll, pitch and heave, with lower periods compared to most waves. Besides, there are slow-drift and mean-drift motions, which are generally caused by irregular waves and wind. These motions have higher periods compared to waves with small velocities and small accelerations, resulting from resonance oscillations in surge, sway and yaw [22].

4. Modelling

The design of an offshore wind turbine exists of several modelling steps, from low costs and low accuracy to high costs and high accuracy. One starts with reduced modelling in the pre-design. If this model satisfies the demands, the aero-servo-hydro-elastic coupling is tested on the design in the design validation stage. When this coupling is studied and validated, it is time for the detailed design in which computational fluid dynamics and finite elements methods are used. [22]

Also the wind turbine is modelled in different steps, with increasing complexity (from low-fidelity to high-fidelity). The choice of this model depends on many aspects, for example whether the flow is viscous or inviscid. There exist empirical and exact models, with varying videlity. The simplest model works with an actuator disk, which assumes a 1D steady, inviscid, irrotational and incompressible flow with constant internal energy. The rotor is assumed to be a porous disk and the averaged rotor loading can be obtained. Using mass conservation, one can determine the flow properties. This model is only valid for induction factors below 0.4 [54]. More involved is the Blade Element Momentum theory (BEM), in which blades are divided into different elements with each their own loading. BEM assumes independency of these annuli, and does not account for wake expansion, tip losses or yaw [55]. In the actuator disk model, the pressure, velocity and loading are assumed to be uniform over each section of the streamtube. In BEM, this is not the case and the streamtube is divided into different annuli, independent of each other [56]. To include even more physics in the model, one can use the 2D lifting line model, which is based on vortex filaments: lines of constant circulation on which the vorticity is concentrated. This model allows to calculate the loads at any point in space [56]. According to this equation, only a change in a force field is able to produce vorticity. This vortex travels with the corresponding local velocity to an infinite distance. It is assumed that the wake is axisymmetric in case of steady turbines. When the turbine is pitched or yawed, a 2D model is not sufficient and a 3D model is needed including 3D wake dynamics. The shed vortex is deformed due to self-induction. [22]

The mooring lines are commonly modeled as linear springs in a quasi-static model: $F = -k\Delta x$, in which F represents the force, k the spring constant and Δx distance that the spring is compressed or extended compared to its length without force applied. This spring model does not take into account the environmental interactions and therefore underestimates the load peaks. A more realistic model uses a kinematic chain of components to represent the mooring lines. [22]

The behavior of the floating wind turbine is determined using Computational Fluid Dynamics (CFD). In this section, some background about CFD will be given, such as the conservation laws on which CFD is based (the Navier-Stokes equations), an introduction to Large Eddy Simulations and some simulation conditions.

4.1. Governing Equations

By solving conservation laws, fluid motions can be predicted. To describe all properties of a fluid flow, one needs the pressure p, the density ρ, the temperature T and the velocity $\vec{v} = (u, v, w)^T$. To find these six variables, six equations are required to solve the system. Five of these equations come from the conservation laws. For a single-phase, compressible flow these consist of the conservation of mass (1 equation), the conservation of momentum (1 equation in each direction) and the conservation of energy (equation of state, 1 equation). All conservation laws together are captured in the Navier-Stokes equations. The equation of state links the temperature, pressure, density and velocity to the total internal energy U. The sixth equation needed to solve the system is the ideal gas law. [57] Note that in case of constant density, there are only 5 variables and the ideal gas law is not needed to solve the system.

4.1.1. Assumptions

In general, fluid mechanics are described by very complex partial differential equations. It appears that in some cases, one can neglect certain terms while the solution is not changed significantly [57]. Therefore, before discussing the governing equations in detail, some of these assumptions are evaluated in this paragraph.

Fully Developed Flow In a fully developed flow, the flow profile does not change when moving along a certain axis. For example, think of a very long horizontal pipe with constant diameter, with an inflow from a very large reservoir. One can easily understand that the flow field just after the inlet is not fully developed yet: since the flow has to go from a larger reservoir to a smaller diameter, the flow will change. However, as the fluid moves along the pipe, it will find a certain form that is not changing anymore. This is called the fully developed state. In this example of a pipe in x-direction, a fully developed scenario is obtained when all partial derivatives with respect to x equal zero. [57]

Incompressible Flow Incompressibility means that the density is not changing over a volume. This is often the case for liquids, like water. However, gases (like air) are compressible, which means that the density can change over the volume. In the case of incompressibility, all partial derivatives of the density equal zero.

Stationary Flow If a flow field is not changing over time, it is called stationary. In these cases, all partial derivatives with respect to time equal zero.

4.1.2. Conservation of Mass (Continuity Equation)

The fact that the mass of a body in motion is not changing over time, is captured in the conservation of mass: the change of mass with time should be zero [58]. Assume a volume $V(\vec{r}, t)$ with position vector $\vec{r}$ at a time t. The mass of this volume can be determined by integrating the density ρ over the volume. To obey the conservation of mass, the derivative of this expression to time should be equal to zero:

$$\frac{d}{dt}\int_{V_t} \rho dV = 0 \tag{12}$$

Above equation is derived by studying an infinitesimal control volume in which mass is flowing in and out. By balancing the mass going in and going out the volume in all directions, one obtains the continuity equation. A more elaborate derivation can be found in [58, 57].

The obtained equation can be rewritten in differential form, using Gauss's divergence theorem ([58]), resulting in the continuity equation:

$$\frac{d\rho}{dt} + \mathrm{div}(\rho\vec{v}) = 0 \tag{13}$$

in which $\rho\vec{v}$ represents the mass flux. For fluids with a constant density (incompressible fluids as described before), this continuity equation reduces to $\mathrm{div}(\vec{v}) = 0$.

4.1.3. Conservation of Momentum

Newton's second law of motion for objects $F = ma$ can also be applied to fluid mechanics, resulting in the conservation of momentum. In [59] a nice derivation is given to obtain the conservation of momentum for fluids. It starts with pointing out all possibilities for momentum transform into or out of a control volume. This can be due to in-/outflowing mass, due to normal and shear forces on the surface of the control volume and due to volume forces (for example gravity). The momentum change is evaluated in each direction separately.

The shear force is indicated by τ_{ij}, where i indicates the normal to the plane in which the shear force is acting and j the direction in the plane in which the shear force is acting. The forces τ_{xx}, τ_{yy} and τ_{zz} are normal forces, which are often denoted with σ_x, σ_y and σ_z respectively.

Examples of volume forces are electrical forces, magnetic forces and gravitational forces. In this research, especially the latter is of importance: $\vec{k}_{grav} = (0, 0, \rho g)^T$ in which g represents the gravitational constant.

Combining all options to gain or lose momentum, results in the balance of momentum [59]:

$$\begin{aligned}
\frac{\partial(\rho u)}{\partial t} &= -\left(\frac{\partial(\rho uu)}{\partial x} + \frac{\partial(\rho vu)}{\partial y} + \frac{\partial(\rho wu)}{\partial z}\right) + \left(\frac{\partial \tau_{xx}}{\partial x} + \frac{\partial \tau_{yx}}{\partial y} + \frac{\partial \tau_{zx}}{\partial z}\right) + k_x \\
\frac{\partial(\rho v)}{\partial t} &= -\left(\frac{\partial(\rho uv)}{\partial x} + \frac{\partial(\rho vv)}{\partial y} + \frac{\partial(\rho wv)}{\partial z}\right) + \left(\frac{\partial \tau_{xy}}{\partial x} + \frac{\partial \tau_{yy}}{\partial y} + \frac{\partial \tau_{zy}}{\partial z}\right) + k_y \\
\frac{\partial(\rho w)}{\partial t} &= -\left(\frac{\partial(\rho uw)}{\partial x} + \frac{\partial(\rho vw)}{\partial y} + \frac{\partial(\rho ww)}{\partial z}\right) + \left(\frac{\partial \tau_{xz}}{\partial x} + \frac{\partial \tau_{yz}}{\partial y} + \frac{\partial \tau_{zz}}{\partial z}\right) + k_z
\end{aligned} \tag{14}$$

In above equations, the left hand side represents the change of momentum in the control volume over time in a certain direction. The right hand side consists of (from left to right) a contribution due to in- and outflowing mass, due to shear forces and due to volume forces.

Because the shear force of a flow field is generally impractical to work with, one can rewrite these in terms of velocity. To do so, one assumes a frictionless flow field, such that all shear forces τ_{ij} with $i \neq j$ vanish. The terms with $i = j$ represent the momentum transport in the normal direction of the plane, which can also happen in frictionless flow fields. Since pressure is acting in all directions, it can be decomposed in the normal forces: $p = -\frac{1}{3}(\tau_{xx} + \tau_{yy} + \tau_{zz})$. The minus sign specifies that the pressure is directed against the boundary of the control volume [59]. Now one can use Stokes' Friction Approach ([60]) to express the shear forces in terms of velocity, using the viscosity η. Taking into account the continuity equation, some terms in the obtained equation vanish.

An elaborate derivation of the conservation of momentum can be found in [59]. Assuming that the viscosity is constant, the following equations can be derived from (14):

$$\begin{aligned}
\frac{\partial(\rho u)}{\partial t} + \frac{\partial(\rho uu)}{\partial x} + \frac{\partial(\rho vu)}{\partial y} + \frac{\partial(\rho wu)}{\partial z} &= -\frac{\partial p}{\partial x} + \eta\left(\frac{\partial^2 u}{\partial x^2} + \frac{\partial^2 u}{\partial y^2} + \frac{\partial^2 u}{\partial z^2}\right) + k_x \\
\frac{\partial(\rho v)}{\partial t} + \frac{\partial(\rho uv)}{\partial x} + \frac{\partial(\rho vv)}{\partial y} + \frac{\partial(\rho wv)}{\partial z} &= -\frac{\partial p}{\partial y} + \eta\left(\frac{\partial^2 v}{\partial x^2} + \frac{\partial^2 v}{\partial y^2} + \frac{\partial^2 v}{\partial z^2}\right) + k_y \\
\underbrace{\frac{\partial(\rho w)}{\partial t}}_{A} + \underbrace{\frac{\partial(\rho uw)}{\partial x} + \frac{\partial(\rho vw)}{\partial y} + \frac{\partial(\rho ww)}{\partial z}}_{B} &= -\underbrace{\frac{\partial p}{\partial z}}_{C} + \underbrace{\eta\left(\frac{\partial^2 w}{\partial x^2} + \frac{\partial^2 w}{\partial y^2} + \frac{\partial^2 w}{\partial z^2}\right)}_{D} + \underbrace{k_z}_{E}
\end{aligned} \tag{15}$$

The terms in above equation represent the time rate of change in flow velocity (A), the convection (B), the influence of pressure gradient on the flow field (C), the internal friction (D) and the volume forces (E) [59].

Above equations can be written in index-notation, resulting in the following:

$$\frac{\partial(\rho U_j)}{\partial t} + \frac{\partial}{\partial x_i}\left(\rho U_i U_j - \eta \frac{\partial U_j}{\partial x_i}\right) = -\frac{\partial p}{\partial x_j} + k_j \tag{16}$$

4.1.4. Conservation of Energy (Equation of State)

A last quantity considered here is energy. Also the amount of energy should be constant in the control volume. An increase or decrease in energy can be due to convection, conduction, boundary forces (for example shear forces), volume energy flow (for example chemical reactions) or work created by volume forces. The total energy of the system consists of internal energy, potential energy and kinetic energy. A complete derivation of the conservation of energy for a control volume can be found in [61], with which the internal energy can be determined. The equation of state is then used to express this internal energy in terms of density, temperature, pressure and velocity (the six unknown variables).

$$\rho c_\mu \frac{\partial T}{\partial t} + \rho c_\mu U_i \frac{\partial T}{\partial x_i} = -P\frac{\partial U_i}{\partial x_i} + \lambda \frac{\partial^2 T}{\partial x_i^2} - \tau_{ij}\frac{\partial U_j}{\partial x_i} \tag{17}$$

From left to right, the energy equation contains the local energy change with time, convection, work due to pressure, diffusion and transfer from mechanical energy into heat.

Above conservation laws can be summarized using a more general notation:

$$\frac{\partial(\rho\Phi)}{\partial t} + \frac{\partial}{\partial x_i}\left(\rho U_i \Phi - \Gamma_\Phi \frac{\partial \Phi}{\partial x_i}\right) = q_\Phi \tag{18}$$

in which $\Phi = [1, U_j, T]$ for respectively the continuity equation, the momentum equation and the energy equation [62]. The variables Γ_Φ and q_Φ also take a different form for the different equations.

4.1.5. Ideal Gas Law

The last equation to solve the system of unknown variables is given by the ideal gas law:

$$pV = nRT \tag{19}$$

in which p again represents the pressure, V the volume and T the temperature. R denotes the ideal gas constant, being 8.314 J/(K mol) and n the number of moles in the gas. [63] Note that this equation is only needed in case of compressible flows. For incompressible flows, the density is constant and this equation is not needed [61].

4.2. Solution Methods

Before a computer is able to handle above equations, they need to be discretized in both space and time. Spatial discretisation can be done by using finite difference, finite element or finite volume methods, based on Gauss Theory [62]. Discretisation in time is divided into explicit methods (using the current state to determine the system at a later time) or implicit methods (depending on both the current state and the state at the later time). For these solution methods, there exists a coupling between solution accuracy and simulation time, linked to the resolution of the solution. When decreasing the grid size, a more realistic solution is obtained, to the cost of computational time. However, when one decreases the computational time by increasing the grid size, the solution becomes less realistic.

The most accurate solution of the problem can be found by using direct numerical simulations (DNS). In these type of simulations, the Navier-Stokes equations are solved without any turbulence model. In other words, turbulence is resolved in the whole range of temporal and spatial scales, from the smallest up to the largest scales. However, in many applications it is too costly to use this approach since the number of iterations scales with Re^3. Therefore, DNS is only suitable for low Reynolds numbers, which is not the case for offshore wind turbines.

Instead, one can use LES (Large Eddy Simulations) to reduce the computational cost. In LES, the smallest length scales are not solved, but modeled. This is done by applying a low-pass filter to the Navier-Stokes equations: it removes all small-scale information by averaging the solution over time and over space. The large scales are solved using equations, while the smallest scales are approximated using a turbulence model. Modelling these smallest scales is justified since the flow structures tend to be similar to each other at these small scales, even in different applications [64].

The computational most efficient approach is to use a Reynolds-averaged Navier-Stokes (RANS) model, which solves the equations only for the mean steady solution and uses turbulence models to approximate all turbulent scales. However, these simulations yield less realistic results compared to DNS or LES.

In this research, LES models are used to study the behavior of the floating platform.

4.3. Courant-Friedrichs-Lewy Condition

The Courant-Friedrichs-Lewy condition (CFL-condition) provides a condition to determine the maximum time step for convergence while solving differential equations [65]. It is based on the dimensionless Courant number C, depending on the mesh size Δx, the time step Δt and the maximum velocity in the domain v_{max}:

$$C = \frac{|v_{max}|\Delta t}{\Delta x} \tag{20}$$

Theoretically, the maximum time step for simulating a stable solution is obtained for a Courant number equal to 1. This value can be explained using the following example: imagine a wave propagating with a speed v. There are different locations, separated with a distance Δx, at which one measures the amplitude of the wave every Δt seconds. The duration between these measurements should be smaller than the time it takes for the wave to move to an adjacent grid point, otherwise the maximum amplitude will not be measured in this grid point. Because of this, a larger grid size allows a larger time step, while decreasing the grid size requires a smaller time step.

Equation 20 represents the Courant number in the one dimensional case. For higher dimensional cases (suppose n-dimensional), the CFL-condition is given as follows:

$$C = \Delta t \left(\sum_{i=1}^{n} \frac{|v_{max_i}|}{\Delta x_i} \right) \leq C_{max} \tag{21}$$

in which Δx_i represents the grid size in the i^{th}-direction, and v_{max_i} the maximum velocity in this direction.

Note that there are multiple ways to define the denoted v_{max}, for example by using the tip speed velocity instead of the flow velocity. In this research, v_{max} is defined as the maximum wind speed.

5. Simulation Tools

To study the dynamics for a floating wind turbine, ASPIRE is used, a software for very precise weather forecasting. A coupling to OpenFAST is established, allowing wind turbine analysis. In this section, both tools will be explained briefly, starting with ASPIRE.

5.1. ASPIRE

The simulations in this research are performed in ASPIRE: the Atmospheric Simulation Platform for Innovation Research and Education. The software is developed by Whiffle ([66]), a company offering very precise weather forecasting to optimize profits of wind and solar farms. ASPIRE is an interface for large-eddy simulations (LES). Whiffle developed their own LES model, called GRASP (GPU-Resident Atmospheric Simulation Platform). This model is based on Graphics Processing Units (GPUs). Most LES models are using Central Processing Units (CPUs) to interpret and execute instructions. Since GPUs are much faster compared to CPUs, ASPIRE offers a very fast way to run LES models. Besides, these GPUs allow visualisations of the LES fields during simulations. ASPIRE runs on Linux operating systems.

To run a simulation in ASPIRE and GRASP, one has to define a `.nml`-file, for example `grasp.000.nml`. This file contains a namelist, consisting of different parts. The options in GRASP are very elaborate, and therefore only the relevant parts for this research will quickly be explained in the bulletpoints below. The underlying physics and the governing equations are nicely explained in [67].

- `&DOMAIN` this section is used to specify the numerical grid. One defines the domain size and the number of grid points in x-, y- and z-direction (the resolution). One can choose for an equidistant grid in z-direction, but also for a grid including percentage growth of cell sizes in vertical direction. Besides, one can specify the latitude and longitude of the domain centre.

- `&LOCATION` the `LOCATION`-section describes the absolute location for each simulation. In this research, the `CCB`-setting is used in all simulations, specifying the centre of the domain.

- `&RUN` in this section, the simulation characteristics are specified, such as the chosen date, the runtime, the maximum time step, the Courant number and the Peclet number. Besides, one can add random perturbations to the simulation by initializing turbulence motions. `irandom` describes the seed of random generator to enable the creation of different random initializations. Furthermore, one can add the magnitude of random perturbations in both specific humidity and in temperature.

- `&INPUTPROF` in this section, the input profile is created by specifying height-dependent variables. For example, one can specify the initial velocity and the geostrophic wind in x- and y-direction, the wind direction, the humidity or the temperature at different heights. One can also introduce tendencies of velocities, humidity or temperature.

- `&PHYSICS` in the `PHYSICS`-part of the namelist, the influence of moisture and Coriolis forces are enabled or disabled. This Coriolis effect is due to the rotation of the earth and causes a deflection of circulating air to the left in the Southern Hemisphere and towards the right in the Northern Hemisphere [68]. Moisture effects are important for the transport of latent heat and they are responsible for the formation of clouds that absorb and reflect solar radiation, affecting the energy balance [69]. In this research, the influences of moisture effects are disabled.

- `&LBC` the lower boundary condition (LBC) is defined in this section. In ASPIRE, this LBC is heterogeneous for each grid box in horizontal direction. There are some predefined boundary conditions, with a prescribed `ilbc`-number, such as a sea surface, or one can use an input file (a netCDF file) to define the lower boundary condition. In this research, the thermodynamic fluxes (both temperature and humidity), the surface roughness lengths (both for momentum and for heat) and the surface pressure are defined for each simulation. Using the Monin-Obukhov similarity theory (see Section 2.1.2), the surface stress is calculated during the simulation.

- `&DYNAMICS` in the `DYNAMICS`-section, the order of the advection schemes for all passive scalars are defined. For example, `iadv_mom`=2 defines a second order scheme for momentum. Instead of momentum, also `thl` and `qt` are used for respectively temperature and specific humidity. In this research, a second order advection scheme is used for both momentum, temperature and specific humidity,

- `&SGSALT` to close the subgrid-scale fluxed for momentum, a certain subgrid scheme is needed. This scheme is specified in `SGSALT`. Possible schemes are Smagorinsky ([70]), Vreman ([71]) or Rozema ([72]). Depending on the chosen scheme, one needs to specify other parameters as well, such as the eddy-viscosity when a uniform scheme is applied. In this research, the Rozema scheme is used, with a dimensionless prefactor of `cs`=0.333.

Above specifications are needed to define a proper simulation. To view, store and analyze the results, the following sections can be added:

- `&STATPROF` to store horizontal average values of different variables, one can use the `STATPROF`-section. One defines the `dtav` and the `dtwrite`, being the amount of seconds in each sample and the amount of seconds in between each storage to a file respectively. For example, `dtav=10` and `dtwrite=100` means that every 10 seconds a sample is taken. After 100 seconds, the 10 obtained samples are averaged and stored to the output file. When the simulation is finished, one obtaines a `graspOut.nml` file including the averaged results for each variable.

- `&STATSLICES` the `STATSLICES`-section can be used to store 3D-variables. One defines the variable(s) of interest, as well as the index (or indices) of cross-section in $x-$, $y-$ and/or $z-$direction. When the simulation is finished, a `graspOutSlices.nml` file is obtained, in which all defined cross-sections are stored. The cross-section of a certain variable ϕ in the (y, z)-plane is specified with $i = ...$ and is denoted with ϕ_yz. Similarly, the indices $j = ...$ and $k = ...$ define a cross-section in (x, z)- and (x, y)-plane and can be found using ϕ_xz and ϕ_xy respectively. Again, one can specify the averaging time.

- `&VIEW` in this section, PNG images can be stored. One can for example define the number of pixels in all directions, the point the camera is looking at (and from), the background color depending on the daytime and the observers orientation.

- `&XCROSS`, `&YCROSS`, `&ZCROSS` to visualize cross-sections of different variables, these `CROSS`-sections can be added. `XCROSS` defines a cross-section in the (y, z)-plane. One can define a variable and a certain grid cell number (for `XCROSS`, one should specify $i = ...$, for `YCROSS` $j = ...$ and for ZCROSS $k = ...$) to display in the ASPGUI. Besides, one can choose a certain colormap.

One can also choose to run multiple simulations simultaneously, on the same GPU. These simulations can be coupled and synchronized. Because of the presence of a wind turbine in the domain, this feature has been very useful in this research. Most simulations in this research have the same set-up: first, a simulation with periodic boundary conditions is run to find proper inflow conditions. This initialisation file is called `grasp.000.nml`. There is no wind turbine included and the simulation continues until it converges to a final flow field. This flow field is then used as input profile for the next simulation, again with periodic boundary conditions. Because there is a turbine involved, one has to prevent that the wake leaving on one side of the domain, enters from the opposite side. Therefore, the simulation consists of an inner domain (cursor simulation, `grasp.100.nml`) and an outer domain (precursor simulation, `grasp.001.nml`). The precursor starts with the obtained flow field from `grasp.000.nml` and continues the simulation in the domain with periodic boundary conditions. This precursor simulation does not feel the presence of a wind turbine. The cursor simulation runs simultaneously and uses the flow field from the precursor as input. The precursors flow field enters the inner domain and the wind turbine causes a wake. This wake does not reach the precursor simulation and therefore the inflow for the cursor remains wake-free.

To define above dependency between the initialising simulation, the precursor and the cursor, the following parts are added to the namelist:

- `&WRITERESTART` to initialize a simulation with the fields of a previous simulation with the same configuration, this section is added to the namelist. By setting the option `lactive` to `true` in the file `grasp.000.nml`, one enables the writing of a restart file, called `graspOutRestart.000.nc`. One specifies the frequency of writing values to this restart file and the desired variables.

- `&READRESTART` The file `graspOutRestart.000.nc` can now be used in the next simulation. The restart variables are specified, as well as the file name with the path to the restart file.

- `&SIMDEP` the dependency of the cursor on the precursor file is specified using the `SIMDEP`-section. In this section, one defines on which `.nml`-file the simulation depends. For example, the cursor simulation `grasp.100.nml` depends on the precursor simulation `grasp.001.nml`. Therefore, in the cursor-file, the following command is used: `depName='grasp.001.nml'`. One can specify a certain time gap between the two simulations by adding `allowedDelay` to control the level of synchronisation (typically a delay in the order of a couple of timesteps). When the domain size and/or the resolution of the dependant simulations are different, linear interpolation is used. The outer region of the dependent simulation (the cursor) is nudged to the corresponding values in the main simulation (the precursor). The strength and the spatial extent of this nudging (or relaxation) is controlled by respectively setting the `nudgeFactor` and the `nudgeExtent`. This `nudgeExtent` is given as fraction of the domain size, meaning that `nudgeExtent>1` implies that the whole domain feels a relaxation term. However, when the value is too small, the cursor might not have enough time or space to relax to the precursor simulation.

5.2. OpenFAST

The analysis for the wind turbine configuration is performed in OpenFAST. A schematic overview of the working of OpenFAST can be found in Figure 9. As one can see, it consists of different modules. The software of OpenFAST is very elaborate and includes a lot of packages and possibilities. In this section, the different modules and their possibilities will be discussed briefly.

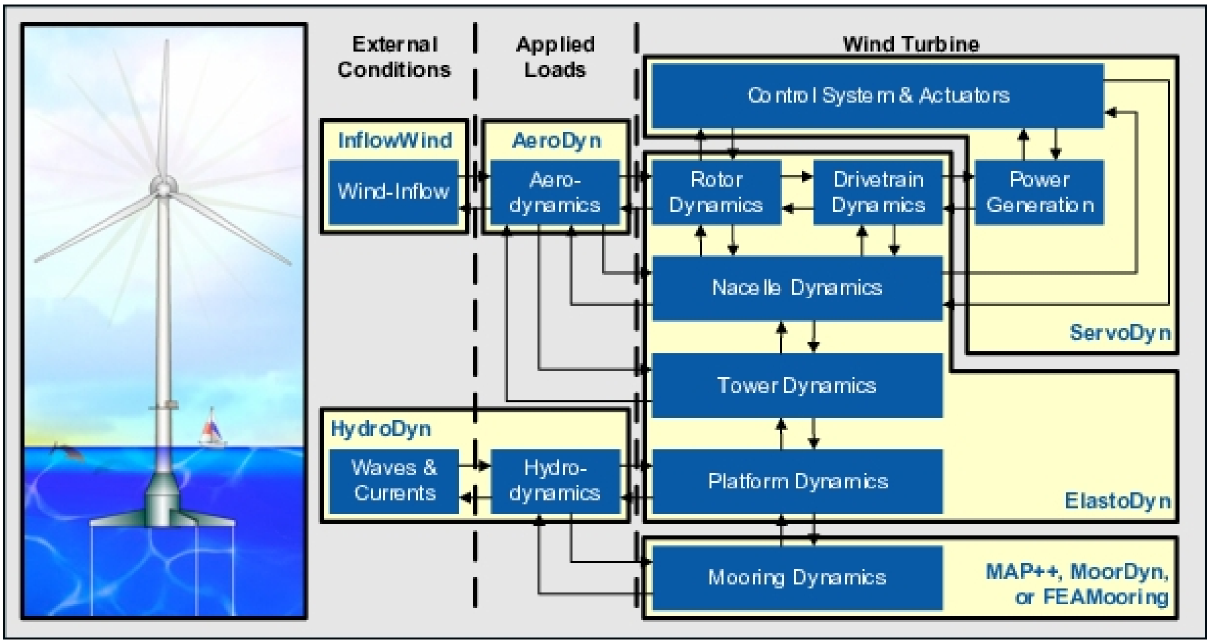

Figure 9: A schematic overview for the working of OpenFast [11].

5.2.1. InflowWind

The InflowWind module is used to generate the undisturbed flow field. In this research, the wind-inflow module is replaced by the wind conditions obtained with GRASP. The coupling is described in detail in Section 5.3.

5.2.2. HydroDyn

The hydrodynamic loads on the structure are calculated in the HydroDyn module. In this module, one can specify some environmental conditions, such as the water density and water depth. Besides, there are different incident wave models to choose from, such as regular waves (periodic) or irregular waves (the JONSWAP/Pierson-Moskowitz or the white noise spectrum). One can also use externally generated waves. Apart from the wave kinematics model, one can specify much more wave parameters, such as the wave direction, the wave spreading, the incident wave elevations or second-order waves. If enabled, the wave elevation output shows the wave movements. One can also choose to disable the wave kinematics, representing still water (no waves).

Also the currents can be specified in the HydroDyn module. One can choose between OpenFASTs standard current profile model, or a user-defined model. In this research, it is assumed that there are no currents. Besides, the platform characteristics are specified in the

HydroDyn module, for example the initial offset of the platform, the used potential-flow model and the additional stiffness and damping.

5.2.3. AeroDyn

The AeroDyn module is used to calculate aerodynamic loads on both the tower and the blades of the turbine, allowing for aero-elastic simulations. Using an actuator line model, the 3D flow around the turbine is approximated with 2D flows at cross sections. All parameters are distributed at nodal points on the blades and on the tower. When coupled to OpenFAST, the module receives the position, the orientation and the velocity at each node and at each time step, including deflections and displacements if desired. It then calculates the aerodynamic loads on all nodes and returns these loads back to OpenFAST, to be used to determine elastic deformations in the ElastoDyn module. The module consists of six submodules, being the rotor wake/induction, the blade airfoil aerodynamics, the tower drag, the aeroacoustics, the bouyance on the blades/hub/nacelle/tower and the influence of the tower on the fluid local to the blade nodes.

The AeroDyn module uses the quasi-steady Blade-Element Momentum Theory (BEM Theory) to calculate the influence of the wake. Using flow local to each node, induction calculations can be performed, resulting in inflow velocities and angles. For high axial induction factors, Glauerts empirical correction is used to replace the linear momentum balance. Optionally, one can choose to apply Prandtl corrections (both for tip- and hub-losses) or Pitt Peters corrections.

For steady blade airfoil aerodynamics, static airfoil data is required, with which the nodal loads are calculated. If one wants to include flow hysteresis, unsteady airfoil aerodynamic models can be used, based on the Beddoes-Leishman theory, with two possible extensions (one developed by González and one developed by Minnema/Pierce).

By using a potential-flow model, the influence of the tower on the fluid is determined, based on the analytical potential-flow solution for flow around a cylinder. One can improve the tower wake by enabling the Bak correction or the tower shadow model.

The AeroDyn module requires airfoil data properties, such as the lift and drag forces for different angles of attack, as well as blade nodal discretizations, buoyancy properties, twist, chord and geometry [11]. Among others, this module returns the rotor speed, the power coefficient, the torque coefficient and the tip seed ratio.

5.2.4. ServoDyn

The ServoDyn module is used to compute control and electrical-drive dynamics. The input file defines the controller options, consisting of different parts. One can, for example, specify the pitch control, the generator and torque control or the nacelle-yaw control. In total, there are 10 control mechanisms which can be disabled or enabled with specified characteristics. A separate file is needed to provide the bladed interface. Here also the minimum and maximum pitch rate and pitch angle are defined, as well as the minimum and optimal generator speed. The ServoDyn module returns among others the generator power and the generator torque.

5.2.5. ElastoDyn

In the ElastoDyb module, the motion of the wind turbine is determined using the aerodynamic forces. In this module, one can specify the degrees of freedom, such as the platform motions, the flapwise and edgewise blade modes, the tower bending modes, the drivetrain rotational-flexibility and the degrees of freedom for the generator and the yaw. One defines initial conditions (such as the initial platform displacement and the initial pitch) and the turbine configurations (such as the number of blades and their cone angles). Also mass and inertia are specified for the blades, hub, generator, nacelle and platform. For each blade, some properties (like the stiffness in edgewise and flapwise direction) need to be defined, as well as the number of nodes per blade. The same applies for the tower. Besides, the rotor-teeter characteristics are defined, such as the used rotor-teeter spring/damper model, its position and the involved constants. The drivetrain is introduced, including gearbox efficiency and gearbox ratio. Using the ElastoDyn module, one can (among others) find the blade pitch, the generator speed and the platform motions.

5.2.6. MoorDyn

In the MoorDyn module the mooring system and the simulation settings can be described. One can for example define line properties (such as the diameter, the stiffness and the mass) and hydrodynamic coefficients. Besides, one can specify connection nodes with which mooring lines can be connected and the number of connections for each anchor. Optionally, one can add seabed properties (such as water depth, bottom damping or bottom stiffness) and initial conditions. If desired, one can find the coordinates, velocities, accelerations, tensions and forces at all connections and lines. [11]

5.3. Coupling between ASPIRE and OpenFAST

As mentioned before, the coupling between ASPIRE and OpenFAST implies that the InflowWind module from OpenFAST is replaced by ASPIRE. GRASP determines the flow field around the turbine and passes the velocities in all directions to OpenFAST. The other modules from OpenFAST then determine the forces on the wind turbine and its position, with which GRASP can determine the flow field around the turbine again. In other words, ASPIRE delivers the proper inflow wind conditions to OpenFAST, which on his turn determines all dynamics around the wind turbine. This iterative loop continues for a certain simulation time at a certain time step. The time step for ASPIRE and the time step for OpenFAST are specified separately in the input files. The chosen time step for ASPIRE should be a multiplier of the time step for OpenFAST to align the obtained forces with the inflow profile. A schematic overview of the coupling between ASPIRE and OpenFAST is shown in Figure 10.

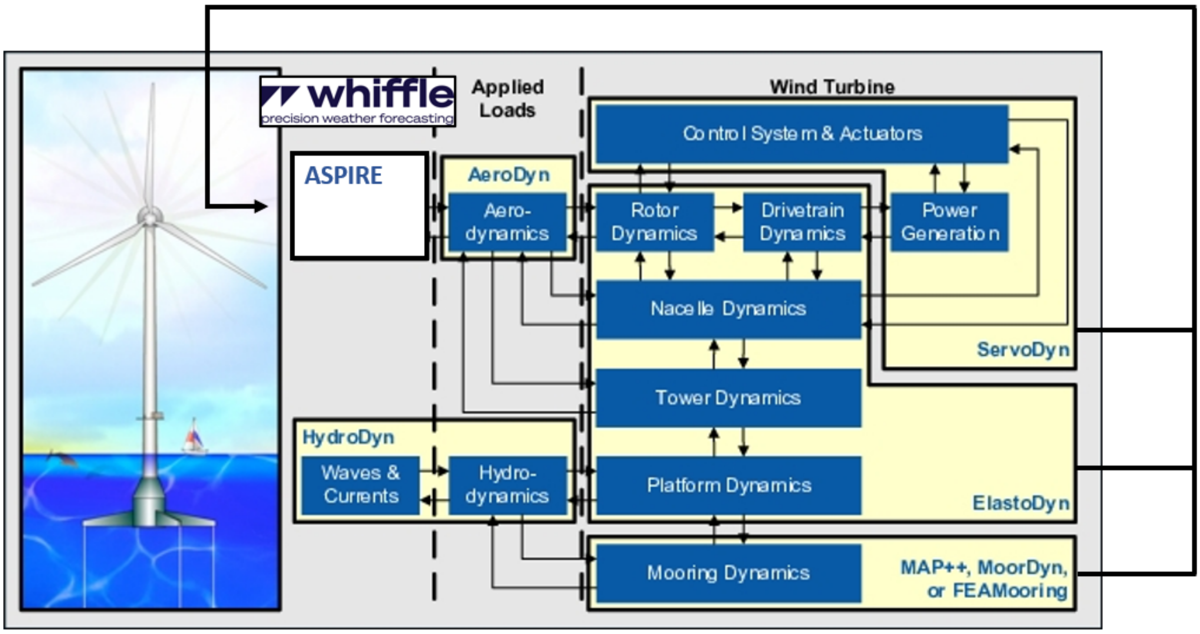

Figure 10: A schematic overview for the coupling of ASPIRE and OpenFAST. Compare with Figure 9 to see the differences with OpenFAST itself.

6. Convergence Study

For solving unsteady, time-dependent problems, it is fundamental to choose a proper time step: it is a balance between realistic dynamics and computational performance. When using a too large time step, the simulation runs quickly, but the flow is modelled inaccurately. However, when reducing the time step, the simulation time will increase. The value for a correct time step depends on the problem, and therefore it is important to find a proper time step for this particular research. In this section, such a time step study is evaluated.

6.1. Method

To find a proper time step for the problem in this research, a simple simulation is used. One single turbine (the 15MW Offshore Reference Wind Turbine on a UMaine VolturnUS-S Semi-Submersible floater) is placed in the domain $(x, y, z) = (1280, 1024, 512)$, at a (x, y)-location of (512, 512), assuming still water conditions. A uniform inflow velocity of 8 m/s is used. Influences from the surface are excluded in the simulation by setting the surface roughness to a very small number ($z_0 = 9.92 \cdot 10^{-5}$). The sub-structural dynamics, the control mechanisms and the influence of the Coriolis force are disabled. Using a relatively short simulation time of 600 seconds in the cursor simulation, different time steps in between $\Delta t = 0.5$ s and $\Delta t = 0.0125$ s are evaluated. One starts with the largest time step and then step-by-step decreases it. When the results are not changing anymore for a decreasing time step, the results are converged and a proper time step is found. A summary of the used parameters is given in Table 3.

parameter	**specification**
wind turbine	IEA Wind 15MW Offshore Reference Wind Turbine [4]
floater type	UMaine VolturnUS-S Semi-Submersible floater [1]
turbine (x, y)-position	512 m × 512 m
simulation time initialisation	7200 s
domain size initialisation	1536 m × 1024 m × 512 m
resolution initialisation	8 m × 8 m × 8 m
simulation time (pre)cursor	600 s
domain size (pre)cursor	1536 m × 1024 m × 512 m
resolution (pre)cursor	8 m × 8 m × 8 m
time step	varying
averaging time cursor	100 s
input velocity	$u_i = 8$ m/s, $v_i = 0$ m/s at all heights
tendency of velocity u	0 m/s^2 at all heights
standard deviation in specific humidity	0 g/kg
standard deviation in specific temperature	0.1 J/(kgK)
Coriolis force	disabled
moisture effects	disabled
surface roughness	$z_0 = 9.92 \cdot 10^{-5}$ m
surface heat flux	0 Km/s
water type	still water

Table 3: The input parameters used for the convergence study for the coupling between ASPIRE and OpenFAST.

6.2. Results

6.2.1. Velocity Profiles

The velocity profiles obtained using above parameters, are shown in Figure 11. As one can see, for each time step, the velocity profiles overlap for $t \geq 200$ s, which means that the velocity field has converged already after 200 seconds for each time step. For time steps in between 0.025 s and 0.4 s, the obtained velocity profiles are very similar, as shown in Figure 12. However, the results for $\Delta t = 0.5$ s are less smooth and are different compared to the results obtained with smaller time steps. This means that a time step of 0.4 s is already small enough to properly capture the flow field.

Remarkable is the fact that for a very small time step of $\Delta t = 0.0125$ s, the results become non-physical: the velocity increases after the rotor, which cannot be the case since energy is subtracted from the flow field. This behavior is due to the control mechanisms as described in the ServoDyn module: when running the same simulation with the control mechanisms disabled, correct results are obtained, as shown in Figure 13. It is not clear why this module causes problems for time steps smaller than 0.02 s. However, because one wants to speed up the simulations as much as possible, it is preferred to choose the largest time step which provides accurate results and therefore it is out of scope of this research to provide more details about this small time step. In further research, one could investigate the problems within ServoDyn to obtain correct results for time steps smaller than 0.025 seconds.

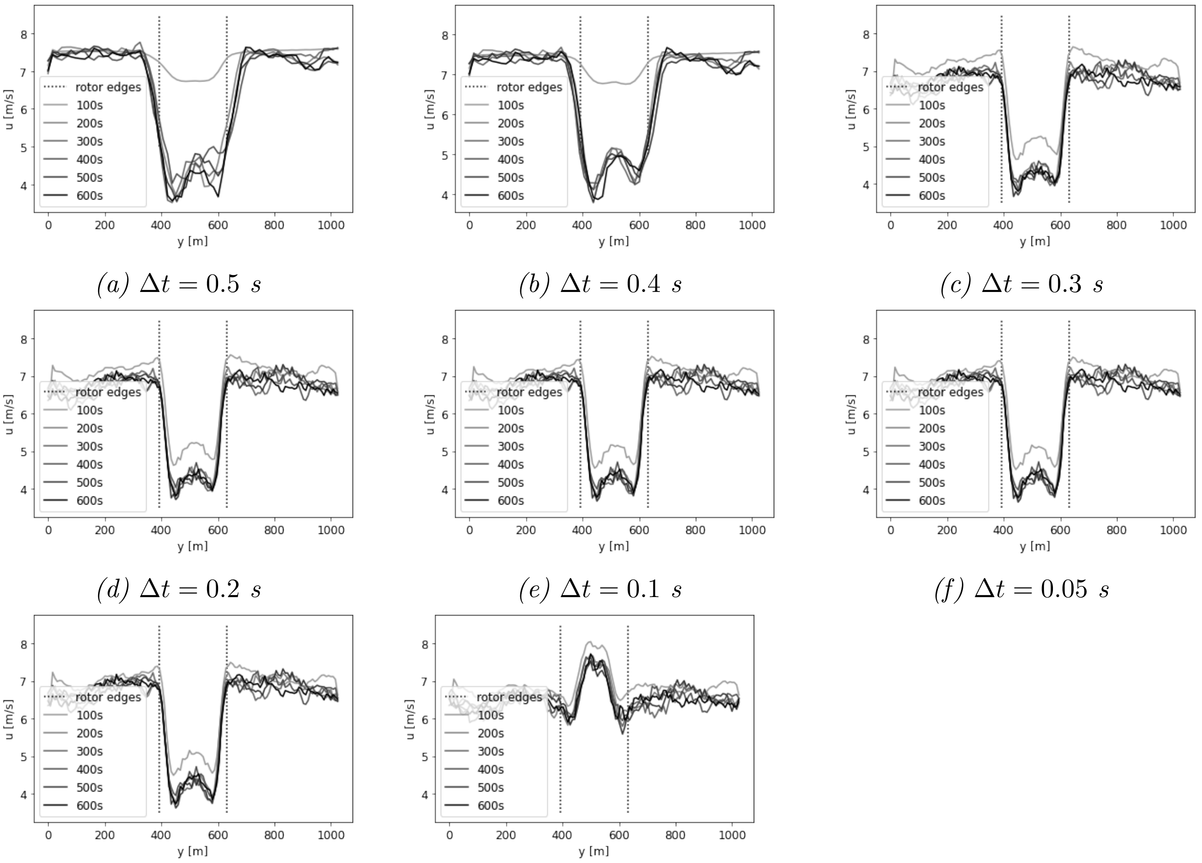

(a) $\Delta t = 0.5\ s$
(b) $\Delta t = 0.4\ s$
(c) $\Delta t = 0.3\ s$
(d) $\Delta t = 0.2\ s$
(e) $\Delta t = 0.1\ s$
(f) $\Delta t = 0.05\ s$
(g) $\Delta t = 0.025\ s$
(h) $\Delta t = 0.0125\ s$

Figure 11: The time-averaged velocity profiles u obtained 2.3D behind the rotor, plotted against the y-axis each 100 seconds, using the settings as described in Table 3. Each subfigure denotes a different time step Δt. The dashed lines represent the rotor edges.

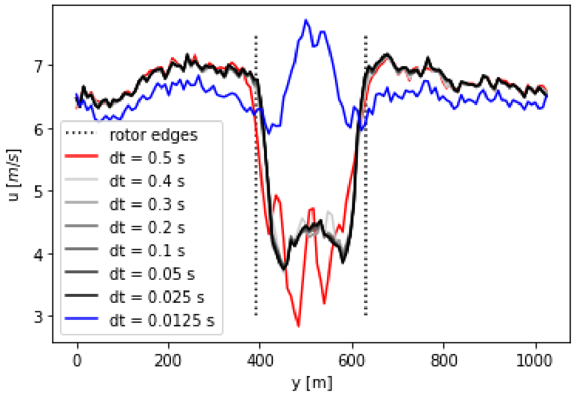

Figure 12: The obtained velocity profile 2.3D behind the rotor for different time steps after 600 s of simulation time.

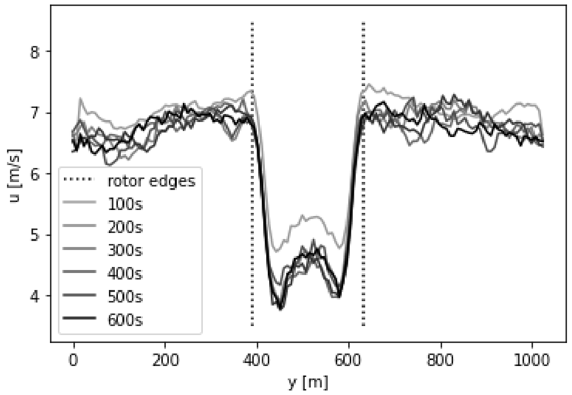

Figure 13: The obtained velocity profile 2.3D behind the rotor for a time step of $\Delta t = 0.0125$ s with the control mechanisms (the ServoDyn module) disabled.

6.2.2. Platform Motions

The obtained platform motions plotted against time for different time steps are shown in Figure 14. As one can see, the curves overlap for time steps in between $\Delta t = 0.025$ s and $\Delta t = 0.2$ s. A time step of $\Delta t = 0.3$ s clearly is too large: when decreasing the time step to $\Delta t = 0.2$ s, the results become very different and thus the platform motions are not converged yet. The graphs for $\Delta t = 0.4$ s and $\Delta t = 0.5$ s show even larger discrepancies and therefore it is chosen to neglect these curves for clarity reasons. Also the curves obtained with a time step of $\Delta t = 0.00125$ seconds are disregarded, because the velocity field analysis already revealed that the results were incorrect.

The differences in the curves for time steps in between 0.025 s and 0.2 s are small: they follow the same shape. Because the velocity field is incorrect for the small time step of $\Delta t = 0.0125$ s with the control mechanisms enabled, it makes sense that also the platform motions show very different results.

For clarity reasons, the obtained platform motions for time steps in between 0.025 s and 0.2 s are plotted in Section A.1. As one can see there, the shapes of the curves are very similar, although the movements for $\Delta t = 0.2$ s are a bit off (especially in roll and heave direction). From these figures, a time step of 0.1 seconds seems a reasonable choice to obtain a good balance between accuracy and costs. In the next section, this guess will be quantified using an error analysis.

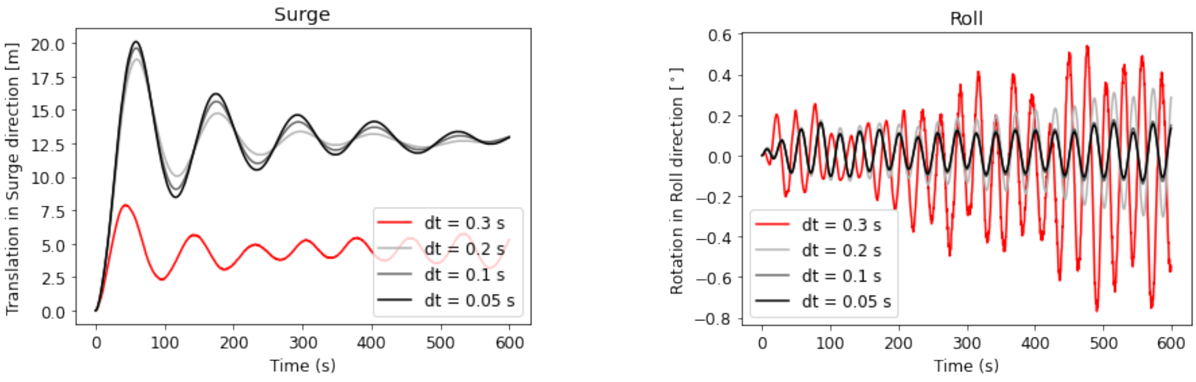

(a) Translation in Surge direction

(b) Rotation in Roll direction

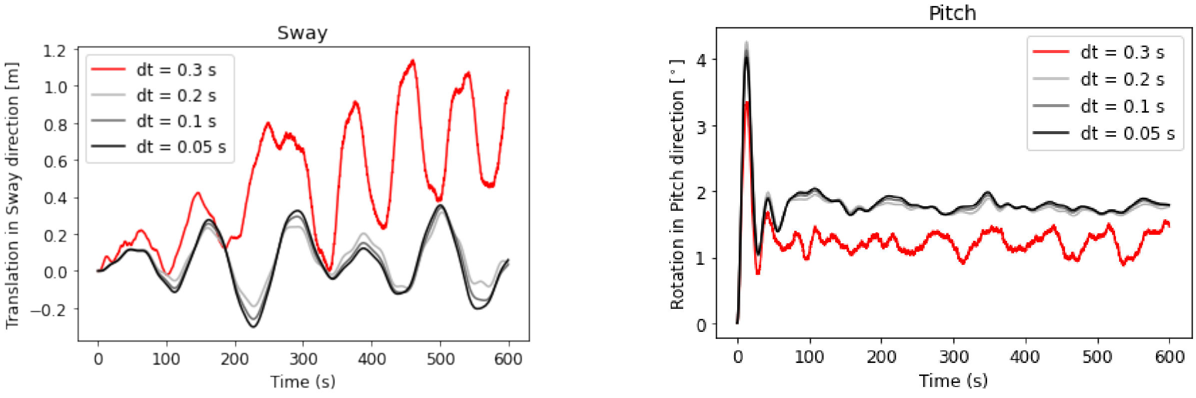

(c) Translation in Sway direction

(d) Rotation in Pitch direction

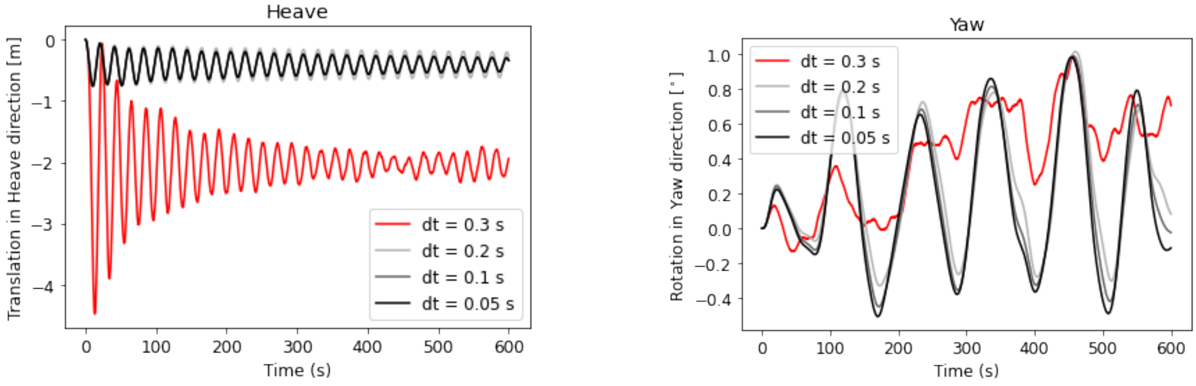

(e) Translation in Heave direction

(f) Rotation in Yaw direction

Figure 14: Platform motions in the six degrees of freedom plotted against the time for different time steps using the settings as described in Table 3.

6.3. Error Analysis

In the previous sections, the time step analysis is performed qualitatively. In this section, the obtained results are compared quantitatively using the root mean square error (RMSE):

$$\mathrm{RMSE} = \frac{\langle|\hat{y}(t) - y(t)|^2\rangle}{\langle|y(t)|^2\rangle} \cdot 100\% \tag{22}$$

in which $y(t)$ represents the real value and $\hat{y}(t)$ the predicted value. Using this RMSE-value, one can quantitatively define the difference between the obtained results for different time steps. In this case, it is assumed that the smaller the time step, the more realistic the solution. Therefore, when comparing, the smaller time step is assumed to give the real results, while the larger time step denotes the predicted results.

Applying above equation to the obtained curves for the platform motions, results in the RMSE-values as given in Table 4. As one can see, the RMSE decreases for decreasing time steps between $\Delta t = 0.3$ s and $\Delta t = 0.025$ s, which is as expected: the smaller the time step, the more it converges to the real solution and thus when decreasing the time step even more, the smaller the obtained differences. Obviously, the RMSE-values for decreasing from $\Delta t = 0.025$ s to $\Delta t = 0.0125$ s are very high due to the non-physical behavior in the control mechanisms for this small time step. Using the RMSE-value, the qualitatively obtained results are confirmed: the shapes of the curves are very similar for all time steps between $\Delta t = 0.025$ s and $\Delta t = 0.2$ s. When increasing the time step from 0.05 s to 0.1 s, the percentages in changes are small, with the largest being 4.3% in sway direction. However, when increasing from 0.1 s to 0.2 s, the percentages are larger, with the largest being 46.9% in roll direction.

In conclusion, it is recommended to use a time step of $\Delta t = 0.1$ s for this simulation with a grid size of $\Delta x = 8$ m, to speed up the simulation as much as possible while still obtaining correct results for the platform motions: decreasing the time step to 0.05 seconds changes the obtained platform motions with only 4.3% in sway direction, and in the other directions even less. When the platform motions are not of interest and one only wants to study the flow field, a higher time step of 0.4 seconds can be used to decrease the computational time.

	Surge	**Sway**	**Heave**	**Roll**	**Pitch**	**Yaw**
from $\Delta t = 0.3$ s to $\Delta t = 0.2$ s	42.4	8857.3	1454.3	1252	10.3	206.1
from $\Delta t = 0.2$ s to $\Delta t = 0.1$ s	0.14	11.4	1.5	46.9	0.1	5.2
from $\Delta t = 0.1$ s to $\Delta t = 0.05$ s	0.06	4.3	0.008	0.3	0.05	1.6
from $\Delta t = 0.05$ s to $\Delta t = 0.025$ s	0.02	1.9	0.01	0.1	0.02	0.5
from $\Delta t = 0.025$ s to $\Delta t = 0.0125$ s	1062.3	103.9	2.8	100.9	244.1	100.2

Table 4: The RMSE for the six degrees of freedom in platform motions, for different time steps, determined using Equation 22. All values are given in percentages.

6.4. Changing Grid Size

Now that a proper time step is found for the simulation using a grid size of 8 m in all directions, it is interesting what happens for other resolutions and their influences on the time step. Therefore, simulations are performed for grid sizes of 16 m and 32 m in all directions. The other parameters as given in Table 3 are unchanged. For these cases with larger grid sizes, very similar results were obtained: the obtained platform motions for $\Delta t = 0.3$ s are very different compared to the motions obtained with time steps in between 0.025 s and 0.2 s. For the region in between 0.025 s and 0.2 s, the shapes were similar, with a small offset for $\Delta t = 0.2$ s. Therefore also for these resolutions a time step of $\Delta t = 0.1$ s is recommended. The obtained platform motions for a grid size of 16 m and 32 m and the obtained RMSE-values when changing the time step can be found in Section A.2.

Again, the error percentages going from $\Delta t = 0.2$ s to $\Delta t = 0.1$ s are large, especially in roll direction with its 57.1% for a grid size of 16 m and 52.3% for a grid size of 32 m. However, when decreasing from $\Delta t = 0.1$ s to $\Delta t = 0.05$ s, the error percentages are small (with the largest being in sway direction with 2.2% and 4.0% for respectively a grid size of 16 m and 32 m). Therefore, a time step of $\Delta t = 0.1$ s is recommended for the simulations of the Umaine VolturnUS S Reference Platform, independent of the grid size.

In Figure 15 one can find the obtained platform motions for the three different grid sizes using a time step of $\Delta t = 0.1$ s. As one can see, the motions are similar in shape, although there are some differences in sign, especially in sway and in yaw direction. This might be due to the randomness in the system. Another option can be that the shape is resolved differently on different grid sizes. Perhaps the turbine "fits" better on a certain coarse resolution than on a slightly higher one. The graphs do confirm that the largest error percentage for all resolutions is obtained in sway direction (see Table 4, Table 15 and Table 16). Also from a physical point of view it makes sense that the largest uncertainty is in this direction: due to the tension in the mooring lines, the gravitational force and the pressure force from the wind, there is less freedom in the other directions.

6.5. Conclusion

In conclusion, a time step of $\Delta t = 0.1$ s gives accurate results in terms of velocity field and platform motions, independent of grid size. Therefore, one can conclude that the CFL-number as introduced in Section 4.3 is not restrictive in these simulations, otherwise the time step would increase for an increasing grid size. The limiting factor for the time step is not due to the coupling of OpenFAST and ASPIRE, but can be found in the software of OpenFAST itself. OpenFAST provides a rule of thumb to determine the maximum time step Δt_{max} for a simulation, being the following [11]:

$$\Delta t_{max} = \frac{1}{10 f_{max}} \tag{23}$$

in which f_{max} denotes the maximum turbine natural frequency. Note that all degrees of freedom are disabled, except for the platform DOF's. Therefore, one should find the highest natural frequency in platform motions, which can be derived from the equations of motion as described in Section 3. The largest natural frequency in the platform degrees of freedom is given in heave direction, with $f = 0.049$ Hz. However, substituting this frequency in above equation results in a maximum time step of 2 s. From the obtained results, it becomes clear that this time step is way too large and one needs a time step in the order of 0.1 s. Therefore, it is expected that is a coupled frequency between the degrees of freedom in the order of 1 Hz to explain the small time step needed to capture accurate results.

At a grid size of 16 m, the platform motions and velocity profiles were obtained correctly, and thus the simulations in this research will be performed using $\Delta t = 0.1$ s and $\Delta x = 16$ m in all directions.

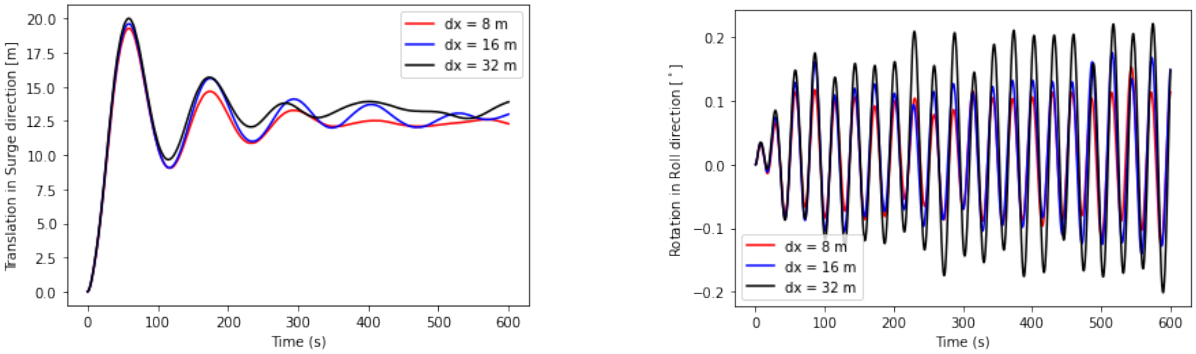

(a) Translation in Surge direction

(b) Rotation in Roll direction

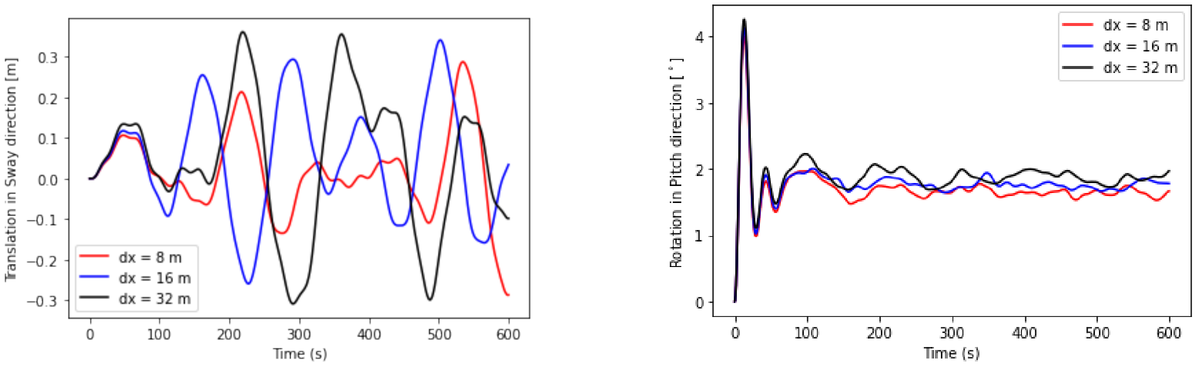

(c) Translation in Sway direction

(d) Rotation in Pitch direction

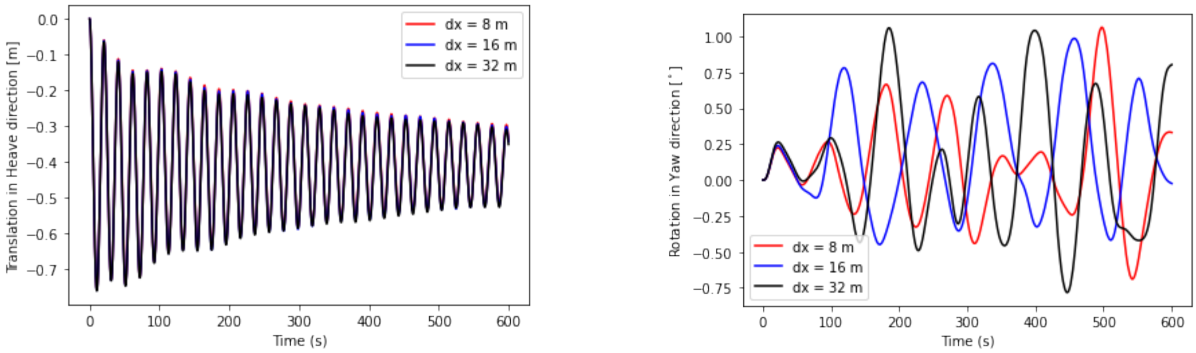

(e) Translation in Heave direction

(f) Rotation in Yaw direction

Figure 15: Platform motions in the six degrees of freedom plotted against the time for a time step of 0.1 s and different grid sizes, using the settings as described in Table 3.

7. Influences of Waves on the Platform Motions

In this section, the influence of wakes on the platform motions is studied and discussed. To this end, an identical simulation is run, one assuming still water and one assuming irregular waves according to the Pierson-Moskowitz wave spectrum. First, some background information about this spectrum is provided, after which the used parameters are given for the simulations, followed by a presentation of the results.

7.1. Pierson-Moskowitz Wave Spectrum

One way to describe the energy distribution within the ocean is the Pierson-Moskowitz spectrum, which is based on a fit to observed oceans with a parameter allowing for a consistent description between sea states. It is an empirical relation, describing the distribution of energy with frequency. In essence, the theory assumes that waves will be in equilibrium with the wind, which is only valid for a fully developed sea: when the wind is steadily blowing over a large area and for a long time. This spectrum is shown in Figure 16, in which one can see the spectral density against the wave frequency for different wind speeds.

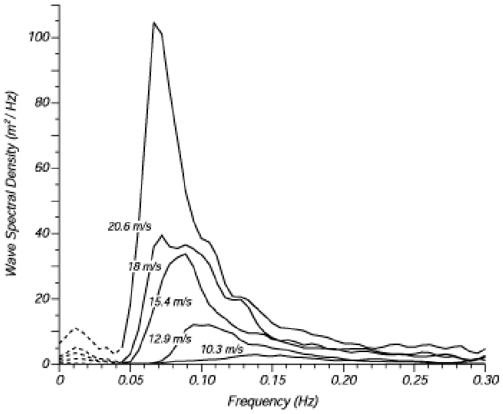

Figure 16: Pierson-Moskowitz wave spectra for a fully developed see at different wind speeds [12].

7.2. Simulation Parameters

The simulation parameters used to study the influence of wakes on the platform motions are shown in Table 5. In the first case, it is assumed that there are no waves (still water). In the second case, the Pierson-Moskowitz spectrum is used to simulate waves. The input parameters for this wave spectrum are presented in Table 6.

The obtained wave profile is plotted in Figure 17, from which it becomes clear that the wave elevation is zero for no waves and nonzero for the Pierson-Moskowitz spectrum, although its mean value also equals zero with a standard deviation of 0.27 m.

7.3. Results

Since the simulation parameters are exactly the same for both simulations except for the wave conditions, the velocity profiles and turbulence intensity are exactly identical, with the same mean value and standard deviation. Also the power outputs are equal to each other: both

parameter	**specification**
wind turbine	IEA Wind 15MW Offshore Reference Wind Turbine [4]
floater type	UMaine VolturnUS-S Semi-Submersible floater [1]
turbine (x, y)-position	384 m × 512 m
simulation time initialisation	30000 s
domain size initialisation	5632 m × 1024 m × 512 m
resolution initialisation	16 m × 16 m × 16 m
simulation time (pre)cursor	3600 s
domain size (pre)cursor	5632 m × 1024 m × 512 m
resolution (pre)cursor	16 m × 16 m × 16 m
timestep	$\Delta t = 0.1$ s
averaging time cursor	100 s
input velocity	$u_i = 11$ m/s, $v_i = 0$ m/s at all heights
tendency of velocity u	$1.8 \cdot 10^{-4}$ m/s^2 at all heights
standard deviation in specific humidity	$2.5 \cdot 10^{-5}$ g/kg
standard deviation in specific temperature	0.1 J/(kgK)
Coriolis force	disabled
moisture effects	enabled
surface roughness	0.0001 m
surface heat flux	0.0 Km/s
water type	case 1: still water case 2: waves according the Pierson-Moskowitz wave spectrum

Table 5: The input parameters used to study the platform motions, flow field and power production of the floating turbine under different atmospheric stability regimes using a simple input profile.

parameter	**specification**
wave stretching	disabled
analysis time for incident wave calculations	850 s
time step for incident wave calculations	0.1 s
peak spectral period of incident waves	8.52 s
peak-shape parameter of incident wave spectrum	1.0 (default for Pierson-Moskowitz)
low cut-off frequency	0.111527 Hz
high cut-off frequency	3.2 Hz
incident wave propagation direction	0.0
directional spreading function	disabled

Table 6: The input parameters for the Pierson-Moskowitz wave spectrum used to study the influence of wakes on the platform motions.

conditions lead to a time-averaged power output of 8.37 MW. The standard deviation in the power output including waves is a bit higher compared to the still water case, being 0.99 MW and 0.94 MW respectively. Using the input parameters as described above, results in the platform motions shown in Figure 18. The grey graph represents the platform motions obtained with the Pierson-Moskowitz wave spectrum and the red graph obtained when assuming still water. The blue graph represents the absolute difference between the two other graphs. As one can see, the obtained platform motions are also similar. In heave direction the absolute difference between the two cases is largest: this motion is smaller in amplitude for still

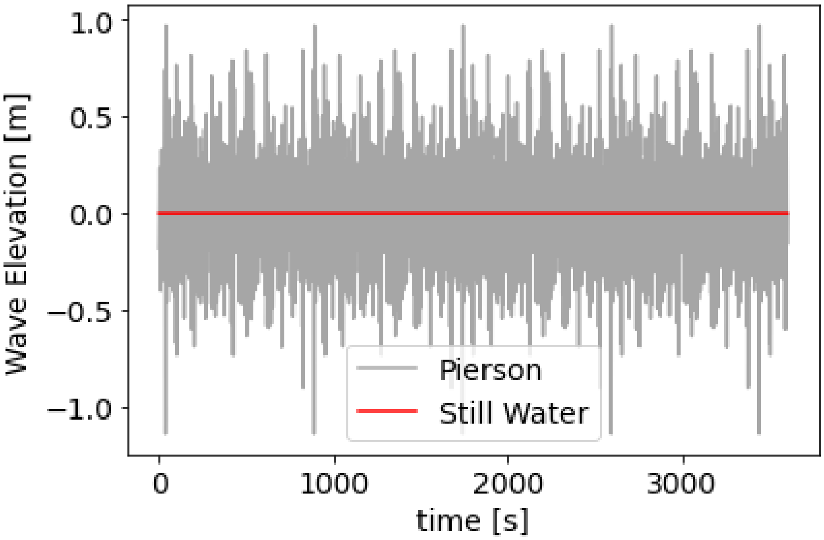

Figure 17: The obtained wave elevation for the two cases: for still water and for the Pierson-Moskowitz wave spectrum.

water than for waves, which makes sense because the waves induce a vertical motion. Also in roll direction, the absolute difference is relatively large. The waves do not influence the platform motions in the other directions.

7.4. Conclusion

Because the influence of waves on the turbines behavior is limited to motions in heave direction, it is chosen to run all simulations in this research assuming still water to speed up the simulation time.

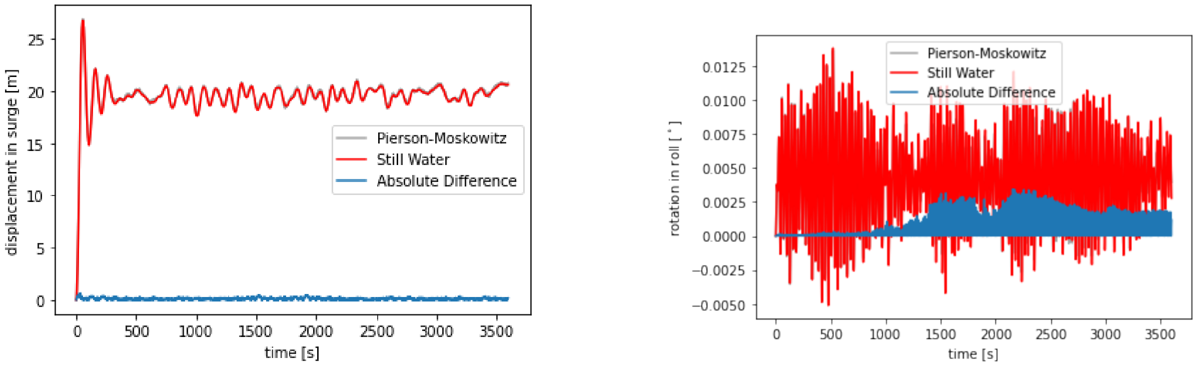

(a) Translation in Surge direction

(b) Translation in Roll direction

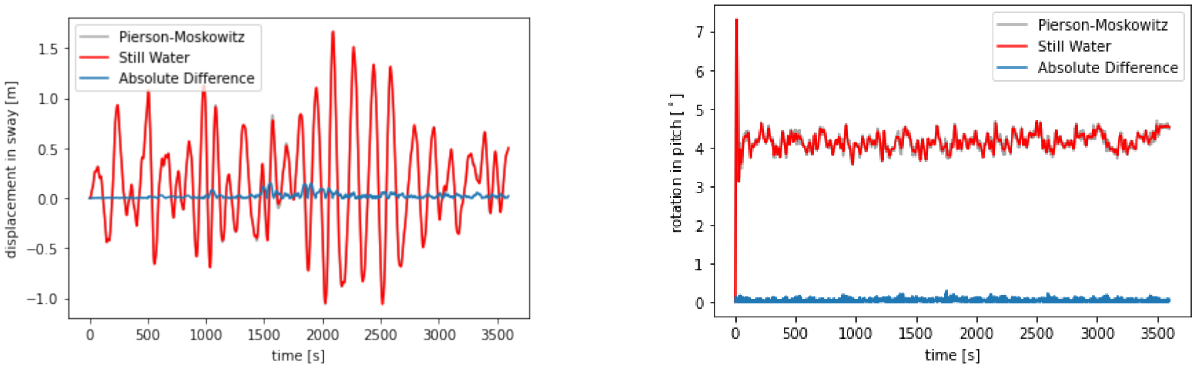

(c) Translation in Sway direction

(d) Rotation in Pitch direction

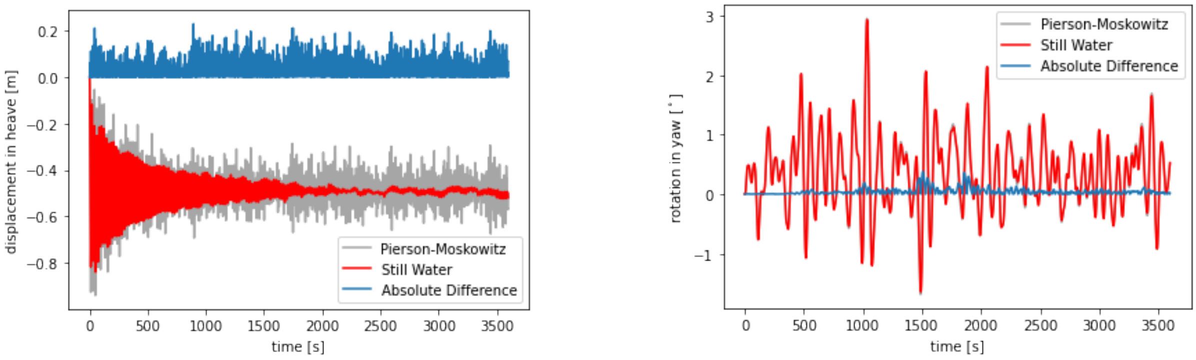

(e) Rotation in Heave direction

(f) Rotation in Yaw direction

Figure 18: Platform motions in the six degrees of freedom plotted against the time for still water (red lines) and for waves according the Pierson-Moskowitz wave spectrum (grey lines). The blue lines represent the absolute difference between the two other graphs.

8. Platform Motions under Uniform Velocity Profiles

In this section, the platform motions of the UMaine VolurnUS S semi-submersible floater is studied under a uniform velocity input profile. Two different cases are compared: one with a uniform input of 8 m/s and one with an input of 15 m/s.

8.1. Method

In a domain of $(x, y, z) = (1280, 1024, 512)$ m a single turbine is located at $(x, y) = (256, 512)$ m. Both simulations have the same input parameters, except for the inflow velocity u_i, which equals 8 m/s in case 1 and 15 m/s in case 2. To make the inflow as simple as possible, an uniform inflow velocity is used. This uniform profile can only be established in LES-models when not modelling turbulence. There is also no modelled turbulence from the subgrid scheme, otherwise one would have shear in the simulations. The surface roughness is set to a very small number ($z_0 = 9.92 \cdot 10^{-5}$ m) to exclude influences from the surface and to increase the wind speed in the lowest grid cell. The magnitude of the random perturbations in both the temperature and the specific humidity equal zero and the Coriolis force is not accounted for. Also the sub-structural dynamics (from `CompSub`) and the control and electrical-drive dynamics (from `CompServo`) are disabled. In the HydroDyn module, still water is assumed (no wave kinematics). The only enabled degrees of freedom are the platform motions. The rotational speed is fixed at 6.34 rpm and the blade pitches are all equal to zero. The precursor has run for 7200 seconds, and the cursor simulation for 3600 seconds, with a time step of 0.1 s and an averaging time of 300 s. The used parameters are summarized in Table 7.

parameter	**specification**
wind turbine	IEA Wind 15MW Offshore Reference Wind Turbine [4]
floater type	UMaine VolturnUS-S Semi-Submersible floater [1]
turbine (x, y)-position	256 m × 512 m
simulation time initialisation	7200 s
domain size initialisation	1280 m × 1024 m × 512 m
resolution initialisation	16 m × 16 m × 16 m
simulation time (pre)cursor	3600 s
domain size (pre)cursor	1280 m × 1024 m × 512 m
resolution (pre)cursor	16 m × 16 m × 16 m
timestep	$\Delta t = 0.1$ s
averaging time cursor	300 s
input velocity	case 1: $u_i = 8$ m/s, $v_i = 0$ m/s at all heights
	case 2: $u_i = 15$ m/s, $v_i = 0$ m/s at all heights
tendency of velocity u	0 m/s^2 at all heights
standard deviation in specific humidity	0 g/kg
standard deviation in specific temperature	0 J/(kgK)
Coriolis force	disabled
moisture effects	disabled
surface roughness	$z_0 = 9.92 \cdot 10^{-5}$ m
surface heat flux	0 Km/s
water type	still water

Table 7: The input parameters used to study the behavior of the floating turbine under uniform velocity input profiles.

After running the precursor simulation using the parameters as described above, one obtains the inflow conditions for the cursor simulation as plotted in Figure 19. As one can see, the flow is very uniform without any perturbations.

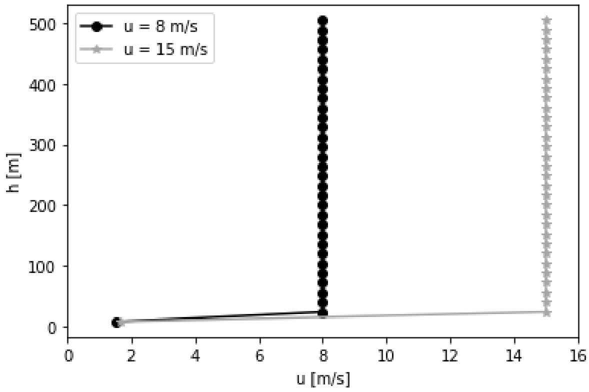

Figure 19: Uniform velocity profiles u plotted against the height h used as inflow conditions for the cursor simulation.

8.2. Results and Discussion

Now that the input profiles are defined, one can start running the simulations for the two different cases and study the results.

8.2.1. Velocity Profiles

Using above velocity profiles as input for the cursor simulation, results in the velocity profiles as shown in Figure 20. These profiles show the velocity along the y-axis at different time steps, measured 2.3D behind the rotor. As one can see, the velocity profiles overlap for $t > 300$ seconds, which means that the solution has converged. Remarkable is the fact that the obtained velocity profiles are not symmetric along the y-axis, although the inflow is uniform. Especially for case 2 ($u_i = 15$ m/s), the difference between the left and the right hand side is large, being $\Delta u = 0.091$ m/s. For case 1 (an inflow velocity of 8 m/s), the asymmetry is less pronounced, being only $\Delta u = 0.015$ m/s. Van der Hoek et al. observed this asymmetry in the wake as well. According to their findings, it is due to vortices shed by the tower interacting with the rotor wake [73]. To validate this reasoning, one could force the turbine to rotate the other way around. Unfortunately, OpenFAST cannot handle negative rotational speeds ([11]) and therefore this simulation cannot be performed in this research.

8.2.2. Platform Motions

The platform motions for the six degrees of freedom over time for the two different cases are visualised in Figure 21. Initially, the platform is located in the origin, so there is no displacement in surge, sway or heave. Besides, the turbine points in vertical direction, so there is no rotation in roll, pitch or yaw direction. When a uniform velocity profile hits the turbine, the platform starts to move in all six directions. Because the platform is mounted to the seabed with mooring lines, there will be a force balance including the tension forces in the mooring lines and the pressure force from the air on the wind turbine, causing damped oscillations in displacements until a steady state position is obtained.

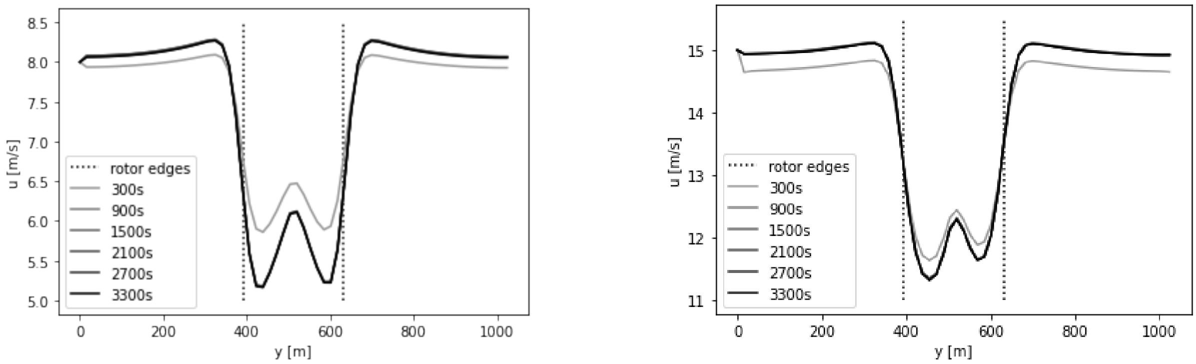

(a) $u = 8$ m/s

(b) $u = 15$ m/s

Figure 20: The velocity profiles at 2.3D behind the rotor at different simulation times, plotted against the y-axis obtained with the settings as described in Table 7 for the two different cases: a) $u_i = 8$ m/s, and b) $u_i = 15$ m/s. The dashed lines represent the rotor edges.

Surge When the simulation starts and the uniform velocity profile hits the turbine, there will be a displacement in surge direction according to Figure 43a. This makes sense when looking at the degrees of freedom for a floating platform as shown in Figure 7. However, due to the mooring lines, the platform is pulled back a little towards its original position. This oscillatory motion continues until the tension forces are in balance with the pressure force from the air. For case 1 ($u_i = 8$ m/s) this final position is located 13.3 m from its original location. For case 2 ($u_i = 15$ m/s), the displacement equals 21.9 m. As expected, the higher the velocity, the larger the displacement in surge direction.

Sway Also in sway direction the displacement is larger for higher velocities: for case 1 the final displacement is only 0.06 m, while it equals 0.66 m for case 2. Besides, one can see much larger oscillatory motions for higher a higher velocity. Compared to the displacement in surge direction, the translation in sway is very small: the translation in sway is only 0.5% and 3% of the displacement in surge for case 1 and case 2 respectively. The motions in sway direction are most likely due to the asymmetry of the velocity profiles as shown in Figure 20. Because the asymmetry is larger for case 2 compared to case 1, also the relative motion in sway direction is expected to be larger. This is indeed the case when looking at Figure 43c.

Heave The platform is moving in surge direction and only a little in sway direction. Because the mooring lines do not change in length, it is therefore expected that the platform experiences a negative displacement in heave direction. This is confirmed by the graph as shown in Figure 43e. Again, the vertical displacement is larger for case 2 compared to case 1, with a final displacement of -0.55 m and -0.41 m respectively.

Apart from above translations, the platform also experiences rotational displacements.

Roll In roll direction, the platform rotates with respectively 0.09° and 0.72° for case 1 and case 2 according to Figure 43b. This rotation is linked to the translation in sway, and therefore also due to the asymmetry in the velocity profile. Note that the amplitude of the oscillatory motion is larger for an input velocity of 8 m/s compared to 15 m/s.

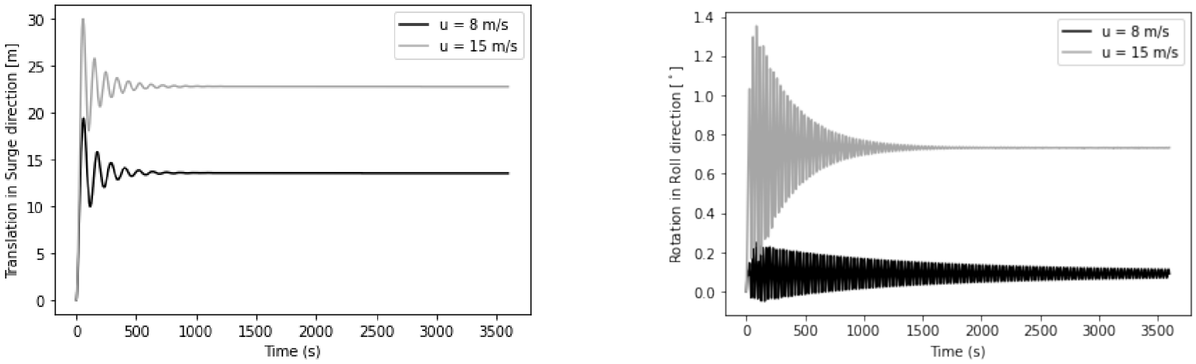

(a) Translation in Surge direction

(b) Rotation in Roll direction

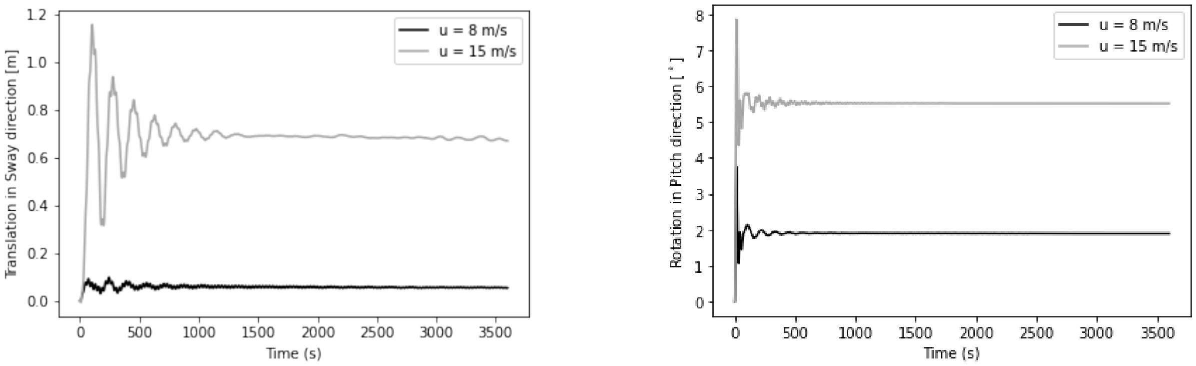

(c) Translation in Sway direction

(d) Rotation in Pitch direction

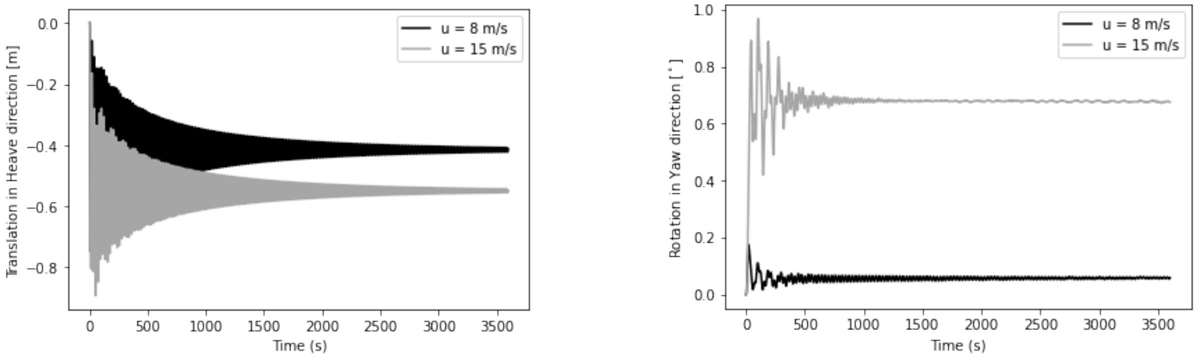

(e) Translation in Heave direction

(f) Rotation in Yaw direction

Figure 21: Platform motions in the six degrees of freedom plotted against the time obtained for the two cases with the settings as described in Table 7.

Pitch The rotation in pitch direction is much larger, as shown in Figure 43d: 1.9° for case 1 and 5.5° for case 2. With its hub height of 150 m and a radius of 120 m, the blade tip hits 270 m. The obtained pitch angles therefore imply a horizontal difference of respectively $270 \times \sin(1.9) = 9.0$ m and $270 \times \sin(5.5) = 26$ m between the blade tip at its highest position and the platform origin.

Yaw In yaw direction, the rotations are smaller again, with 0.06° in case 1 and 0.66° in case 2. The mean of the oscillatory movements for rotations in roll and in yaw directions are much higher for higher velocities compared to lower velocities. However, the amplitude of the oscillatory motion in roll direction is larger for the lower velocity for $t > 1000$ seconds, being .

8.2.3. Natural Frequencies

From the obtained oscillatory motions plotted in Figure 21 one can deduce the natural frequencies in each degree of freedom. In this section, the natural frequencies in each degree of freedom are determined and discussed. To find the natural frequency in each degree of freedom, a sine-function is fitted to the graphs in Figure 21 using the optimisation toolbox in Python [74]. The following function is fitted to the platform motions:

$$A \sin\left(2\pi f(t + t_0)\right) + C \tag{24}$$

in which the fitting parameters are A (the fitted amplitude), f (the fitted frequency), t_0 (the horizontal offset) and C (the vertical offset). The value for f is assumed to be the natural frequency. A visualisation of the sine-fitting to the obtained platform motions for an input velocity of 8 m/s can be found in Section A.3.

Surge and Sway According to the free-decay tests performed by Allen et al. the natural frequencies in surge and sway direction are given by 0.007 Hz (and thus a period of approximately 143 seconds). When fitting a sine-function to the graphs in Figure 43a and Figure 43c, one obtains a natural frequency of 0.0089 Hz ($T = 113$ seconds) in surge direction and 0.0063 Hz ($T = 159$ seconds) in sway direction for an input velocity of 8 m/s. For 15 m/s, the natural frequency is 0.0079 Hz ($T = 126$ seconds) in surge and 0.0058 Hz ($T = 172$ seconds) in sway. Therefore, one can conclude that the natural frequency depends on the wind speed: the natural frequency slightly decreases for higher wind speed for surge and sway direction.

Heave The frequency with which the platform is moving in heave direction is much higher compared to the oscillations in surge or sway direction. This is in line with the natural frequencies as given in Table 2 from the free-decay tests performed by Allen et al [1]: for surge and sway direction, the natural frequency equals 0.007 Hz, while it is 0.049 Hz in heave direction (a period of 20 seconds). Fitting a sine-function to the platform motions in heave direction results in an equal oscillatory frequency for all wind speeds, with a period of 20.6 seconds ($f = 0.049$ Hz).

Roll In roll direction, the natural frequency is high: it has a period of 28.8 seconds, which corresponds to a frequency of 0.035 Hz. The wind velocity barely influences the frequency in roll direction. However, for low velocities, the platform keeps oscillating in roll direction with a sinusoidal shape between 0.07° and 0.11°, as shown in Figure 22b. The amplitude with which the platform keeps oscillating for higher wind speeds is much smaller.

Pitch In pitch direction, the oscillation is damped much faster compared to the roll or yaw direction. It is difficult to see the periods in pitch direction from this graph. A zoomed in version is shown in Figure 22c, in which one can clearly see 2 oscillations, after which it becomes more chaotic. Fitting sine-function to the obtained platform motion in pitch direction, results in a period of 28 seconds, independent of wind speed. This corresponds to a natural frequency of 0.036 Hz, which is similar to the natural frequency obtained with free-decay tests.

Yaw Also in yaw direction it is difficult to see clear oscillations. In Figure 22d, the first 300 s of the simulation are shown, in which one can see a large oscillation. Fitting a sine-function to the obtained platform motions in yaw direction, results in a natural frequency of 0.012 Hz for a wind speed of 8 m/s and 0.013 Hz for a wind speed of 15 m/s.

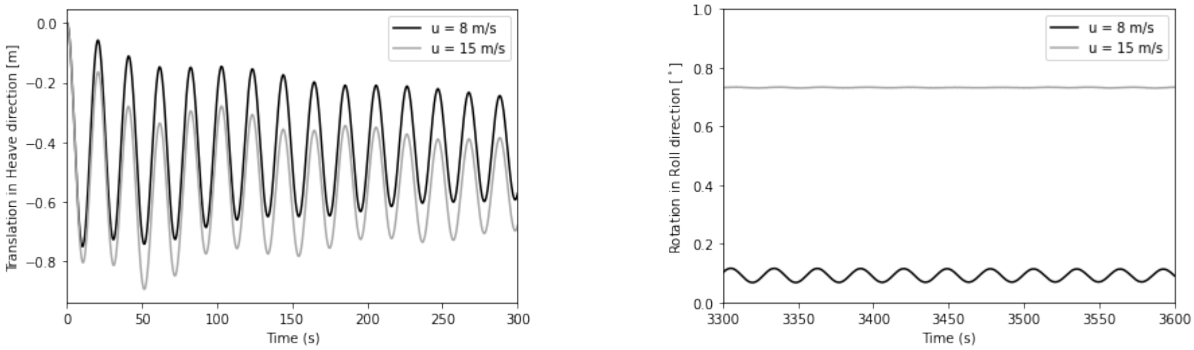

(a) Heave motions for the first 300 seconds of the simulation. The oscillatory frequency is equal for both input profiles.

(b) Roll motions for the final 300 seconds of the simulation to visualise the oscillation for the input profile of 8 m/s.

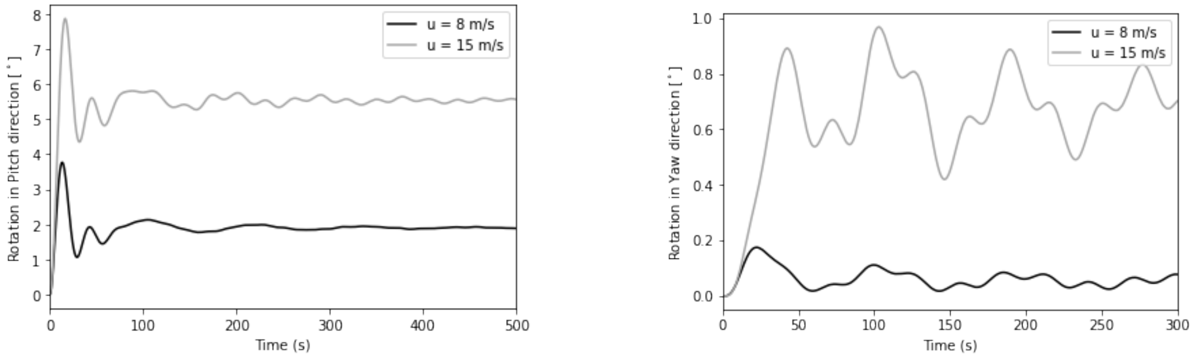

(c) Pitch motions for the first 500 seconds of the simulation. It is hard to distinguish an oscillatory motion.

(d) Yaw motions for the first 300 seconds of the simulation to visualize the large oscillatory motions.

Figure 22: The same figures as shown in Figure 21 but then zoomed-in to better visualise the shapes of motions.

A summary of the obtained natural frequencies compared with the measured frequencies form Allen et al. is presented in Table 8. The absolute error percentages ϵ are determined using the following equation:

$$\epsilon = \left| \frac{f_{obtained} - f_{real}}{f_{real}} \right| \cdot 100\% \tag{25}$$

As one can see, large error percentages are obtained in surge, sway and yaw direction. This makes sense, since these movements depend on the wind velocity: the obtained natural frequencies are determined using an inflow wind of 8 m/s, while the free-decay tests are performed assuming a still wind environment and therefore some deviations are expected. The natural frequencies in heave, roll and pitch do not depend on wind velocity and therefore these frequencies have much smaller error percentages when comparing to the results from the free-decay tests.

DOF	Obtained Natural Frequency	Free-Decay Natural Frequency	Absolute Percentage Error
Surge	0.009	0.007	29%
Sway	0.006	0.007	14%
Heave	0.049	0.049	0%
Roll	0.035	0.036	3%
Pitch	0.036	0.036	0%
Yaw	0.012	0.011	9%

Table 8: A comparison of the obtained natural frequencies (GRASP and OpenFAST with an inflow velocity of 8 m/s) and the results from the free-decay tests (performed by Allen et al., [1]) in the six degrees of freedom (DOFs) with their absolute error percentages calculated using Equation 25. All frequencies are given in Hz.

8.3. Conclusion

When a floating platform with a wind turbine is at rest and a uniform inflow profile hits the tower, the platform starts oscillating in the six degrees of freedom until it reaches an equilibrium between the pressure force from the wind, the friction force of the platform and the tension force in the mooring lines. The largest displacement is obtained in surge direction and the largest rotation in pitch direction. The higher the inflow velocity, the larger the amplitude of translation and rotation. From the oscillatory platform motions, one can determine the natural frequency in each degree of freedom by fitting a sine-function to the obtained graphs. The fitted frequencies correspond to the natural frequencies obtained with free-decay tests performed by Allen et al. [1], with the largest absolute percentage error in surge direction being 29%.

9. Platform Motions under Sinusoidal Wind Fluctuations

Now, a wind fluctuation is added to the uniform velocity profile in the form of a sine-function with a period T and an amplitude A added the pressure terms in the Navier-Stokes equation as presented in Equation 15 in $x-$ and y-direction. In z-direction, nothing changes. A summary of the added terms is given below:

$$\begin{aligned} \frac{\partial p}{\partial x} &\quad\rightarrow\quad \frac{\partial p}{\partial x} + A_u \sin\left(\frac{2\pi}{T_u} t\right) \\ \frac{\partial p}{\partial y} &\quad\rightarrow\quad \frac{\partial p}{\partial y} + A_v \sin\left(\frac{2\pi}{T_v} t\right) \\ \frac{\partial p}{\partial z} &\quad\rightarrow\quad \frac{\partial p}{\partial z} \end{aligned} \tag{26}$$

The variables A_u, A_v, T_u and T_v are given as input in ASPIRE. The other input parameters are given in Table 9.

parameter	**specification**
wind turbine	IEA Wind 15MW Offshore Reference Wind Turbine [4]
floater type	UMaine VolturnUS-S Semi-Submersible floater [1]
turbine (x, y)-position	512 m × 512 m
simulation time initialisation	$40 \times T$ s
domain size initialisation	1536 m × 1024 m × 512 m
resolution initialisation	16 m × 16 m × 16 m
simulation time (pre)cursor	9000 s
domain size (pre)cursor	1536 m × 1024 m × 512 m
resolution (pre)cursor	16 m × 16 m × 16 m
timestep	$\Delta t = 0.1$ s
averaging time cursor	60 s
input velocity	$u_i = 7$ m/s, $v_i = 0$ m/s at all heights
tendency of velocity u	$8 \cdot 10^{-5}$ m/s^2 at all heights
standard deviation in specific humidity	$2.5 \cdot 10^{-5}$ g/kg
standard deviation in specific temperature	0.1 J/(kgK)
Coriolis force	disabled
moisture effects	enabled
surface roughness	$z_0 = 0.0001$ m
surface heat flux	0 Km/s
water type	still water

Table 9: The input parameters used to study the platform motions of the floating turbine under sinusoidal wind fluctuations.

For a period of $T = 800$ s and a sine amplitude of $6 \cdot 10^{-3}$ kg/(m^{2}s^2) under the parameters as given in Table 9, one obtains the velocity input profiles as shown in Figure 23. The left figure represents the input profile for a sinusoidal wind fluctuation in x-direction (surge direction) and the right figure the profile for a fluctuation in y-direction (sway direction). The next step is to simulate the behavior of the floating platform under these input profiles.

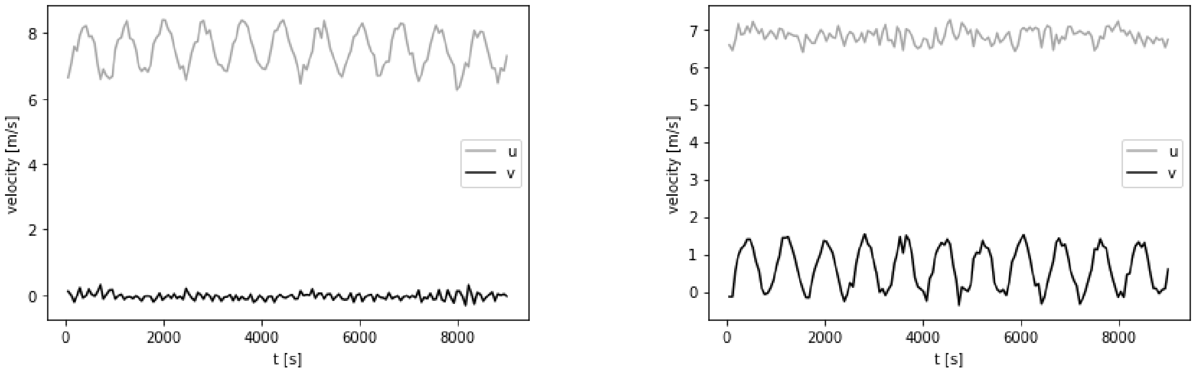

(a) Sinusoidal Fluctuation in u

(b) Sinusoidal Fluctuation in v

Figure 23: The input velocity at hub height in horizontal and vertical direction (u and v) plotted against time for a sinusoidal wind fluctuation in x- (left figure) and in y-direction (right figure).

9.1. Theory and Method

The method to quantify the behavior of the floating platform is the following:

1. Choose a certain period T
2. Run the first simulation (`grasp.000.nml`) to initialize the sinusoidal input profile
3. Run the second simulation consisting of a precursor (without turbine, `grasp.001.nml`) and a cursor (with turbine, `grasp.100.nml`) using the results of the previous step as input profile
4. Fit a sine-function with period T to the velocity at the rotor obtained from `grasp.001.nml` (the precursor: this domain does not feel the presence of the wind turbine). Also fit a sine-function to the obtained platform motions from `grasp.100.nml` (the cursor: with turbine). The sine-function to fit looks as follows:

   $$A \sin\left(\frac{2\pi}{T}(t + t_0)\right) + C \tag{27}$$

   The fitting variables are the amplitude A, the horizontal offset t_0 and the vertical offset C. The optimal values for these parameters and their variances σ^2 are determined using the `scipy.optimize.curve_fit()` function in Python [74]. The period T is forced to the chosen period from step 1.
5. Store the obtained amplitude, horizontal offset and vertical offset for the input profile and for the six degrees of freedom in a matrix, as well as the obtained variances in these fitting parameters.
6. Start again from step 1 choosing a different period.

9.1.1. Examples Sine-Fitting

A zoomed in version of the velocity profiles as shown in Figure 23 is plotted in Figure 24, as well as the fitted sine. In the remainder of this chapter, a gust in x-direction (fluctuation in u) is marked with blue lines and in y-direction (fluctuation in v) with red lines. As one can see, the fitted sines describe the input profile very good.

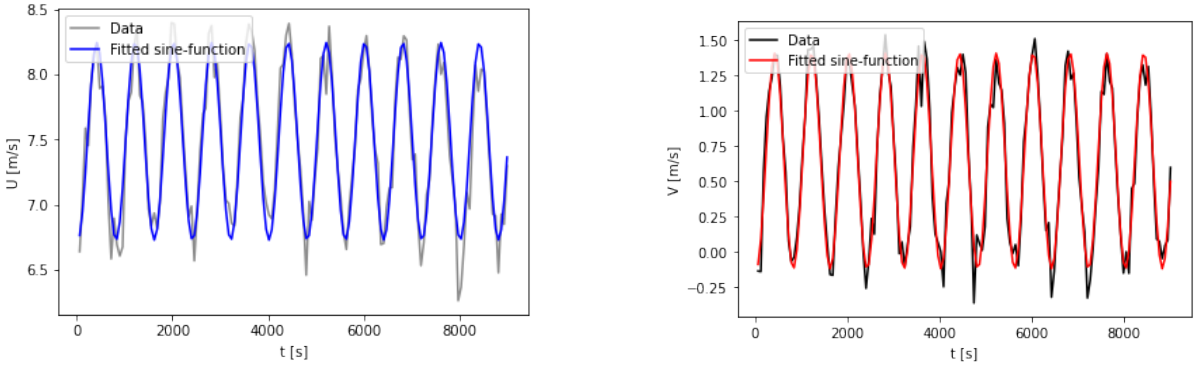

(a) Sinusoidal Fluctuation in u

(b) Sinusoidal Fluctuation in v

Figure 24: The input velocity profiles for a sinusoidal wind fluctuation in x- and in y-direction (in u and in v) plotted against time including the fitted sine function.

The sine-fitting to the platform motions for these input profiles results in the graphs as shown in Figure 25 and Figure 26. The grey lines represent the obtained platform motions, the blue and red lines the fitted sine functions. Note that the rotational motions in roll, pitch and yaw are translated into meters by calculating the displacement d at hub height h for the obtained angle α:

$$d = h \sin \alpha \tag{28}$$

Comparing the fitted functions for a fluctuation in u and in v, one can clearly see a difference in the amplitude for each degree of freedom. For example, the amplitudes in surge and pitch direction are much larger for a fluctuation in u compared to a fluctuation in v, whereas it is the other way around for the amplitude in yaw direction. For the other graphs the difference in response is less pronounced.

9.1.2. Response Function and Phase Difference

Repeating the sine-fitting process for different periods, results in three big matrices in u and in v containing the fitted amplitude and offsets for the input velocity profile and the platform motions and three big matrices containing their variances. To quantify the difference in response for a fluctuation in u and in v, the response function H and the phase difference $\Delta\phi$ can be used, given by the following expressions:

$$\begin{aligned} H &= \frac{A_{\text{out}}}{A_{\text{in}}} \\ \Delta\phi &= \phi_{\text{in}} - \phi_{\text{out}} \\ &= \frac{2\pi}{T}\left(t_{0,\text{in}} - t_{0,\text{out}}\right) \end{aligned} \tag{29}$$

in which $(.)_{out}$ denotes the output profile of the platform motion in a certain direction and $(.)_{in}$ the input velocity profile. The fitted amplitude determines the response function H. Because

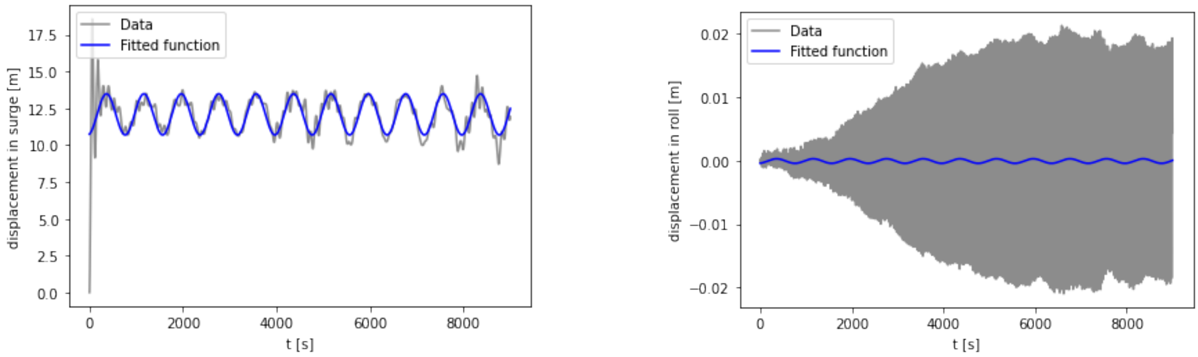

(a) Translation in Surge direction *(b) Translation in Roll direction*

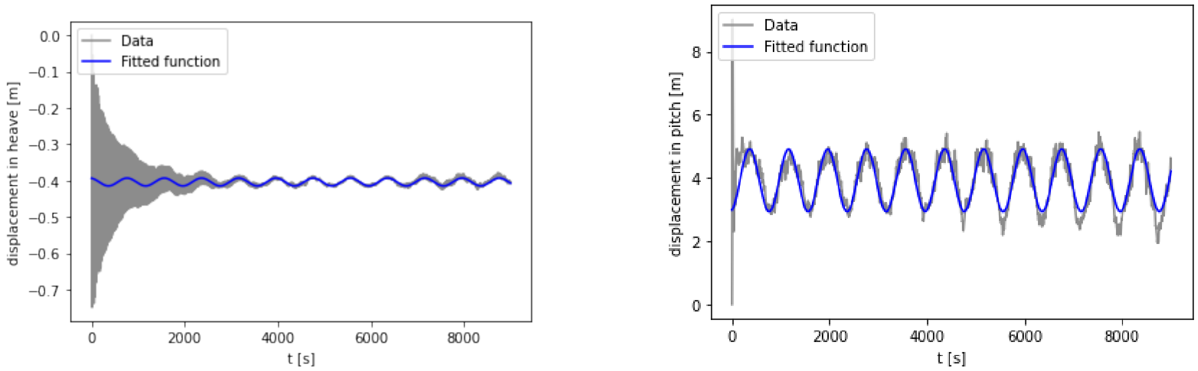

(c) Translation in Sway direction *(d) Translation in Pitch direction*

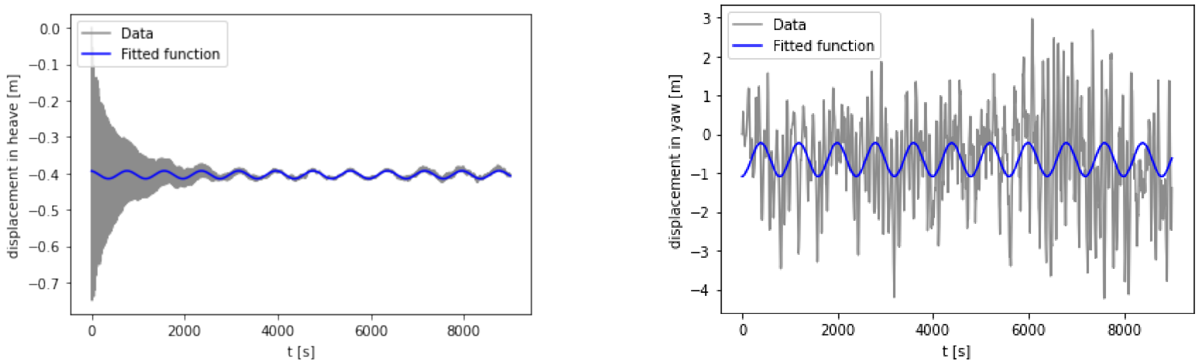

(e) Translation in Heave direction *(f) Translation in Yaw direction*

Figure 25: Platform motions in the six degrees of freedom plotted against the time under a sinusoidal wind fluctuation in u with a period of $T = 800$ s using the settings as described in Table 9 including the fitted sine.

the amplitude of motion is directly related to the amplitude of the input variable (the larger the velocity, the larger the translation in for example surge direction), the fitted output amplitude is divided by the fitted input amplitude, such that the obtained amplitudes can be compared to each other. The response H is therefore given in m/(m/s), representing the displacement of the platform for a wind ramp of 1 m/s. If the platform motion is not influenced by the sinusoidal fluctuation input profile, H tends to go to zero. The larger the value of H, the larger the response: the amplitude of the input profile is translated into an amplitude of the platform motion. One would therefore expect a low-pass filter for the response: for very high frequencies, the fluctuation is too fast for the platform to follow the

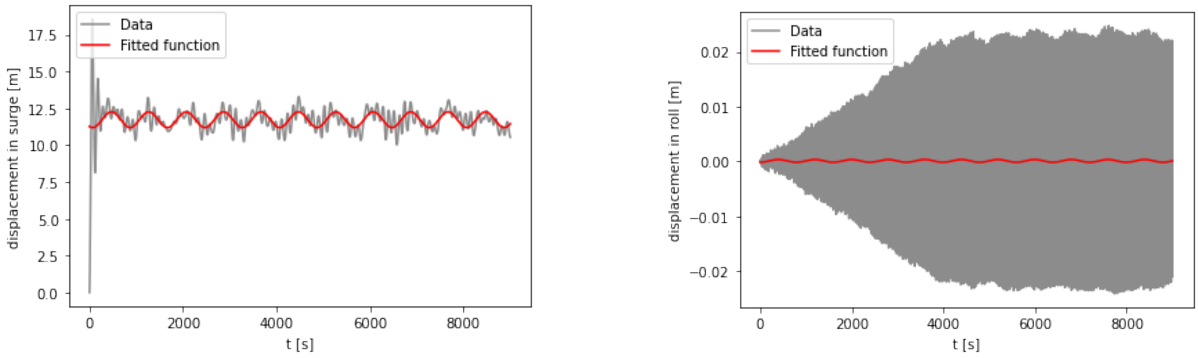

(a) Translation in Surge direction

(b) Translation in Roll direction

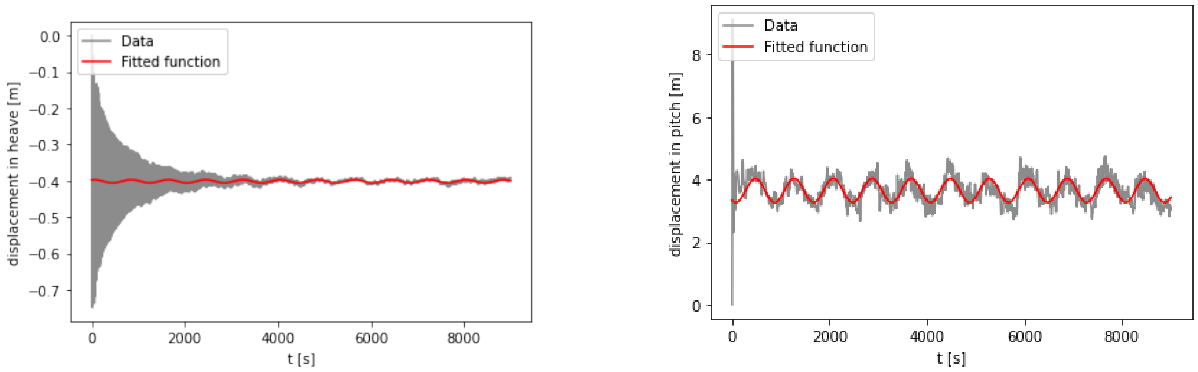

(c) Translation in Sway direction

(d) Translation in Pitch direction

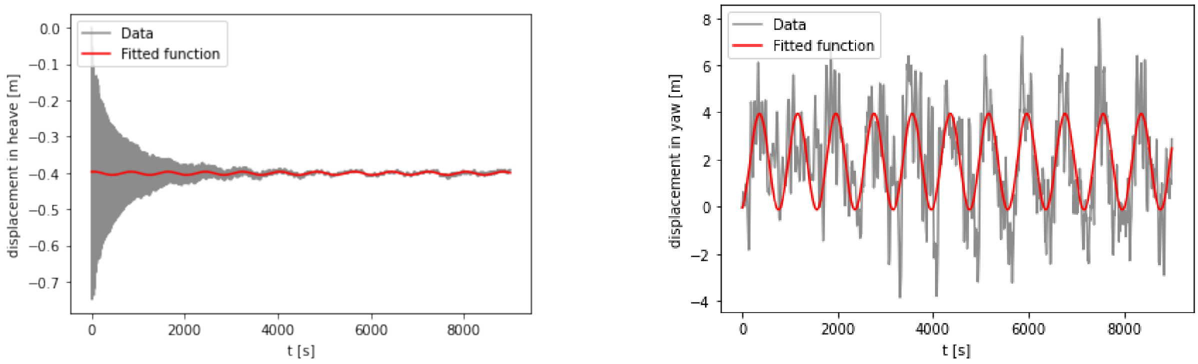

(e) Translation in Heave direction

(f) Translation in Yaw direction

Figure 26: Platform motions in the six degrees of freedom plotted against the time under a sinusoidal wind fluctuation in v with a period of $T = 800$ s using the settings as described in Table 9 including the fitted sine.

movements and thus H tends to zero. For very low frequencies, the turbine has time enough to adapt to the change in velocity and therefore the turbine motions will have a similar oscillation as the input profile, and thus H will be non-zero.

One can also study the phase difference $\Delta\phi$ between the input velocity profile and the obtained platform motions by subtracting the phase ϕ of the platform motion from the input profile. This ϕ is obtained from the fitted t_0 via $\phi = \frac{2\pi}{T}t_0$, given in radians. If $\Delta\phi$ tends to zero, the platform motion is in phase with the input profile. If it tends to $\pm\pi$, the motions are out of phase. One would expect a zero phase difference for very low frequencies since the motion is in phase with the velocity input. For higher frequencies, the phase difference is nonzero because the motion and the inflow are not aligned. Note that a sine-function is periodic with 2π, such that an obtained phase of $-\pi$ is equal to a phase of π.

9.2. Results and Discussion

Calculating the response and the phase difference at different frequencies $\omega = 2\pi/T$ for each degree of freedom results in the plots as shown in Figure 27. The blue lines represent a sinusoidal fluctuation in u and the red lines a fluctuation in v. The responses H are plotted on a log-log scale in the upper graphs and the phase differences on a semilog scale in x-direction in the lower graphs. The black vertical lines denote the natural frequency for each degree of freedom as given in [1]. The coloured dashed lines and the black crosses and triangles are obtained using an error analysis, which will be explained in detail in Section 9.3.

9.2.1. Response Function

As described in Section 3, there are two sets of coupled equations of motion for the floater: one consisting of roll, sway and yaw and one with surge, pitch and heave. This coupling is also visible in the obtained responses as shown in Figure 27: for a sinusoidal fluctuation in u the response in surge, heave and pitch is higher compared to a fluctuation in v (the blue line is above the red line). However, for the response in sway and yaw it is the other way around, with a larger response to the fluctuations in v (the red line is above the blue line). The response in roll direction is very similar for both directions.

As one can see in Figure 27c and Figure 27d there is a clear peak in response at the natural frequency in heave and in roll direction. For the other degrees of freedom, an increased response at the natural frequency is less pronounced. For example in sway direction (Figure 27b), the obtained response at the natural frequency is only slightly higher compared to the response at lower frequencies. However, when increasing the frequency above the natural frequency, the response in sway direction decreases significantly. In other words, the response in sway direction shows the low-pass filter as expected [50]. Remarkable is the fact that there is a sudden increase in sway response at $\omega = 0.23\ \mathrm{s}^{-1}$, which is the natural frequency for roll and visualizes the coupled equations of motion in sway and roll direction. Also in yaw direction such an increase at $\omega = 0.23\ \mathrm{s}^{-1}$ is visible for fluctuations in v, again at the natural frequency for motions in roll direction. The response in yaw-direction shows again a clear low-pass filter, which was also stated by Wise et al. [50]. There is no increase in response in roll direction at the natural frequencies for sway or yaw and therefore it seems that the motion in roll direction is dominant in the first set of coupled equations of motion.

Also in the second set of coupled equations of motion (for surge, pitch and heave) there is an interaction visible: there is a large increase at its natural frequency in heave direction for fluctuations in both u and v. There is also a slightly increase in response at the natural frequency in pitch direction, at $\omega = 0.23\ \mathrm{s}^{-1}$. Similarly to the behavior in sway direction, there is a clear low-pass filter visible in the response in surge direction, with an increase in response at $\omega = 0.23\ \mathrm{s}^{-1}$ for a fluctuation in u, which is again the natural frequency of pitch. Also in pitch direction, the low-pass filter is clearly visible. Because an increase in response at the natural frequency of pitch is visible in motions in both surge and heave direction, pitch seems to dominate this set of coupled equations.

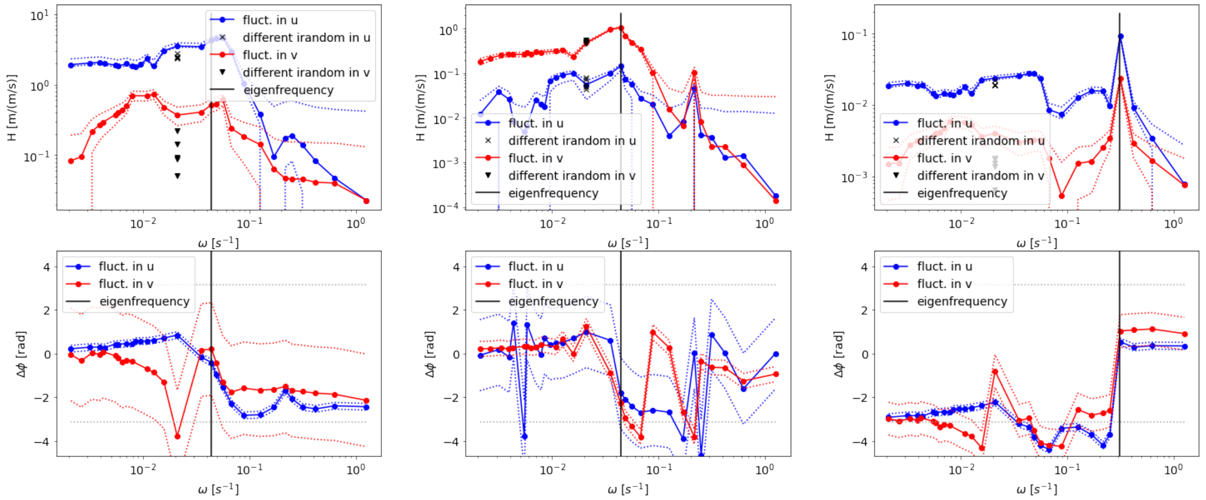

(a) Surge

(b) Sway

(c) Heave

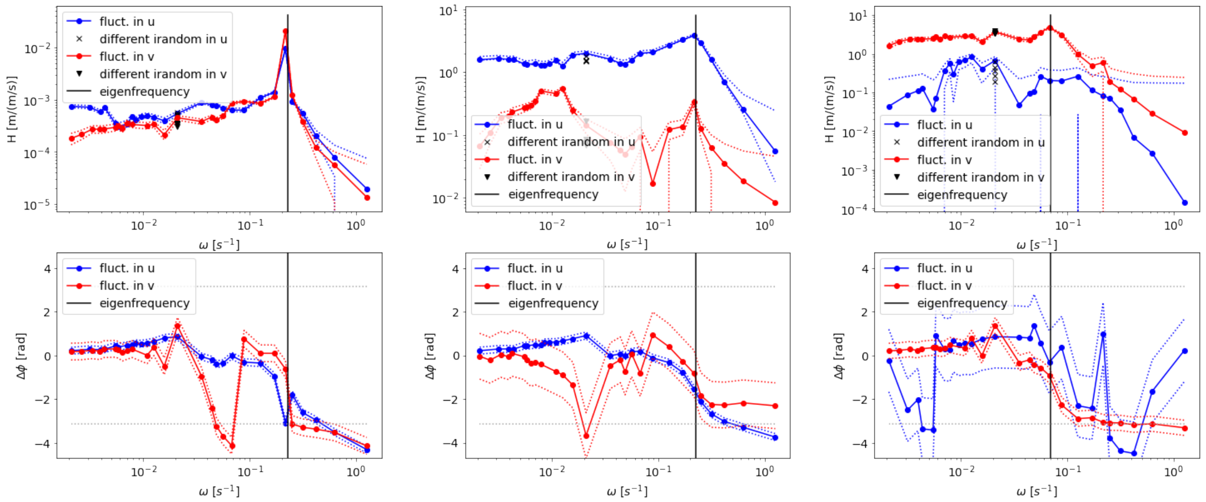

(d) Roll

(e) Pitch

(f) Yaw

Figure 27: The response function H (on a log-log scale) and the phase difference $\Delta\phi$ (on a semi-log scale in x-direction) plotted against the frequency ω for the six degrees of freedom. The blue lines represent a fluctuation in u, the red lines a fluctuation in v and the black vertical line the natural frequency for the degree of freedom. The black crosses and triangles denote the results for different random initialisation in respectively u and v. The standard deviation in these values is used to plot the error bars, denoted with the blue and red dashed lines.

9.2.2. Phase Difference

An interpretation of the obtained phase difference is a bit less clear compared to the responses in amplitude because there are much more outliers and big jumps. Note that a sine-function is periodic with 2π and therefore 2π can be added or subtracted from the phase difference without changing the obtained fitted sine. In this research, it is chosen to force the phase difference between $-\pi$ and $+\pi$, indicated with the grey dashed horizontal lines in Figure 27. However, sometimes the graphs are more easily to read when the phase difference is plotted slightly below $-\pi$ or slightly above $+\pi$, to prevent extreme jumps in the plotted graphs.

In surge direction, one can clearly see that the motions are aligned to the input profile for low frequencies and that the phase difference between the input velocity and the platform motions is increasing for higher frequencies. Especially for fluctuation in u this shape is nicely visible. At its natural frequency, the phase difference equals zero, meaning the input velocity and the output motion in surge direction are aligned again. Above this natural frequency, the phase difference is getting larger and larger, except at the natural frequency of pitch, showing the interaction between these degrees of freedom. For the fluctuation in v, the same behavior is obtained, except for the increase at the natural frequency of pitch and with one larger outlier at $\omega = 0.021 \text{ s}^{-1}$. A similar behavior is obtained for the phase differences in the other degrees of freedom, except for the one in heave direction: for low frequencies the motions are exactly out of phase (a phase difference of $-\pi$). At the natural frequency, this phase difference suddenly approaches zero and it then stays at zero when increasing the frequency. This opposite behavior makes sense: the more the platform moves in surge or sway direction, the more negative is the motion in heave direction due to the tension in the mooring lines. Therefore, the sine-function need to change sign. The fitted amplitude is forced to be positive and thus a phase difference of $\pm\pi$ is required to flip the sine function: $\sin(x \pm \pi) = -\sin(x)$.

9.3. Error Analysis

In this subsection, an error analysis is presented to validate the accuracy of the obtained results. Two methods are used: one considering uncertainties from uncertainty analysis and one considering different values for a random initialisation.

9.3.1. Uncertainty Analysis

The optimal values for A, t_0 and C are obtained using the `scipy.optimize.curve_fit()` function in Python, including the estimated variances σ^2 of these fitting parameters [74]. Using the uncertainty analysis as given in [75], the following equations can be used to calculate the uncertainties in the response (δH) and in the phase difference ($\delta(\Delta\phi)$):

$$\begin{aligned} \delta(H) &= H\sqrt{\left(\frac{\sigma_{A_\text{out}}}{A_\text{out}}\right)^2 + \left(\frac{\sigma_{A_\text{in}}}{A_\text{in}}\right)^2} \\ \delta(\Delta\phi) &= \sqrt{\sigma^2_{\phi_{in}} + \sigma^2_{\phi_{out}}} \end{aligned} \tag{30}$$

The obtained response function and phase difference for the surge direction including uncertainty is plotted in Figure 28. As one can see, the obtained uncertainties are small, meaning that the sine is fitted with high accuracy. Note that in the upper graph containing the response function H the y-axis is plotted on a logarithmic scale. Therefore, the uncertainties seem to be larger for smaller responses, while the relative uncertainty does not necessarily have to be larger compared to frequencies with higher responses. In the second and third column of Table 10 one can find the response for a period of 300 seconds and its uncertainty determined according to Equation 30 for a fluctuation in respectively u and v. As one can see, the obtained uncertainties are small compared to the responses.

9.3.2. Random Initialisation

Another method to validate the obtained results is by repeating a certain simulation with a different random initialisation. As described in Section 5.1, one can specify a certain `irandom` in the input profile, changing the random initialization. For a gust period of 300 s, the simulation is repeated for different values of `irandom`, indicated with the black crosses and

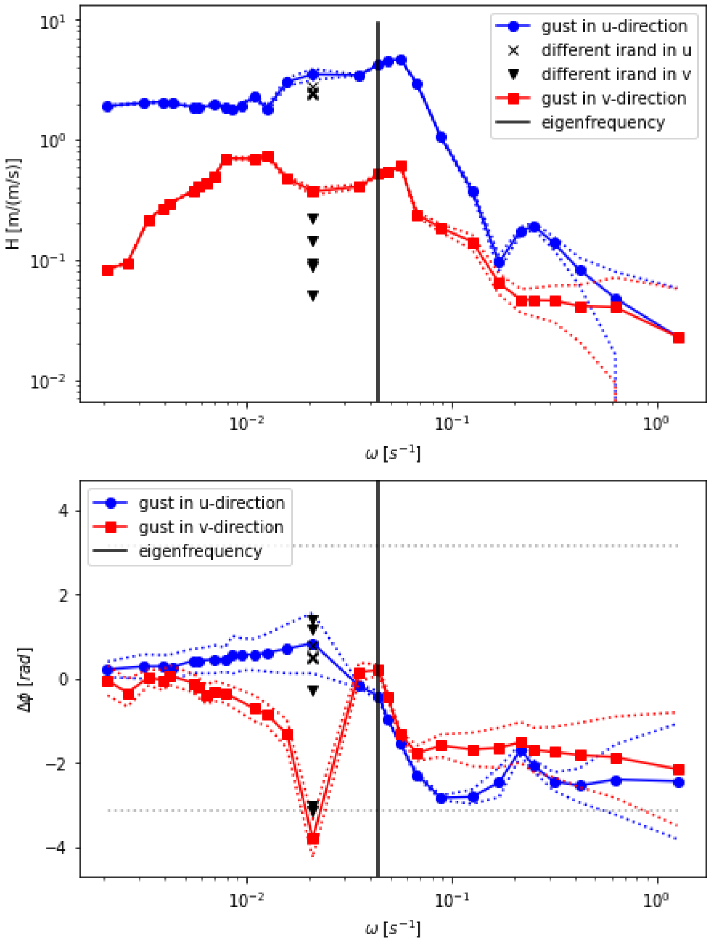

Figure 28: The response function H and phase difference $\Delta\phi$ plotted against the frequency ω for surge motions including uncertainty calculated using Equation 30.

triangles in Figure 28. As one can see, the responses obtained with these simulations do not fall between the uncertainty range from the analysis given in Equation 30. Therefore, it is chosen to use the error bars obtained from the random initialisation rather than using Equation 30.

In the fourth and fifth column in Table 10 the average value of the obtained responses for six different random initialisations and a gust period of 300 seconds is given, as well as the standard deviation in this value. Using this error analysis, one can determine the error bars as shown with the dashed lines in Figure 27. The upper error bar is obtained by adding the obtained standard deviation to the the response graph and the lower error by subtracting this standard deviation. This approach assumes that the magnitude of the uncertainty does not change for different frequencies. The same procedure can be used to determine the error bars in the phase difference.

As becomes clear from Table 10, the standard deviation for the obtained responses for a fluctuation in u is in general not too large, with percentages in between 10% (heave) and 20% (sway) of the average value. Except for the motions in yaw direction, in which the standard deviation equals 40% of the averaged value. When looking at the platform motions, one can understand that the standard deviation is largest in yaw direction since the motions are very chaotic in nature.

For fluctuations in v, there is a much larger difference in the obtained responses under different initialisations. In surge and in heave direction the standard deviations equals respectively 69% and 58% from the average values, while those in sway and yaw direction are much smaller with their 6% and 7%. Therefore, one can conclude that there is a much larger uncertainty in the obtained motions for fluctuations in v compared to fluctuations in u: the instability of the platform is larger for wind fluctuations in v than for those in u.

The visualisation in Figure 27 shows a much larger error bar in phase difference for fluctuations in u than for fluctuations in v. The opposite is true for the phase difference in surge and pitch where the error bars are larger for fluctuations in v.

The approach to determine the error bars using standard deviations assumes a normal distribution in motions. It is recommended to perform a more detailed error analysis in further research. One should also validate the assumption that the error bar does not change with frequency.

DOF	**response fluct. in** u **uncertainties from** (30)	**response fluct. in** v **uncertainties from** (30)	**average response fluct. in** u **std. from** `irandom`	**average response fluct. in** v **std. from** `irandom`
surge	3.51 ± 0.37	0.37 ± 0.02	2.68 ± 0.40	0.16 ± 0.11
sway	$(5.5 \pm 0.6) \cdot 10^{-2}$	0.48 ± 0.03	$(5.9 \pm 1.2) \cdot 10^{-2}$	0.50 ± 0.03
heave	$(2.4 \pm 0.3) \cdot 10^{-2}$	$(4.1 \pm 0.8) \cdot 10^{-3}$	$(2.0 \pm 0.2) \cdot 10^{-2}$	$(1.9 \pm 1.1 \cdot 10^{-3}$
roll	$(5.4 \pm 2.3) \cdot 10^{-4}$	$(4.5 \pm 2.3) \cdot 10^{-4}$	$(5.0 \pm 0.6) \cdot 10^{-4}$	$(3.6 \pm 0.4) \cdot 10^{-4}$
pitch	2.00 ± 0.21	0.14 ± 0.01	1.65 ± 0.19	0.10 ± 0.04
yaw	0.67 ± 0.07	3.69 ± 0.20	0.43 ± 0.17	3.55 ± 0.24

Table 10: The obtained responses in [m/(m/s)] for a sinusoidal fluctuation in u and in v for all degrees of freedom obtained for a gust period of $T = 300$ seconds, including uncertainties as determined using Equation 30 (column 2 and 3) or the standard deviation in the results for different random initialisation (column 4 and 5).

9.4. Conclusion

In conclusion, the response graphs clearly show low-pass filters in all degrees of freedom and for both the fluctuation in u and in v. At the natural frequencies, there are increased responses compared to surrounding frequencies, especially in heave and in roll direction. Due to the increase in response also at other natural frequencies, the coupling of motions is confirmed. The different results for a gust in u and in v greatly show the division of the degrees of freedom over the two sets of coupled equations of motion.

An error analysis is performed on the obtained response function and phase difference. The standard deviation provided by the fitting tool in Python is small. However, the results when running the same simulation for a gust period of 300 seconds with another random initialisation do not fall within the obtained uncertainty range. Therefore, the standard deviation is determined for the results for six different random initialisations and this value is used to determine the error bars. It is recommended to do a more elaborate uncertainty analysis, which could help to put some of the "jumpy" results into perspective. One can for example run more simulations with other random initialisations or study the dependence of the error bar on frequency.

10. Turbine's Behavior under Different Atmospheric Stability Regimes

Since atmospheric stability have a substantial impact on the wind turbine efficiency in terms of motions, wakes and power production (see Section 2), it is crucial to take atmospheric stability into account when designing wind turbines.

In this section, the influence of atmospheric stability on the power generation and motions for a floating wind turbine is evaluated. Some background information about atmospheric stability is given in Section 2.

10.1. Changing Surface Heat Flux

The simplest way to introduce a stable, neutral and unstable boundary layer in ASPIRE is by changing the surface heat flux. This surface heat flux is given by $\overline{w'\theta'_v}$ as introduced in Section 2.1.2 in Equation 3. A negative value for this surface heat flux denotes a stable atmosphere ($L > 0$), a positive value denotes an unstable atmosphere ($L < 0$) and zero surface heat flux denotes the neutral atmosphere ($L \to \infty$). The used parameters to study the influence of atmospheric stability on the floater are given in Table 11.

parameter	**specification**
wind turbine	IEA Wind 15MW Offshore Reference Wind Turbine [4]
floater type	UMaine VolturnUS-S Semi-Submersible floater [1]
turbine (x, y)-position	384 m × 512 m
rotor speed	6.31 rpm
simulation time initialisation	30000 s
domain size initialisation	10240 m × 1024 m × 512 m
resolution initialisation	16 m × 16 m × 16 m
simulation time (pre)cursor	3600 s
domain size (pre)cursor	10240 m × 1024 m × 512 m
resolution (pre)cursor	16 m × 16 m × 16 m
time step	$\Delta t = 0.1$ s
averaging time cursor	1800 s
input velocity	$u_i = 8$ m/s, $v_i = 0$ m/s at all heights
tendency of velocity u	stable conditions: $2.3 \cdot 10^{-4}$ m/s^2 at all heights neutral conditions: $3.2 \cdot 10^{-4}$ m/s^2 at all heights unstable conditions: $4.8 \cdot 10^{-4}$ m/s^2 at all heights
standard deviation in specific humidity	$2.5 \cdot 10^{-5}$ g/kg
standard deviation in specific temperature	0.1 J/(kgK)
Coriolis force	disabled
moisture effects	enabled
surface roughness	0.05 m
surface heat flux	stable conditions: -0.005 Km/s neutral conditions: 0.0 Km/s unstable conditions: +0.048 Km/s
water type	still water

Table 11: The input parameters used to study the behavior of the floating turbine under different atmospheric stability regimes by changing the surface heat flux.

Ideally one would have three different scenarios with identical velocity at the rotor because the wind speed is greatly influencing the turbines behavior in terms of power production and motions (see Section 8). Therefore, each simulation has a different value for the tendency of velocity in x-direction. The surface roughness is equal for all stability regimes. It is chosen to set the value for the surface roughness to $z_0 = 0.05$ m, although this value is not representative for values offshore. This value is needed to increase the background turbulence in the simulations, otherwise the wake will not recover under neutral conditions where the surface heat flux equals zero due to a lack of mixing of air. Under real weather situations there is more background turbulence and thus the wake will also recover in neutral situations.

All simulations are initialized with an input velocity of 8 m/s in x-direction, but due to influences from the surface heat flux (causing the different stability conditions), the final velocity profiles after running the initialization simulation is different for each stability. A visualisation of these profiles is shown in Figure 29. The hub-height for the chosen wind turbine is denoted with the horizontal dashed line. As one can see, the velocity at hub height is 8 m/s in all regimes, although the profiles look very different. This is achieved by adapting the tendency of u for each surface heat flux separately.

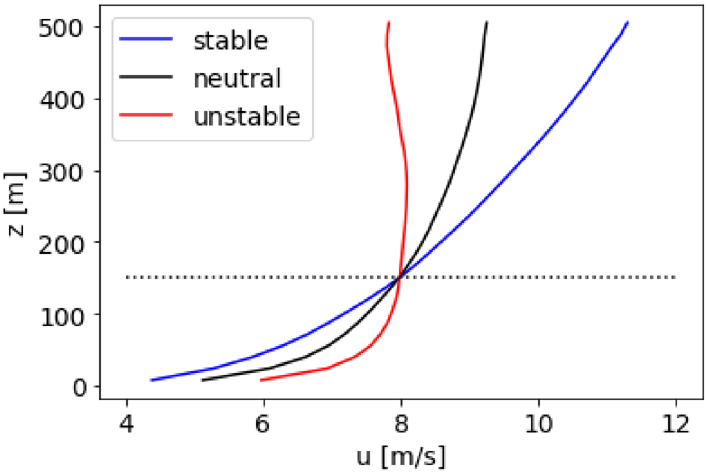

Figure 29: The input velocity profile to study the influence of atmospheric stability on the floater, using the simple input profiles with only changing surface heat flux. The dashed horizontal line denotes the hub height for the chosen wind turbine.

10.2. Results and Discussion

A summarize of the obtained results for the different atmospheric stability conditions are given in Table 12. In the next subsections, these results will be discussed in detail.

	description	stable regime	neutral regime	unstable regime
u	wind velocity at hub height in x	8.00 ± 0.00 m/s	8.00 ± 0.01 m/s	7.98 ± 0.01 m/s
v	wind velocity at hub height in y	-0.012 ± 0.001 m/s	-0.026 ± 0.004 m/s	0.029 ± 0.004 m/s
w	wind velocity at hub height in z	$(0.6 \pm 1.4) \cdot 10^{-10}$ m/s	$(-0.8 \pm 2.3) \cdot 10^{-10}$ m/s	$(1.4 \pm 2.7) \cdot 10^{-10}$ m/s
P	rotor power	3.6 ± 0.6 MW	3.8 ± 0.7 MW	2.9 ± 0.7 MW
c_P	rotor power coefficient	0.42 ± 0.03	0.42 ± 0.03	0.39 ± 0.04
d_{sg}	displacement in surge direction	13.9 ± 1.4 m	14.1 ± 1.4 m	13.3 ± 1.5 m
d_{sw}	displacement in sway direction	-0.03 ± 0.35 m	-0.04 ± 0.41 m	-0.07 ± 0.47 m
d_{hv}	displacement in heave direction	-0.42 ± 0.06 m	-0.42 ± 0.06 m	-0.41 ± 0.06 m
α_{roll}	rotation in roll direction	$0.16 \pm 0.12°$	$0.15 \pm 0.13°$	$0.10 \pm 0.14°$
α_{pt}	rotation in pitch direction	$2.2 \pm 0.2°$	$2.2 \pm 0.2°$	$1.9 \pm 0.3°$
α_{yaw}	rotation in yaw direction	$0.61 \pm 0.58°$	$0.21 \pm 0.67°$	$-0.20 \pm 0.95°$

Table 12: Different variables for the three different stability conditions, averaged over the last 1800 seconds of the simulation in the steady regime including standard deviation.

10.2.1. Velocity Profiles

The obtained velocities at hub height are averaged over the last 1800 seconds of the simulation. To exclude the influence of the difference in free-stream velocities, the velocity deficit is determined for all stability regimes at all locations in the domain using the following expression:

$$\frac{\Delta u_{(x,y)}}{u_\infty} = \frac{u_\infty - u_{(x,y)}}{u_\infty} \tag{31}$$

in which $u_{(x,y)}$ denotes the obtained velocity at a certain position (x, y) and u_∞ the free-stream velocity. It is chosen to use the velocity at hub-height from the input profile as u_∞, being 8 m/s for all stability regimes. The velocity deficit is determined for every location in the domain, resulting in the contour plots as shown in Figure 30. From this figure, it becomes clear that the wake recovery is fastest under unstable conditions and slowest under stable conditions. This is due to the difference in turbulence intensity: the higher the turbulence intensity (decreasing stability), the larger the mixing and the faster the wake recovers [8].

It takes $23D$ under stable, $15D$ under neutral and $7D$ under unstable conditions for the wake of the floating turbine to recover. Research from Abkar et al. used an actuator disk model with rotation for a static wind turbine to study the wake length under different atmospheric stability regimes [41]. The values for the kinematic shear stress, the streamwise velocity profile and the potential temperature greatly correspond to the values used in this research. Abkar et al. obtained a wake length of $20D$ under stable, $12D$ under neutral and $8D$ under unstable conditions [41]. This indicates that the differences between a modelled floating wind turbine and a modelled static wind turbine are only small in terms of wake length when comparing different atmospheric stability conditions.

Looking at Figure 30, one can see that the wake under unstable conditions is not following the main wind direction, but it is a bit inclined. This is due to the eddies in the system: under unstable conditions the eddies are growing and growing until they touch the domain boundaries, resulting in a left- or right-handed circulation through the domain. Therefore, although the average velocity in y-direction equals zero, turbulence starts to organize over time. A visualisation of this circulation is shown in Figure 31. The upper figure shows the velocity v in the initialisation simulation after 1200 seconds and the lower figure after 30.000 seconds. As one can see, after 1200 seconds the areas of higher and lower velocities are divided

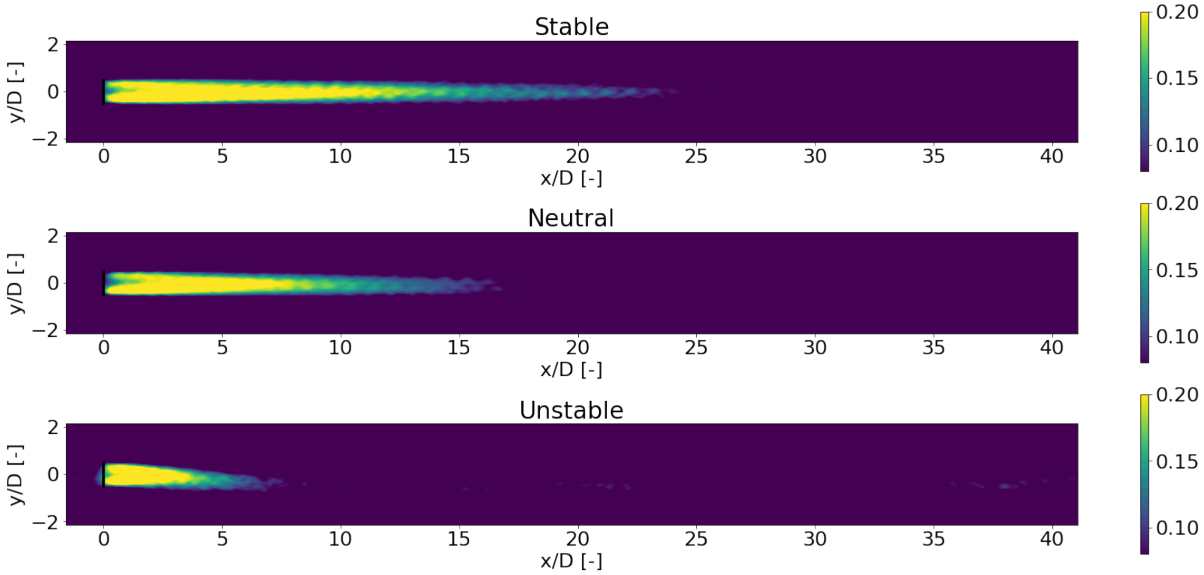

Figure 30: The time-averaged streamwise velocity deficit $\Delta u/u_\infty$ in the (x, y)-plane at turbine hub height for the three different stability regimes.

randomly throughout the domain. However, after 3600 seconds large eddies are developed, which cause the velocity to slightly increase in the lower part of the domain and decrease in the upper part of the domain, still with a zero average wind speed. The areas of higher velocities gather at the lower part of the domain and the areas of lower velocity in the upper part. This causes the wake under unstable conditions to incline to the lower part of the domain. Because the eddies are suppressed under stable conditions, they stop growing and the wake is following the main wind direction.

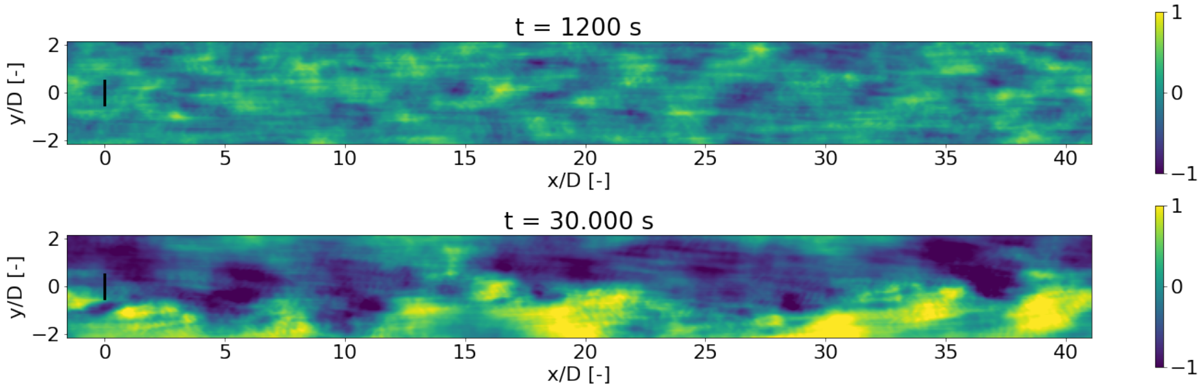

Figure 31: The development of the velocity in y-direction during initialization of the boundary layer under unstable conditions. The upper figure shows the velocity v after 1200 seconds and the lower figure after 30.000 seconds, visualizing the influence of large eddies in the domain.

In Figure 32 the cross sections in x-direction of the horizontal wind profiles are shown. The profiles are plotted 1D apart from each other and show the wake evaluation over space. Each profile is shifted with 0.5 in horizontal direction and thus the space in between the profiles at the x-axis corresponds to $\Delta u/u_\infty = 0.5$. Again one can see that the wake under unstable conditions recovers fastest. Besides, one can see that the wake propagation under unstable conditions is not following the main wind direction, but shows a small incline. The difference between stable and neutral conditions is less pronounced, although one can still see that the wake under neutral conditions recovers a bit faster compared to stable conditions.

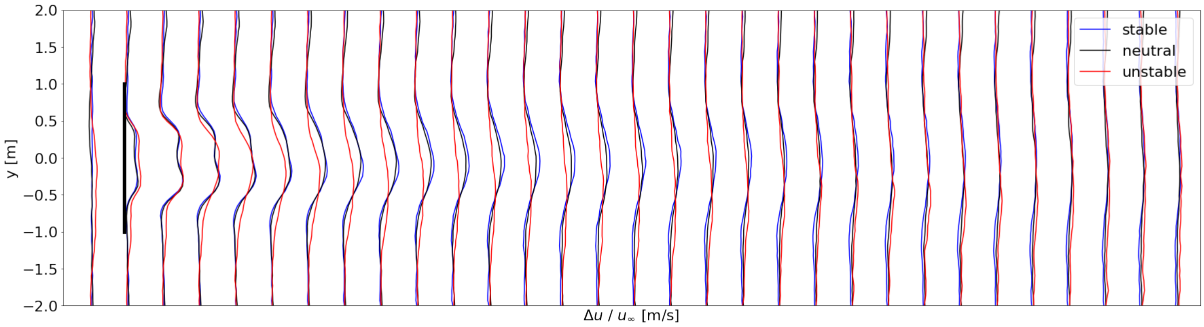

Figure 32: The time-averaged velocity deficit behind the rotor, plotted 1D apart under stable, neutral and unstable conditions. The horizontal space in between each profile at the x-axis corresponds to $\Delta u/u_\infty = 0.5$.

10.2.2. Turbulence Intensity

The turbulence intensities for the three different stability regimes are shown in Figure 33. The point of maximum turbulence intensity can be found at $4.7D$ behind the rotor under stable, $4.5D$ under neutral and only $1.7D$ under unstable conditions. In other words, the point of maximum turbulence intensity moves further downwind as stability increases. This was also observed by Abkar et al. [41]. Again, the differences between stable and neutral conditions is less pronounced compared to the unstable case.

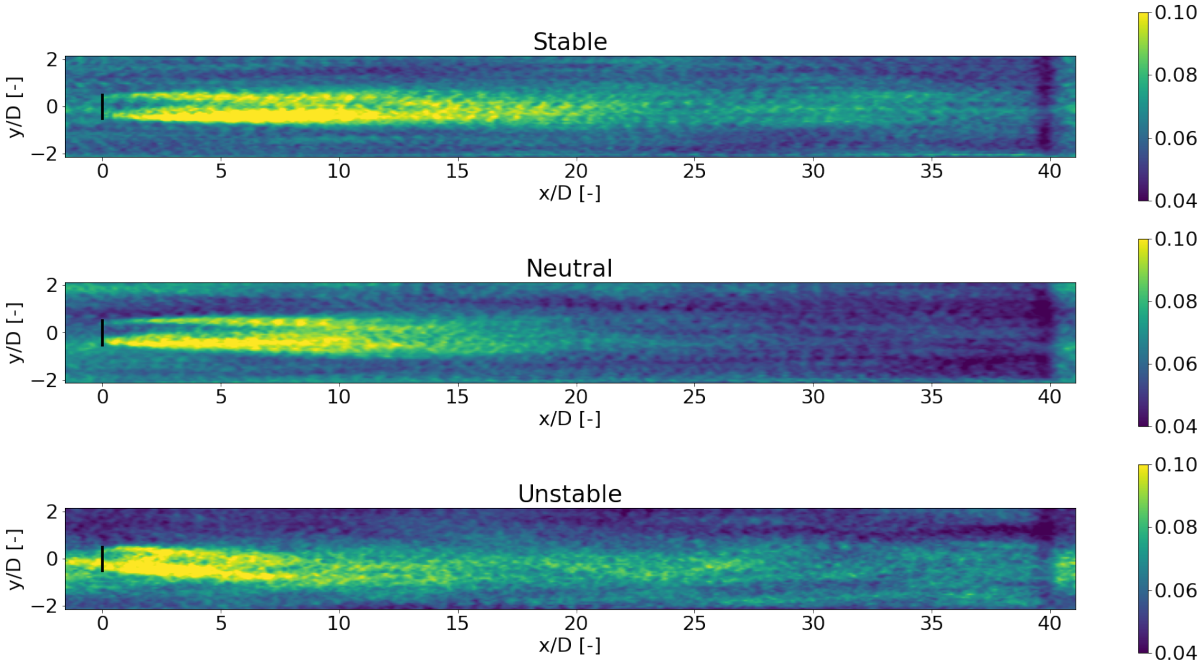

Figure 33: The time-averaged turbulence intensity TI (m^2/s^2) *plotted in the* (x, y)*-plane for the three different stability regimes.*

10.2.3. Power Generation

The power output of a wind turbine is greatly influenced by the inflow velocity. Because the difference in velocity at hub height is very small in the used set-up, one would expect a small difference in power output. However, it varies between 2.9 MW under unstable, to 3.6 MW under stable, to 3.8 MW under neutral conditions. The standard deviation is similar in all cases in absolute value, meaning that it is relatively largest under unstable conditions. The reduction in power for unstable conditions compared to stable conditions equals 19%. This is in line with the results from Wharton et al., where a reduction of 20% was found for an isolated turbine under different atmospheric conditions [44]. Due to the higher turbulence intensity in the unstable regime, the power fluctuations are larger compared to stable conditions, which is in line with the study of Liu et al. [7].

10.2.4. Platform Motions

In general, the platform motions do not vary that much for the three different stability regimes, as shown in Table 12. From Section 8 and Section 9 it becomes clear that platform motions are greatly influenced by the inflow velocities. As one can see in Figure 29, the velocity below hub height is lower under stable conditions and higher under unstable conditions. Because the platform and tower experience a larger velocity under unstable conditions, one would expect a larger response in platform motions compared to stable conditions. However, looking at the results presented in Table 12, this is not the case and the differences between the obtained motions is quite small for the different regimes. The variations in input velocities are not large enough to cause a significant difference in platform motions for the three stability regimes. Therefore, according to these results, the atmospheric stability is not influencing the platform motions significantly.

10.3. Conclusion

By changing the surface heat flux from positive to negative values, the atmospheric stability is changed from unstable to stable conditions. Looking at the velocity deficit, the largest wake length is obtained under stable conditions ($23D$) and the smallest under unstable conditions ($7D$). This is due to the increase in turbulence intensity under unstable conditions, enhancing the mixing of air and thus increasing the wake recovery. As stability increases, the point of maximum turbulence intensity is moving further downwind (from $4.7D$ under stable to $1.7D$ under unstable conditions). The atmospheric stability does not influence the platform motions significantly.

11. Bottom Fixed versus Floating Turbines

In this section, a comparison is made between a bottom-fixed wind turbine and the floating wind turbine in terms of velocity profile, power production and turbulent kinetic energy for a uniform inflow velocity profile.

The used bottom-fixed wind turbine is the IEA-15-240-RWT-Monopile [4]. Such a monopile construction is one of the most common foundations in offshore wind construction, due to its easy installation in shallow waters (up to 50 m water depth [19]). It consists of a steel tube, driven into the seabed by hammering [76] and therefore it cannot move in the introduced six degrees of freedom for a floater. The wind turbine on the Monopile is identical to the one on the floating platform. Therefore, the parameters for the turbine as given in Table 1 are unchanged for the Monopile. However, the specifications for the platform do change and these are shown in Table 13.

parameter	**specification**
transition piece height	15 m
monopile embedment depth	45 m
monopile base diameter	10 m
designed water depth	30 m
monopile mass	1318 t

Table 13: Some general parameters for the Monopile construction [4].

This Monopile is compared to the UMaine VolturnUS S semi-submersible floater, as already introduced in the previous chapters. The library for both the Monopile and the UMaine VolturnUS S Semi-Submersible are downloaded from the GitHub [77].

Identical simulations are run, the only differences between the two simulations are in the specifications of the wind turbine itself. For both cases, the structural dynamics are determined using the ElastoDyn module. In this module, all degrees of freedom are disabled, except for the platform motions. Aerodynamic and hydrodynamic loads are computed using AeroDyn and HydroDyn. In case of the monopile construction, SubDyn is enabled to compute substructural dynamics. For the floating turbine, the mooring system is included by enabling MoorDyn. An input velocity profile of 10 m/s is used in this simulation, the blade pitch is forced to 0° and the rotor speed is fixed at 7.55 rpm, which is in line with the definition of the chosen wind turbine [4]. The other parameters are given in Table 14.

Note that the used time step for the Monopile in OpenFAST differs from the time steps in previous sections. This is due to the enabling of the substructural dynamics, which needs a smaller time step because of their lower structural time-scales (see Equation 23).

parameter	specification
wind turbine	IEA Wind 15MW Offshore Reference Wind Turbine [4]
type	floating: UMaine VolturnUS-S Semi-Submersible floater [1] bottom-fixed: IEA-15-240-RWT-Monopile [4]
turbine (x, y)-position	512 m × 512 m
simulation time initialisation	30000 s
domain size initialisation	10240 m × 1024 m × 512 m
resolution initialisation	16 m × 16 m × 16 m
simulation time (pre)cursor	3600 s
domain size (pre)cursor	10240 m × 1024 m × 512 m
resolution (pre)cursor	16 m × 16 m × 16 m
averaging time cursor	1800 s
timestep GRASP	$\Delta t = 0.1$ s
timestep OpenFAST	floating: $\Delta t = 0.1$ s fixed: $\Delta t = 0.005$ s
input velocity	$u_i = 10$ m/s, $v = 0$ m/s at all heights
tendency of velocity u	$2 \cdot 10^{-4}$ m/s^2 at all heights
standard deviation in specific humidity	$2.5 \cdot 10^{-5}$ g/kg
standard deviation in specific temperature	0.1 J/(kgK)
Coriolis force	disabled
moisture effects	enabled
surface roughness	$z_0 = 0.0001$ m
water type	still water

Table 14: The parameters used to study the difference between a floating and a bottom-fixed wind turbine under a uniform velocity input profile.

11.1. Results and Discussion

11.1.1. Velocity Profile

In Figure 34 one can find the obtained time-averaged velocity deficit at hub height determined using Equation 31 for the Monopile (fixed turbine) and the UMaine semi-submersible (floating turbine) plotted in the (x, y)-plane. They are averaged over the last 1800 seconds of the simulation. As one can see, the profiles are very similar in both shape and magnitude.

Another visualisation of the velocity deficit is shown in Figure 35 in which a time-averaged cross-section of the velocity deficit in y-direction is plotted each $1D$ behind the rotor for both the floating and the fixed turbine. The plotted graphs are measured $1D$ apart from each other and plotted with a horizontal shift of 0.7. And indeed, there is no difference in the velocity deficit for a fixed or a floating turbine under the used inflow profile. Other research studying the difference in mean velocity profile for fixed and floating wind turbines obtained similar results, showing that the mean velocity profile is unchanged for the two cases [78, 79].

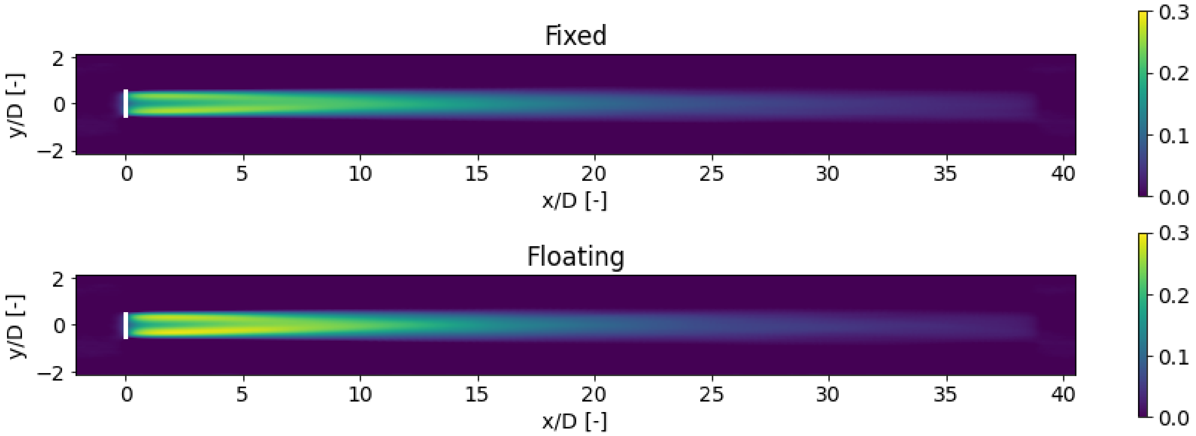

Figure 34: The time-averaged streamwise velocity deficit $\Delta u/u_\infty$ *in the* (x,y)*-plane at turbine hub height for a floating ([1]) and a bottom-fixed ([4]) wind turbine.*

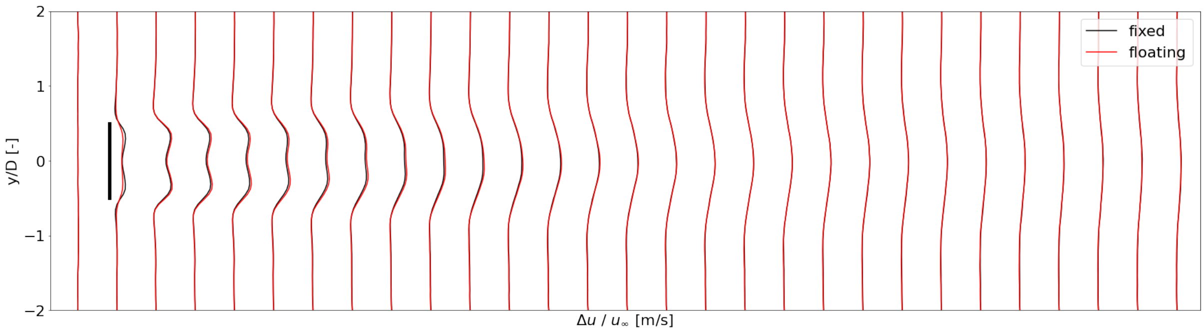

Figure 35: The time-averaged velocity deficit at hub height plotted $1D$ *apart for a floating and a bottom-fixed wind turbine. The horizontal space in between each profile at the x-axis corresponds to* $\Delta u/u_\infty = 0.7$*.*

11.1.2. Turbulent Kinetic Energy

The time-averaged turbulent kinetic energy k at hub height is plotted in the (x,y)-plane for both turbines in Figure 36. The profiles look similar, although they clearly show some difference in value around $10D$ behind the rotor. To visualise the difference in more detail, the cross-sections in x-direction are shown in Figure 37, in which the profiles (measured $1D$ apart from each other) are plotted next to each other with a horizontal spacing of 0.3 $\mathrm{m}^2/\mathrm{s}^2$. As one can see, the difference in turbulent kinetic energy behind the rotor in the near wake are small: until $3D$ the profiles are very similar. However, when moving further downwind, the turbulent kinetic energy gets a bit higher for the floating turbine compared to the fixed one. For example at $10D$, the maximum turbulent kinetic energy equals 0.43 $\mathrm{m}^2/\mathrm{s}^2$ for the Monopile and 0.50 $\mathrm{m}^2/\mathrm{s}^2$ for the UMaine Volturnus S Semi-Submersible, which is almost 1.2 times larger. When moving to $29D$ or even further downwind, the profiles are similar again and there is no difference in turbulent kinetic energy between the two cases.

Typical spacing for an offshore wind farm is $8D - 12D$ in the prevailing wind direction and $3D - 5D$ in the cross-wind direction [80]. In this region, the turbulent kinetic energy is higher for floating turbines, resulting in higher induced loads on the downwind turbines. The obtained results are not in line with research performed by Schliffke et al. ([79]), in which the opposite was obtained: in the far wake, the turbulence intensity was lower for floating turbines compared to bottom-fixed wind turbines.

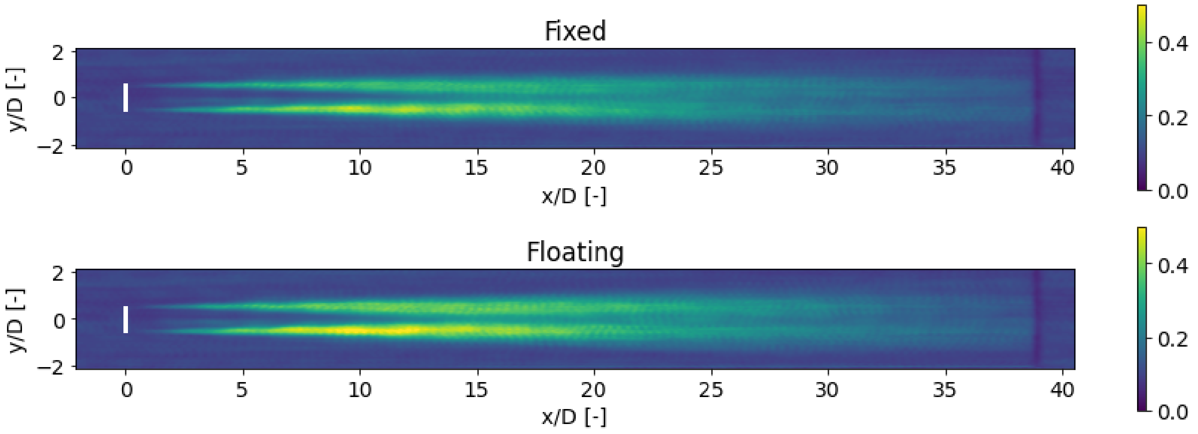

Figure 36: The time-averaged turbulence intensity k (m^2/s^2) *at turbine hub height in the* (x, y)-*plane for a floating ([1]) and a bottom-fixed ([4]) wind turbine.*

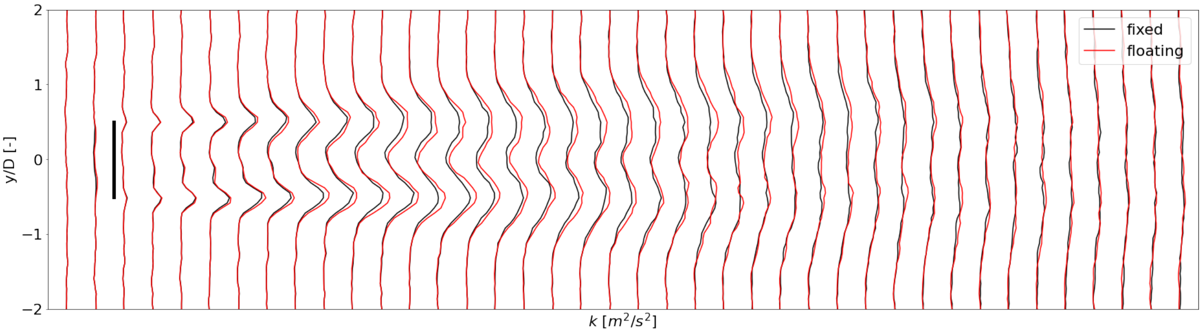

Figure 37: The time-averaged cross-sections of the turbulent kinetic energy k at hub height, plotted $1D$ *apart for a floating and a bottom-fixed wind turbine. The horizontal space in between each profile at the x-axis corresponds to* $k = 0.3\ m^2 s^{-2}$.

11.1.3. Power Generation

The obtained power outputs plotted against time for the bottom-fixed and the floating construction are shown in Figure 38. As one can see, the fluctations in power generation are much larger for the floating turbine compared to the fixed turbine: the time-averaged power over the last 1800 seconds of the simulation equals 8.47 ± 1.46 MW for the UMaine Volturnus S Semi-Submersible and 9.09 ± 0.75 MW for the Monopile. The increase in power fluctuations is most likely due to the increased turbulence intensity for the floating turbine. The obtained outputs are smaller than expected according to the definition of the chosen wind turbine: for a wind speed of 10 m/s, a blade pitch of 0° and a rotor speed of 7.55 rpm the turbine is designed to generate 13 MW [4]. The rotor speed and the blade pitch are fixed to these values, so this cannot cause the difference. It is unclear why the obtained results are 31% smaller than expected. To find the cause of this difference, it is recommended to validate the simulation set-up again.

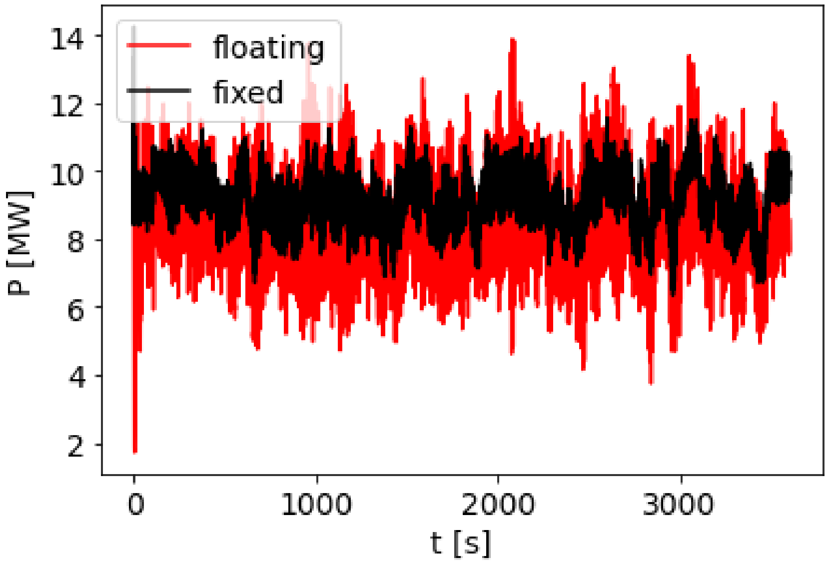

Figure 38: The obtained power outputs plotted against time for the bottom-fixed and the floating wind turbine.

11.2. Conclusion

The obtained velocity profiles are very similar for the Monopile (bottom-fixed turbine) and the UMaine VolturnUS S Semi-Submersible (floating turbine). This is in line with the observations of Schliffke et al. and Fontanella et al. [78, 79]. The turbulent kinetic energy is similar in the near wake (up to $3D$). When moving further downwind, the turbulent kinetic energy is higher for the floating turbine compared to the bottom-fixed turbine: at $10D$ it is almost 1.2 times larger. After $29D$ the turbulent kinetic energy is recovered to its original state and there are no differences between the bottom-fixed and the floating turbine. The obtained power output is smaller for the floating turbine, but with larger power fluctuations. This is most likely due to the increased turbulence intensity. However, the obtained values are 31% smaller than expected under the simulated situation according to the turbine's definition [4]. In this research, time did not permit to find out what causes the difference in power output. Therefore, it is recommended to check and validate the used set-up again. Besides, it would be interesting to run simulations under real weather conditions while enabling the control mechanisms in ServoDyn, to see what happens with the turbulent kinetic energy and the velocity profiles in more realistic scenarios.

12. Conclusion

The energy consumption is growing and growing over the past few years and in the meanwhile, all nations are united by the Paris Agreement to undertake ambitious efforts to limit global warming and combat climate change. Therefore, there is a strong need for more renewable energy sources. In addition to solar power, wind energy will be one of the key sources of additional renewable energy. Wind turbines can be placed both onshore and offshore. For water depths more than 50 m, floating platforms are the most effective ways to stabilize wind turbines offshore. In this research, the behavior in terms of platform motions, flow field and power production of the Umaine VolturnUS S semi-submersible floating platform designed for the IEA 15 MW reference turbine is studied using a coupling between ASPIRE and OpenFAST. ASPIRE is a software to solve LES-models, developed by the company Whiffle and is able to do very precise weather forecasting by providing a turbulence resolving numerical weather model. The coupling with OpenFAST allows to combine these weather conditions with wind turbine analysis. This coupling can reduce the costs of adapting wind energy inputs to the power grid because the energy producers would meet the expected supply threshold more often due to the more precise power forecasting.

After this coupling is established, a convergence study is performed, in which a proper time step and grid size are obtained for the simulations in this research. A time step of 0.1 seconds and a grid size of 16 m in all directions is used to capture both platform motions and flow field properties correctly. It is chosen to fix the rotor speed and blade pitch to proper values obtained from the turbine's definition [4]. The influence of waves from the Pierson-Moskowitz spectrum on the power output, platform motions and flow field are small and therefore the simulations are performed assuming still water.

Using these settings, the platform motions of the floater are studied under uniform inflow velocity profiles. In general, the displacements in all directions increase for higher velocities, for example the platform moves 22.8 m in surge direction for a streamwise wind speed of 15 m/s and only 13.5 m for a streamwise wind speed of 8 m/s. From the oscillatory motions in the responses, one can determine the natural frequencies in all degrees of freedom. In general, the obtained frequencies correspond to the frequencies obtained with the free-decay tests in [4], with absolute percentage errors in between 2% (heave) and 29% (surge).

To study the response of the platform for different frequencies, simulations were performed using a sinusoidal input profile with various periods in either u or v (respectively surge or sway direction). Fitting a sine-function with the specified period to both the input profile and the platform motions allowed to determine the response functions and the phase differences between the two. The responses in surge, pitch and heave direction are higher for fluctuations in u compared to v, whereas it is the other way around for the responses in sway and yaw. This can be explained with the equations of motion, which consist of two sets of coupled equations: one containing motions in surge, pitch and heave direction and one containing motions in roll, sway and yaw direction. As expected, the response at the natural frequency is higher than at other frequencies, especially in roll and in heave direction this increase in response is clearly visible. Remarkable is the fact that some motions also show an increased response at the natural frequency in another degree of freedom: for example there is a clear increase visible in sway direction at the natural frequency of roll. This again shows the coupling between the motions.

The influence of atmospheric stability on the floater is tested by changing the surface heat flux from negative (stable) to zero (neutral) to positive (unstable) values. To exclude influences of the different velocities at hub height, the velocity deficit is computed and compared. From this velocity deficit, it becomes clear that as stability increases, the wake length grows: a full wake recovery takes $23D$ under stable and only $7D$ under unstable conditions. This is due to the decreasing turbulence intensity for increasing stability, which also explains the larger power fluctuations in unstable conditions. Besides, as stability increases, the point of maximum turbulence intensity is moving further downwind: it is positioned at $4.7D$ behind the rotor under stable conditions and at $1.7D$ in the unstable regime.

Lastly, the differences in behavior between a floating and a bottom-fixed wind turbine are evaluated regarding the flow field and power production. For the chosen set-up there was no significant difference in obtained velocity flow field, which is in line with other research [78, 79]. The turbulent kinetic energy is almost 1.2 times higher for the floating turbine at $10D$ behind the rotor. In the near wake (up to $3D$) and far behind the rotor (from $29D$ and further) there are no differences in turbulent kinetic energy between the two cases. The obtained power output is smaller for the floating turbine with larger power fluctuations compared to the fixed turbine. It is recommended to run simulations using more realistic input profiles to see what happens with the results.

13. Discussion and Recommendations

This report contains different subjects and different research questions, which are dealt with in separate sections. In this section, a discussion about the obtained results are provided, as well as some recommendations for further research.

13.1. Convergence Study

A time step of 0.1 seconds and a grid size of 16 m was chosen as a balance between accuracy and computational costs. It would be interesting to analyse the equations of motion in more detail. The largest natural frequency in the degrees of freedom equals 0.049 Hz (heave) [4], theoretically resulting in a maximum allowed time step of $1/(10f_{max}) = 2.0$ s [11]. The maximum allowed time step in the simulations in this research equals 0.1 s, indicating that there should be some coupled frequency in the order of 1 Hz. It would be interesting to see whether one can indeed find this frequency by studying the equations of motion in more detail. Besides, one can search for other factors limiting the time step. Regarding the flow field, one could increase the time step to 0.4 seconds. However, this is not small enough to correctly capture the platform motions. After finding the limiting component for the time step, one can decide whether this can be disabled to decrease the computational costs by increasing the time step.

When changing the grid size, some interesting behavior is obtained in sway and yaw direction. It would be interesting to study the platform motions in more detail. In Figure 39 one can find the obtained platform motions for more resolutions. It seems that the shape is resolved differently on different grid sizes. Perhaps the turbine "fits" better on a certain coarse resolution than on a slightly higher one. It would be interesting to figure out what is going on with the motions in sway and yaw direction in more detail.

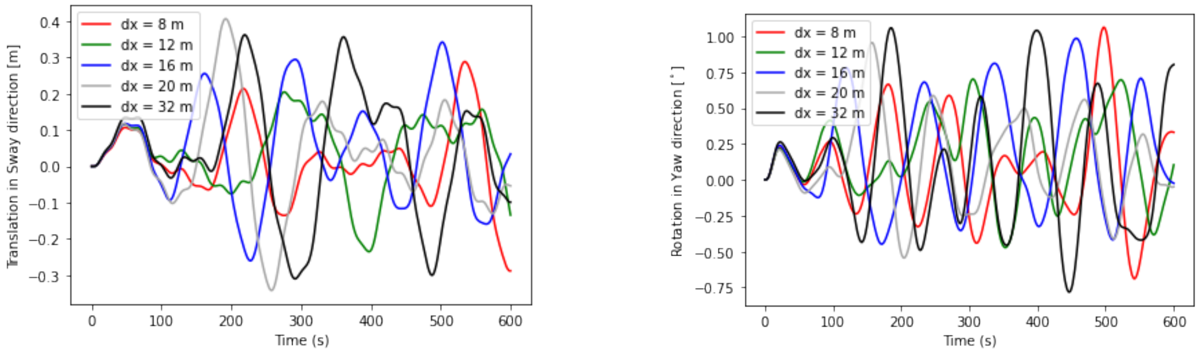

(a) Translation in sway direction

(b) Rotation in yaw direction

Figure 39: Platform motions in sway and in yaw direction plotted against time for different resolutions to visualise the difference in behavior.

13.2. Responses

Before a new wind farm is built, it is useful to study the prevailing frequencies in the wind data over the past few years at the chosen area and in the wake of the turbine. One can then determine the occurrence of each frequency and check the corresponding turbine's response. It would be interesting to study which conditions cause high responses. This information could help to improve the process of allocating wind farms: one can decide to find another location where the specific frequency is less pronounced, or to use another wind turbine with other natural frequencies. This would decrease the motions of the wind turbine and thus the fatigue.

13.3. Stability Conditions

The conditions in the North Sea are dominated by unstable and near-neutral conditions [28]. Comparing to other sides, where the atmosphere is dominated by stable conditions, the wake length at the North Sea is much shorter. This would imply that the spacing within a wind farm can be smaller and thus one can add more turbines to the same area, increasing the power production in that area. It would be interesting to run a whole year of real weather data for a wind farm at the North Sea and study the optimal spacing. Research from Svensson et al. showed a strong seasonality in the stability over the Baltic Sea with 80% stability in spring compared to 10% in winter [81]. Due to the large differences in wake length under the different stability regimes, it is complex to find a proper spacing within a wind farm. It would be interesting to run simulations including a whole wind farm with real wind data to find the optimal spacing, the fatigue on downwind turbines and the power production.

13.4. Bottom-Fixed versus Floating

In further research, it is recommended to check the used set-up again to compare the behavior of bottom-fixed (Monopile) versus floating (UMaine VolturnUS S semi-submersible) wind turbines. The expected power production according to the turbine's data from Gaertner et al. for the chosen wind speed, blade pitch and rotor speed is 1.4 times larger than the obtained power [4]. One has to find out what causes this difference and determine its importance. After this, it is suggested to run simulations using more realistic wind conditions to study the results and find the differences between bottom-fixed and floating wind turbines.

13.5. Other Recommendations

In this study, only the platform degrees of freedom are enabled and the blade pitch and rotor speed are fixed. It would be interesting to see what happens with the platform motions and flow fields when one enables all degrees of freedom (for example tower bending or flapwise and edgewise blade bending modes) and the control mechanisms. One could start running with simplified input profiles and then extend the model using more realistic weather conditions from ASPIRE. This has a practical application in wind farm forecasts. To achieve this, one must first incorporate a complete wind farm into the simulation. The connection makes it possible to precisely calculate the power generation and fatigue in a wind farm. To validate the model, one might run a full year using actual weather data for the area where the wind farm is located and compare the simulated power production with the actual power production of the selected wind farm. Then, it would be possible to identify in which situations the model accurately predicts the power output and which scenarios have higher differences. The model can then be improved by looking into these circumstances in further detail.

Also machine learning techniques can be used to improve the obtained power forecasts. These computer algorithms can automatically learn from data and improve their performance through experience [20]. Using past power measurements and meteorological forecasts of wind speed and direction at the site of the wind farm, one can improve power predictions. Besides, these machine learning techniques can enable optimal maintenance operations and asset protection, which prevents costly downtime of wind turbines. Furthermore, it can be trained to detect for example yaw misalignment to quickly return the turbine to its optimal position, increasing the power production [82].

In OpenFAST, a BEM-model is used to determine aerodynamic loads. However, because correction models are used to capture the aerodynamic phenomena present in the design load cases with turbulent wind, aerodynamic loads under challenging conditions can be overestimated when using such a model [83]. This could result in unnecessarily high component costs. Another method to determine aerodynamic loads is using higher-order aerodynamic methods, such as the Lifting-Line Free Vortex Wake model. It is recommended to make a coupling between ASPIRE and for example QBlade ([84]) to provide more realistic load calculations. The more accurate the power forecasts are, the lower the costs for energy producers because wind farms meet the expected supply thresholds more frequently.

Besides, it would be interesting to simplify the dynamics for a floating wind turbine to speed up the simulations. Implementing such a simplified version in ASPIRE, would allow Whiffle to do very precise and very fast forecasting for semi-submersible floating wind turbines. A suggestion would be to use an actuator disk model which is able to move in space according to a force balance between the pressure force from the wind and the tension force in the mooring lines using a spring-mass system. Combining low fidelity and high fidelity models could drastically reduce simulation times.

A. Appendix

A.1. Convergence Study - Platform Motions

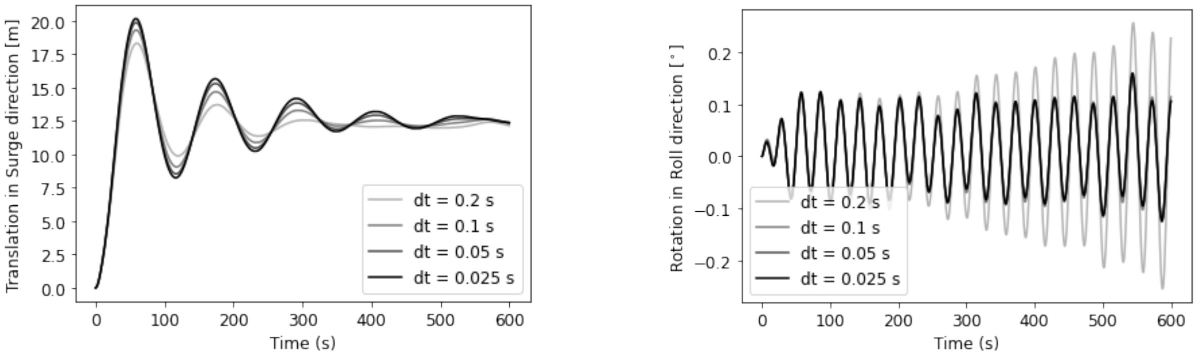

(a) Translation in Surge direction

(b) Rotation in Roll direction

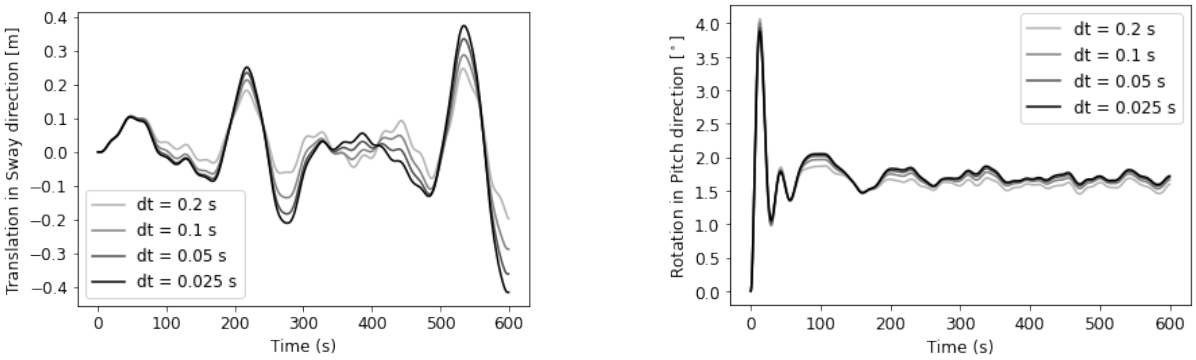

(c) Translation in Sway direction

(d) Rotation in Pitch direction

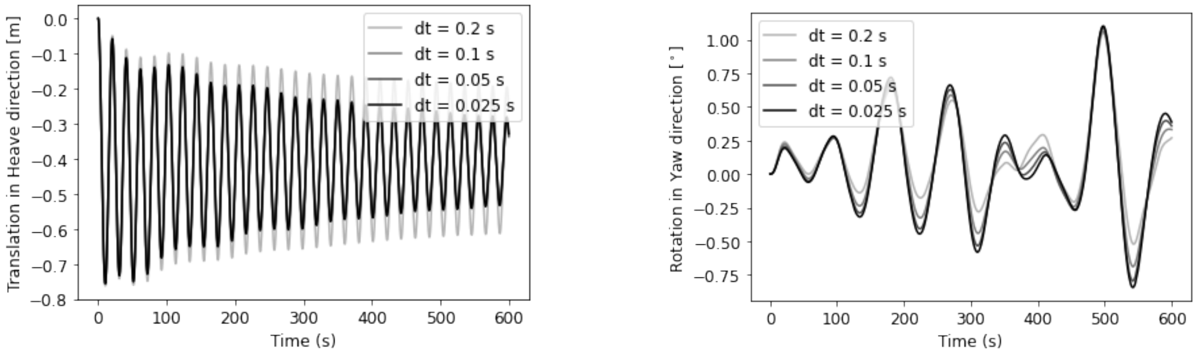

(e) Translation in Heave direction

(f) Rotation in Yaw direction

Figure 40: Platform motions in the six degrees of freedom plotted against the time for different time steps using the settings as described in Table 3. For clarity reasons, only the time steps in between 0.025 s and 0.2 s are shown in these graphs.

A.2. Convergence Study - Other Resolutions

A.2.1. Grid size of 16 m

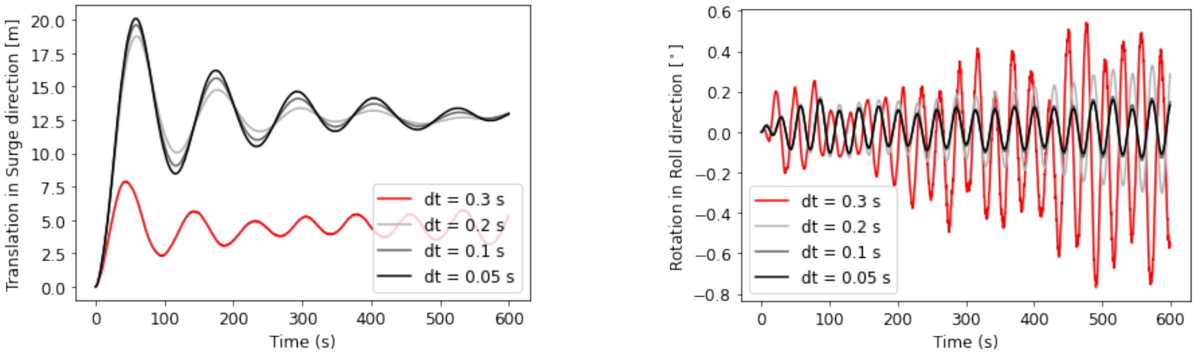

(a) Translation in Surge direction

(b) Rotation in Roll direction

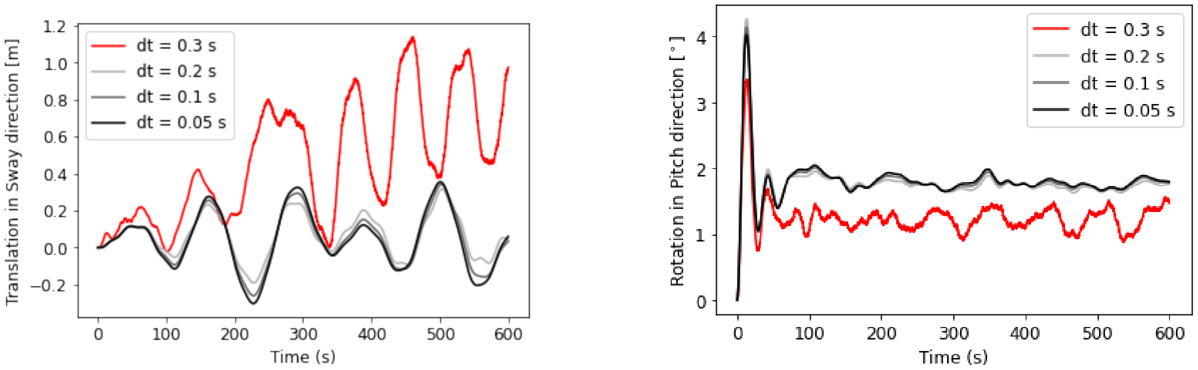

(c) Translation in Sway direction

(d) Rotation in Pitch direction

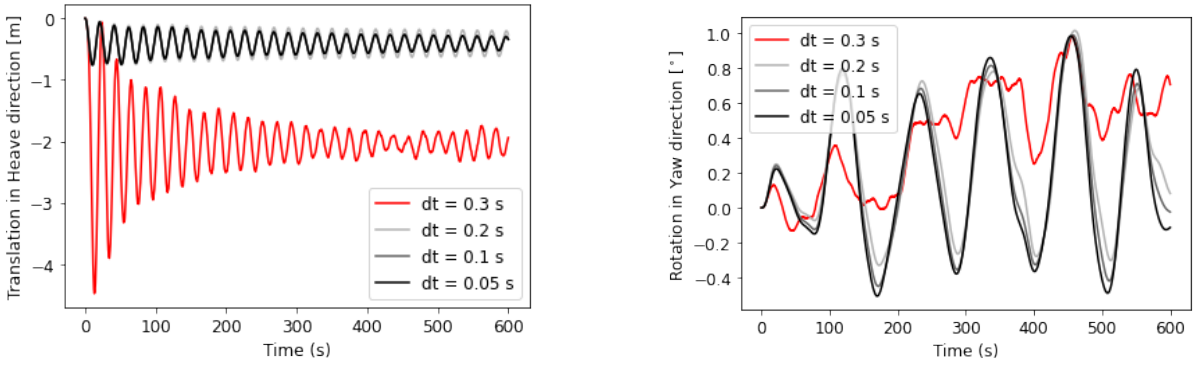

(e) Translation in Heave direction

(f) Rotation in Yaw direction

Figure 41: Platform motions in the six degrees of freedom plotted against the time for different time steps using the settings as described in Table 3 and a grid size of 16 m.

	Surge	**Sway**	**Heave**	**Roll**	**Pitch**	**Yaw**
from $\Delta t = 0.3$ s to $\Delta t = 0.2$ s	43.3	1573.7	1433.3	611.4	9.0	67.9
from $\Delta t = 0.2$ s to $\Delta t = 0.1$ s	0.13	6.7	1.5	57.1	0.06	4.1
from $\Delta t = 0.1$ s to $\Delta t = 0.05$ s	0.06	2.2	0.006	0.97	0.02	1.9

Table 15: The RMSE for the six degrees of freedom in platform motions using the settings from Table 3 with a grid size of 16 m, for different time steps, determined using Equation 22. All values are given in percentages.

A.2.2. Grid size of 32 m

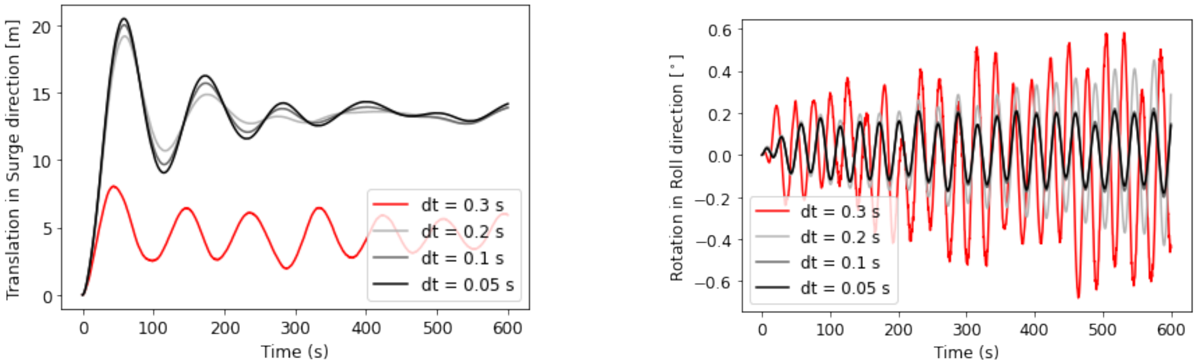

(a) Translation in Surge direction

(b) Rotation in Roll direction

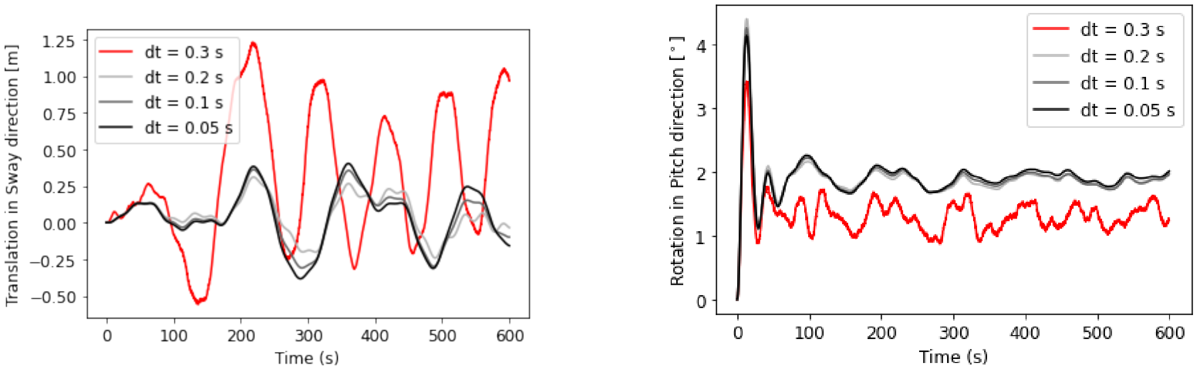

(c) Translation in Sway direction

(d) Rotation in Pitch direction

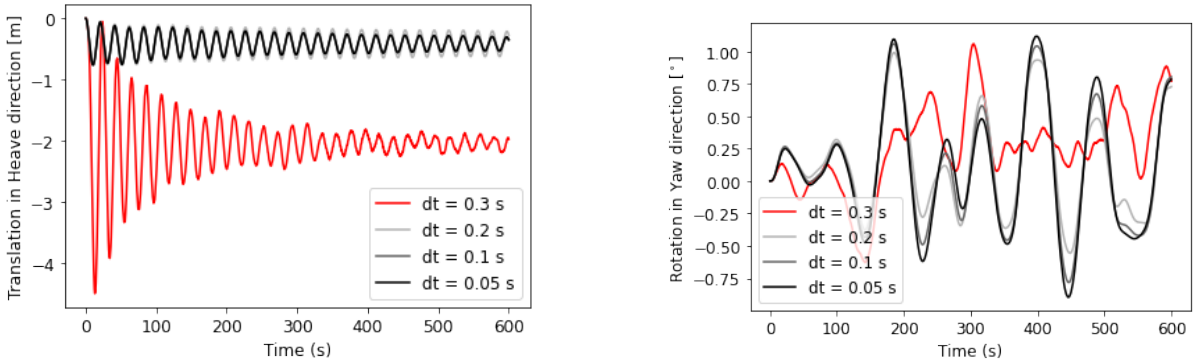

(e) Translation in Heave direction

(f) Rotation in Yaw direction

Figure 42: Platform motions in the six degrees of freedom plotted against the time for different time steps using the settings as described in Table 3 and a grid size of 32 m.

	Surge	**Sway**	**Heave**	**Roll**	**Pitch**	**Yaw**
from $\Delta t = 0.3$ s to $\Delta t = 0.2$ s	44.8	1526.3	1420.2	397.8	9.3	119.0
from $\Delta t = 0.2$ s to $\Delta t = 0.1$ s	0.1	12.0	1.5	52.3	0.04	4.3
from $\Delta t = 0.1$ s to $\Delta t = 0.05$ s	0.05	4.0	0.01	0.5	0.05	1.7

Table 16: The RMSE for the six degrees of freedom in platform motions using the settings from Table 3 with a grid size of 32 m, for different time steps, determined using Equation 22. All values are given in percentages.

A.3. Uniform Velocity Profiles - Sine-Fitting to Platform Motions

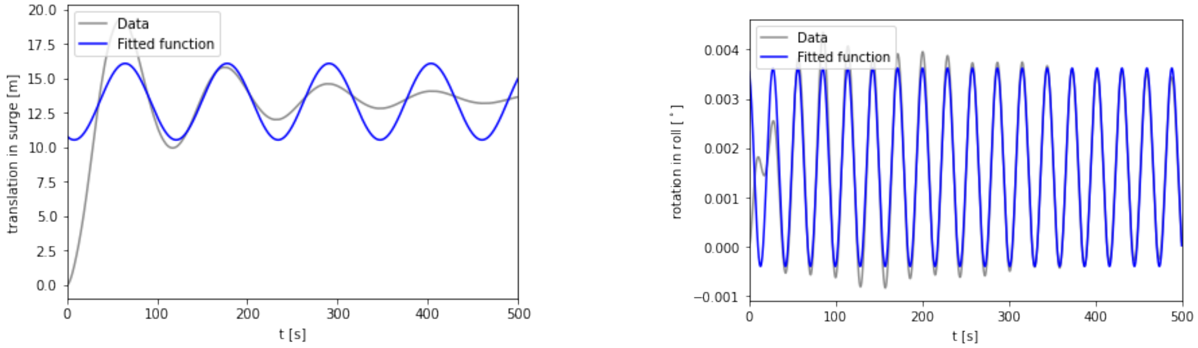

(a) Translation in Surge direction

(b) Rotation in Roll direction

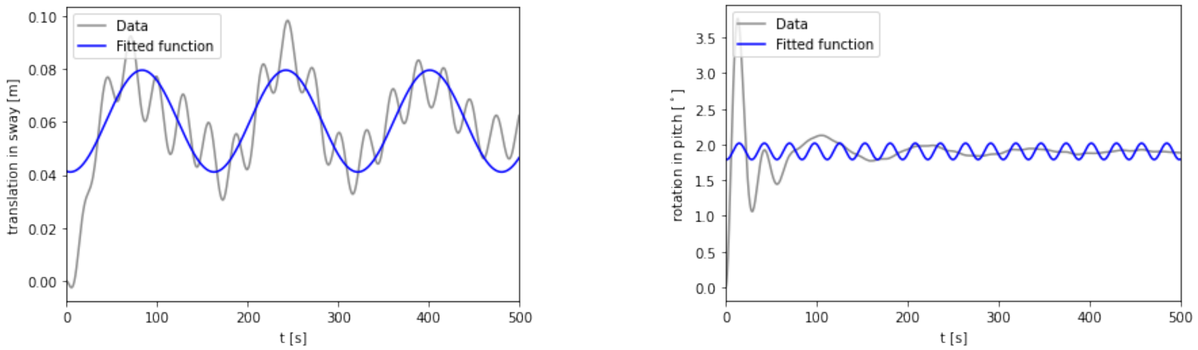

(c) Translation in Sway direction

(d) Rotation in Pitch direction

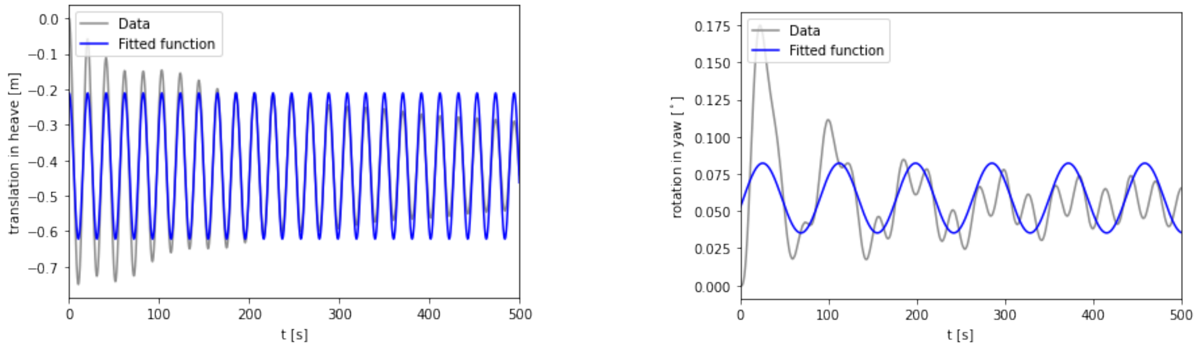

(e) Translation in Heave direction

(f) Rotation in Yaw direction

Figure 43: Platform motions in the six degrees of freedom plotted against the time obtained for the in input velocity of 8 m/s including fitted sine-function to determine the natural frequency in each degree of freedom. For clarity reasons, only the first 500 seconds of the simulation are shown.

References

[1] Christopher Allen, Anthony Viscelli, Habib Dagher, Andrew Goupee, Evan Gaertner, Nikhar Abbas, Matthew Hall, and Garrett Barter. Definition of the umaine volturnus-s reference platform developed for the iea wind 15-megawatt offshore reference wind turbine. Technical report, National Renewable Energy Lab.(NREL), Golden, CO (United States), 2020.

[2] Hannah Ritchie, Max Roser, and Pablo Rosado. Energy. *Our World in Data*, 2020. https://ourworldindata.org/energy.

[3] Paul Van der Valk. *Coupled Simulations of Wind Turbines and Offshore Support Structures: Strategies based on the Dynamic Substructuring Paradigm.* PhD thesis, 10 2014.

[4] Evan Gaertner, Jennifer Rinker, Latha Sethuraman, Frederik Zahle, Benjamin Anderson, Garrett E Barter, Nikhar J Abbas, Fanzhong Meng, Pietro Bortolotti, Witold Skrzypinski, et al. Iea wind tcp task 37: definition of the iea 15-megawatt offshore reference wind turbine. Technical report, National Renewable Energy Lab.(NREL), Golden, CO (United States), 2020.

[5] Hyeonjeong Ahn, Yoon-Jin Ha, and Kyong-Hwan Kim. Load evaluation for tower design of large floating offshore wind turbine system according to wave conditions. *Energies*, 16(4):1862, 2023.

[6] Alison Nugent and David DeCou. Chapter 5: Atmospheric stability. *Atmospheric Processes and Phenomenon. http://pressbooks-dev. oer. hawaii. edu/atmo/chapter*, 2018.

[7] Luoqin Liu and Richard J.A.M. Stevens. Effects of atmospheric stability on the performance of a wind turbine located behind a three-dimensional hill. *Renewable Energy*, 175:926–935, 2021.

[8] Matthew J Churchfield, Sang Lee, John Michalakes, and Patrick J Moriarty. A numerical study of the effects of atmospheric and wake turbulence on wind turbine dynamics. *Journal of turbulence*, (13):N14, 2012.

[9] Toan Tran and Dong-Hyun Kim. The platform pitching motion of floating offshore wind turbine: A preliminary unsteady aerodynamic analysis. *Journal of Wind Engineering and Industrial Aerodynamics*, 142, 07 2015.

[10] Xiangheng Feng, Yonggang Lin, Guohao Zhang, Danyang Li, Hongwei Liu, and Bin Wang. Influence of combined motion of pitch and surge with phase difference on aerodynamic performance of floating offshore wind turbine. *Journal of Marine Science and Engineering*, 9(7):699, 2021.

[11] National Renewable Energy Laboratory. Openfast documentation - openfast v3.2.0 documentation. https://openfast.readthedocs.io/en/dev/index.html, 2022.

[12] Lionel Moskowitz. Estimates of the power spectrums for fully developed seas for wind speeds of 20 to 40 knots. *Journal of geophysical research*, 69(24):5161–5179, 1964.

[13] Paris Agreement. Paris agreement. In *Report of the Conference of the Parties to the United Nations Framework Convention on Climate Change (21st Session, 2015: Paris). Retrived December*, volume 4, page 2017. HeinOnline, 2015.

[14] K Rohrig, C Richts, S Bofinger, M Jansen, M Siefert, S Pfaffel, and M Durstewitz. The importance of offshore wind energy for the energy sector and for the german energiewende, 2013.

[15] M Dolores Esteban, J Javier Diez, Jose S López, and Vicente Negro. Why offshore wind energy? *Renewable energy*, 36(2):444–450, 2011.

[16] Mehmet Bilgili, Abdulkadir Yasar, and Erdogan Simsek. Offshore wind power development in europe and its comparison with onshore counterpart. *Renewable and Sustainable Energy Reviews*, 15(2):905–915, 2011.

[17] Brunel. Onshore vs offshore wind: The pros and cons, May 2021.

[18] International Energy Agency (IEA). Offshore wind outlook 2019: World energy outlook special report, 2019.

[19] Aaron Zigeng Du. The frontier between fixed and floating foundations in offshore wind, Oct 2020.

[20] Andrea Di Stefano. Ai and machine learning in the wind power industry, Oct 2022.

[21] eSubsea. Floating offshore wind foundations - tlp, semi-sub and spar, Jul 2022.

[22] Delphine De Tavernier and Axelle Viré. Lecture notes in floating offshore wind energy (ae4w31, technical university of delft). 2022.

[23] Giovanni Gualtieri and Sauro Secci. Comparing methods to calculate atmospheric stability-dependent wind speed profiles: A case study on coastal location. *Renewable Energy*, 36(8):2189–2204, 2011.

[24] Linlin Tian, Yilei Song, Ning Zhao, Wenzhong Shen, Tongguang Wang, and Chunling Zhu. Numerical investigations into the idealized diurnal cycle of atmospheric boundary layer and its impact on wind turbine's power performance. *Renewable Energy*, 145:419–427, 2020.

[25] Roland B Stull. *An introduction to boundary layer meteorology*, volume 13. Springer Science & Business Media, 1988.

[26] Prem Datt. *Latent Heat of Condensation*, pages 702–703. Springer Netherlands, Dordrecht, 2011.

[27] Wikipedia contributors. Monin–obukhov similarity theory — Wikipedia, the free encyclopedia. `https://en.wikipedia.org/w/index.php?title=Monin%E2%80%93Obukhov_similarity_theory&oldid=1117642033`, 2022. [Online; accessed 17-March-2023].

[28] Ameya Sathe, Sven-Erik Gryning, and Alfredo Peña. Comparison of the atmospheric stability and wind profiles at two wind farm sites over a long marine fetch in the north sea. *Wind Energy*, 14(6):767–780, 2011.

[29] Jason Jonkman, Sandy Butterfield, Walter Musial, and George Scott. Definition of a 5-mw reference wind turbine for offshore system development. Technical report, National Renewable Energy Lab.(NREL), Golden, CO (United States), 2009.

[30] J Sanz Rodrigo, E Cantero, B García, F Borbón, U Irigoyen, S Lozano, PM Fernande, and RA Chávez. Atmospheric stability assessment for the characterization of offshore wind conditions. In *Journal of Physics: Conference Series*, volume 625, page 012044. IOP Publishing, 2015.

[31] AA Grachev and CW Fairall. Dependence of the monin–obukhov stability parameter on the bulk richardson number over the ocean. *Journal of Applied Meteorology*, 36(4):406–414, 1997.

[32] Lars Morten Bardal, Anja Eide Onstad, Lars Roar Sætran, and John Amund Lund. Evaluation of methods for estimating atmospheric stability at two coastal sites. *Wind Engineering*, 42(6):561–575, 2018.

[33] Alfredo Peña and Andrea N Hahmann. Atmospheric stability and turbulence fluxes at horns rev—an intercomparison of sonic, bulk and wrf model data. *Wind Energy*, 15(5):717–731, 2012.

[34] Andreas Platis, Marie Hundhausen, Astrid Lampert, Stefan Emeis, and Jens Bange. The role of atmospheric stability and turbulence in offshore wind-farm wakes in the german bight. *Boundary-Layer Meteorology*, 182(3):441–469, 2022.

[35] Qamar Chaudhry. An investigation on wind power potential of gharo-sindh, pakistan. *Pak J Meteorol*, 6, 01 2009.

[36] Balaji Subramanian, Ndaona Chokani, and Reza S Abhari. Impact of atmospheric stability on wind turbine wake evolution. *Journal of Wind Engineering and Industrial Aerodynamics*, 176:174–182, 2018.

[37] Kurt S Hansen, Rebecca J Barthelmie, Leo E Jensen, and Anders Sommer. The impact of turbulence intensity and atmospheric stability on power deficits due to wind turbine wakes at horns rev wind farm. *Wind Energy*, 15(1):183–196, 2012.

[38] Alfredo Peña, Pierre-Elouan Réthoré, and Ole Rathmann. Modeling large offshore wind farms under different atmospheric stability regimes with the park wake model. *Renewable energy*, 70:164–171, 2014.

[39] S Emeis. A simple analytical wind park model considering atmospheric stability. *Wind energy*, 13(5):459–469, 2010.

[40] Yu-Ting Wu and Fernando Porté-Agel. Large-eddy simulation of wind-turbine wakes: evaluation of turbine parametrisations. *Boundary-layer meteorology*, 138:345–366, 2011.

[41] Mahdi Abkar and Fernando Porté-Agel. Influence of atmospheric stability on wind-turbine wakes: A large-eddy simulation study. *Physics of fluids*, 27(3):035104, 2015.

[42] Meteorological aspects of siting large wind turbines. Technical report, Battelle Pacific Northwest Labs., Richland, WA (USA), 1981.

[43] Dae-Young Kim and Bum-Suk Kim. Differences in wind farm energy production based on the atmospheric stability dissipation rate: Case study of a 30 mw onshore wind farm. *Energy*, 239:122380, 2022.

[44] Sonia Wharton and Julie K Lundquist. Assessing atmospheric stability and its impacts on rotor-disk wind characteristics at an onshore wind farm. *Wind Energy*, 15(4):525–546, 2012.

[45] Rebecca Jane Barthelmie and LE Jensen. Evaluation of wind farm efficiency and wind turbine wakes at the nysted offshore wind farm. *Wind Energy*, 13(6):573–586, 2010.

[46] LE Jensen. Array efficiency at horns rev and the effect of atmospheric stability. *Dong Energy Presentation*, 2007.

[47] Leonardo P Chamorro and Fernando Porté-Agel. Effects of thermal stability and incoming boundary-layer flow characteristics on wind-turbine wakes: a wind-tunnel study. *Boundary-layer meteorology*, 136(3):515–533, 2010.

[48] M Dörenkämper, J Tambke, G Steinfeld, D Heinemann, and M Kühn. Atmospheric impacts on power curves of multi-megawatt offshore wind turbines. *Journal of Physics: Conference Series*, 555:012029, dec 2014.

[49] Irene Rivera-Arreba, Adam S Wise, Mahé Hermile, Fotini K Chow, and Erin E Bachynski-Polić. Effects of atmospheric stability on the structural response of a 12 mw semisubmersible floating wind turbine. *Wind Energy*, 2022.

[50] Adam S Wise and Erin E Bachynski. Wake meandering effects on floating wind turbines. *Wind Energy*, 23(5):1266–1285, 2020.

[51] Toan Tran and Dong-Hyun Kim. The platform pitching motion of floating offshore wind turbine: A preliminary unsteady aerodynamic analysis. *Journal of Wind Engineering and Industrial Aerodynamics*, 142, 07 2015.

[52] SN Das and Samir Kumar Das. Determination of coupled sway, roll, and yaw motions of a floating body in regular waves. *International Journal of Mathematics and Mathematical Sciences*, 2004(41):2181–2197, 2004.

[53] Nils Salvesen, EO Tuck, and Odd Faltinsen. Ship motions and sea loads. 1970.

[54] Sven Schmitz. 2a.2 the actuator disk model. `https://www.e-education.psu.edu/aersp583/node/471`, 2020.

[55] Wikipedia contributors. Blade element momentum theory — Wikipedia, the free encyclopedia. `https://en.wikipedia.org/w/index.php?title=Blade_element_momentum_theory&oldid=1096568358`, 2022. [Online; accessed 30-August-2022].

[56] Carlos Simão Ferreira. Lecture notes in rotor / wake aerodynamics (ae4135, technical university of delft). 2022.

[57] Bastian E. Rapp. Chapter 10 - conservation of mass: The continuity equation. In Bastian E. Rapp, editor, *Microfluidics: Modelling, Mechanics and Mathematics*, Micro and Nano Technologies, pages 265–271. Elsevier, Oxford, 2017.

[58] Aniko Toth and Elemer Bobok. Chapter 2 - basic equations of fluid mechanics and thermodynamics. In Aniko Toth and Elemer Bobok, editors, *Flow and Heat Transfer in Geothermal Systems*, pages 21–55. Elsevier, Oxford, 2017.

[59] Bastian E. Rapp. Chapter 11 - conservation of momentum: The navier-stokes equation. In Bastian E. Rapp, editor, *Microfluidics: Modelling, Mechanics and Mathematics*, Micro and Nano Technologies, pages 273–289. Elsevier, Oxford, 2017.

[60] Hermann Schlichting and Klaus Gersten. *Boundary-layer theory.* springer, 2016.

[61] Bastian E. Rapp. Chapter 12 - conservation of energy: The energy equation and the thermodynamic equation of state. In Bastian E. Rapp, editor, *Microfluidics: Modelling, Mechanics and Mathematics*, Micro and Nano Technologies, pages 291–301. Elsevier, Oxford, 2017.

[62] Wangda Zuo. Introduction of computational fluid dynamics, 2022.

[63] Wikipedia contributors. Ideal gas law — Wikipedia, the free encyclopedia. `https://en.wikipedia.org/w/index.php?title=Ideal_gas_law&oldid=1135737777`, 2023. [Online; accessed 1-March-2023].

[64] Gestione. Turbulence models in cfd - rans, des, les and dns, Apr 2022.

[65] Richard Courant, Kurt Friedrichs, and Hans Lewy. On the partial difference equations of mathematical physics. *IBM journal of Research and Development*, 11(2):215–234, 1967.

[66] Whiffle. https://whiffle.nl/, 2022.

[67] Whiffle. *Aspire Documentation Release 0.1.0.* Whiffle, 09 2022.

[68] National Oceanic US Department of Commerce and Atmospheric Administration. The coriolis effect, Jun 2013.

[69] D Jacob. The role of water vapour in the atmosphere. a short overview from a climate modeller's point of view. *Physics and Chemistry of the Earth, Part A: Solid Earth and Geodesy*, 26(6-8):523–527, 2001.

[70] Petri Majander and Timo Siikonen. Evaluation of smagorinsky-based subgrid-scale models in a finite-volume computation. *International Journal for Numerical Methods in Fluids*, 40(6):735–774, 2002.

[71] AW Vreman. An eddy-viscosity subgrid-scale model for turbulent shear flow: Algebraic theory and applications. *Physics of fluids*, 16(10):3670–3681, 2004.

[72] Wybe Rozema, Hyun J Bae, Parviz Moin, and Roel Verstappen. Minimum-dissipation models for large-eddy simulation. *Physics of Fluids*, 27(8):085107, 2015.

[73] D. van der Hoek, J. Frederik, M. Huang, F. Scarano, C. Simao Ferreira, and J.-W. van Wingerden. Experimental analysis of the effect of dynamic induction control on a wind turbine wake. *Wind Energy Science*, 7(3):1305–1320, 2022.

[74] scipy.optimize.curve_fit SciPy v1.10.1 Manual. scipy.optimize.curve_fit. https://docs.scipy.org/doc/scipy/reference/generated/scipy.optimize.curve_fit.html, 2023.

[75] Vern Lindberg. nbsp;uncertainties and error propagation part i of a manual on uncertainties, graphing, and the vernier caliper, Jul 2000.

[76] Ahmed Elkadi. New pile installation method for offshore wind monopiles, Nov 2021.

[77] IEAWindTask37. Ieawindtask37/iea-15-240-rwt: 15mw reference wind turbine repository developed in conjunction with iea wind, Nov 2022.

[78] Alessandro Fontanella, Alan Facchinetti, Simone Di Carlo, and Marco Belloli. Wind tunnel investigation of the aerodynamic response of two 15 mw floating wind turbines. *Wind Energy Science*, 7(4):1711–1729, 2022.

[79] Benyamin Schliffke, Sandrine Aubrun, and Boris Conan. Wind tunnel study of a "floating" wind turbine's wake in an atmospheric boundary layer with imposed characteristic surge motion. In *Journal of Physics: Conference Series*, volume 1618, page 062015. IOP Publishing, 2020.

[80] Peng Hou, Jiangsheng Zhu, Kuichao Ma, Guangya Yang, Weihao Hu, and Zhe Chen. A review of offshore wind farm layout optimization and electrical system design methods. *Journal of Modern Power Systems and Clean Energy*, 7(5):975–986, 2019.

[81] Nina Svensson, Hans Bergström, Erik Sahlée, and Anna Rutgersson. Stable atmospheric conditions over the baltic sea: model evaluation and climatology. 2016.

[82] Rob Budny. The application of ai across wind energy, Oct 2022.

[83] Sebastian Perez-Becker, Francesco Papi, Joseph Saverin, David Marten, Alessandro Bianchini, and Christian Oliver Paschereit. Is the blade element momentum theory overestimating wind turbine loads?–an aeroelastic comparison between openfast's aerodyn and qblade's lifting-line free vortex wake method. *Wind Energy Science*, 5(2):721–743, 2020.

[84] D. Marten. Qblade - next generation wind turbine simulation, Mar 2023.